

**POLITECNICO DI TORINO**

Master's Degree in Energy and Nuclear Engineering



**Politecnico  
di Torino**

Master's Degree Thesis

**Advancements in glass-ceramic sealants  
for proton conductive electrolysis cells  
(PCECs)**

Supervisors

Prof. Federico SMEACETTO

Prof. Massimo SANTARELLI

Dr. Simone ANELLI

Dr. Domenico FERRERO

Candidate

**Alessio RIORDA**

Academic Year 2022/2023



# Summary

In response to the escalating levels of  $CO_2$  and other greenhouse gas (GHG) emissions, countries worldwide have recognized the critical need for a more sustainable system. To tackle this global crisis, governments are increasingly implementing new laws and strategies that prioritize the utilization of renewable energy technologies. However, one of the key challenges associated with these solutions is their intermittency, highlighting the necessity for efficient energy storage systems and solution for the overproduction period. In the last years, the utilization of hydrogen as a viable energy vector has become a pivotal driving force behind the ongoing energy transition towards a low-carbon future. Electrolysis of water, specifically green hydrogen production, offers a means to generate hydrogen by splitting water molecules using electricity, with the resulting hydrogen that can be after utilized as a fuel to generate electricity. In this context, high temperature cells have high efficiency, due to the elevated temperature that helps transport mechanisms. Solid Oxide Cells (SOCs) and Proton Ceramic Cells (PCCs), with a temperature range of 700-1000°C and 500-700°C, respectively are part of this family. While SOCs currently represent the most advanced technology, their primary drawback lies in the degradation issues stemming from their high operational temperature range. To address this concern, PCCs, which rely on proton-conducting electrolytes, present a promising solution by reducing operating temperatures while maintaining high efficiency and cost-effectiveness. PCECs are now mainly at laboratory scale, so more efforts are needed to develop stack of large area cells with commercial interest. This thesis aims to improve the knowledge on this open issue, focusing on the characterization of the sealant material. The sealant is a crucial component in this technology as it prevents gas leakage or diffusion within the stack. In the case of the presented study, glass-ceramic sealants were considered. The characterization process included both the thermo-mechanical and chemical aspects of the sealant material, like the compatibility with the other component of a stack of cells (electrolyte, electrode, and interconnector), and the behaviour of the selected material at the operational temperature (500-700°C). Additionally, further studies were made, preparing glass pastes and analysing their rheological properties, in terms of printability and shape-fidelity. This was done for evaluate the feasibility to use

a robocasting deposition method, which establish the foundations for industrial scaling of the production. After simulation modeling was carried out with the objective of establishing and verifying a reference model for a PCEC. This model was constructed using COMSOL Multiphysics software and fine-tuned with data sourced from existing literature.



# Table of Contents

<b>List of Tables</b>	VII
<b>List of Figures</b>	VIII
<b>Acronyms</b>	XIV
<b>1 Introduction</b>	<b>1</b>
1.1 Role of hydrogen . . . . .	1
1.2 Electrolysis . . . . .	3
1.2.1 Overview . . . . .	3
1.2.2 Thermodynamic behaviour of electrolysis cells . . . . .	6
1.3 Proton Conductive Cells (PCCs) . . . . .	6
1.3.1 PCC operation . . . . .	8
1.3.2 State of the art materials for PCEC stack . . . . .	10
1.4 Glass and glass-ceramic seals . . . . .	18
1.4.1 Effect of composition on thermal characteristics . . . . .	18
1.4.2 Additive manufacturing . . . . .	20
1.4.3 Ceramic inks . . . . .	23
1.5 Goal of the thesis . . . . .	24
<b>2 Experimental Methods</b>	<b>26</b>
2.1 Glass-ceramic preparation . . . . .	26
2.1.1 Composition of the glasses and casting procedure . . . . .	26
2.2 Paste preparation . . . . .	27
2.2.1 Glass modification . . . . .	29
2.3 Rheological characterization of ceramic inks . . . . .	30
2.4 Joining fabrication . . . . .	31
2.4.1 Sample preparation . . . . .	31
2.4.2 Ageing of samples . . . . .	32
2.5 Thermal analysis . . . . .	33
2.5.1 Differential scanning calorimetry (DSC) . . . . .	33

2.5.2	Heating stage microscopy (HSM)	34
2.5.3	Dilatometry (DIL)	36
2.6	Microstructural characterization	36
2.6.1	Scanning electron microscopy (SEM)	36
2.6.2	X-ray diffraction (XRD)	38
<b>3</b>	<b>Results and discussion</b>	<b>39</b>
3.1	Glass characterization	39
3.1.1	Evaluation of characteristic temperatures	39
3.1.2	Coefficient of thermal expansion (CTE)	43
3.2	Paste characterization	44
3.3	Microstructural characterization	47
3.3.1	Joined samples	48
3.3.2	After ageing	51
3.4	Modification of glass composition	54
3.4.1	GM31107+8YSZ	54
3.4.2	GM31107+3YSZ	56
<b>4</b>	<b>Numerical modelling</b>	<b>59</b>
4.1	Model development	59
4.1.1	Charge balance	59
4.1.2	Mass balance	60
4.1.3	Heat balance	61
4.1.4	Electrochemical reaction	61
4.2	Geometry	62
4.3	Simulation results	63
4.3.1	Boundary conditions	63
4.3.2	Electrochemical behaviour curves	64
4.3.3	Species mole fraction	65
4.3.4	Heat balance	67
<b>5</b>	<b>Conclusion</b>	<b>69</b>

# List of Tables

1.1	Comparison between different typer of electrolysis cell technologies	5
2.1	Three different BCZY considered, with their composition and nomenclature utilized inside the work. . . . .	26
2.2	Evaluated glasses composition . . . . .	27
2.3	PG paste composition (%wt). . . . .	29
2.4	Terpineol paste composition (%wt). . . . .	29
3.1	CTE of different materials . . . . .	43
3.2	Samples nomenclature . . . . .	48
4.1	Geometry parameters of the PCEC . . . . .	64

# List of Figures

1.1	Hydrogen utilization, from 1975 to 2021, for different purpose. The first column is about utilities that need pure hydrogen, the second one considers hydrogen mixed with other gas. Data from 2019 IEA report on hydrogen [3]. . . . .	2
1.2	Sources utilized for hydrogen production. [4]. . . . .	3
1.3	Electrolyser capacity in different region [4] . . . . .	5
1.4	Electrolyser capacity, in GW/year for different technologies [4] . . . . .	5
1.5	Energy demand for hydrogen production from water splitting[9] . . . . .	6
1.6	Difference between a SOC and a PCC in a electrolyser mode. . . . .	7
1.7	Two configuration for a PCC: a) fuel cell mode, and b) electrolysis mode . . . . .	8
1.8	Polarization i-V curve for electrolysis configuration. The over-voltage losses zones are highlighted [9]. . . . .	9
1.9	Polarization i-V curve for fuel cell configuration. Also in this case the over-voltage zones are highlighted, and is also present a dotted line representing the power density curve[9]. . . . .	10
1.10	Representation of the active area in the cathode, in the case of MIEC (a) and TCO (b) material[19]. . . . .	11
1.11	Schematic representation of the conduction of different charged species, considering the four main typology of air electrode materials: a) pure electronic conductor, b) MIEC, c) MPEC, d) THOEC. . . . .	13
1.12	Ionic conductivity of different electrolyte materials, function of the temperature[29]. . . . .	15
1.13	Diagram of a portion of stack for a PCEC. Is possible to notice the aim of the interconnector, which allow the diffusion of the gas, through the channel, in and out of the electrodes, and represent a pathway for the electrons. The cell is portrayed with the following colors: Fuel electrode (green), electrolyte (blue), and air electrode (red).In the right there is a magnification of the boxed zone. The proportion are not observed here for a simpler comprehension. . . . .	16

1.14	This diagram shows the possible position of the sealant for a PCEC stack. . . . .	18
1.15	Representation of a glass network structure. All the possible type of glass network components are here reported[33]. . . . .	19
1.16	Additive manufacturing process of robocasting. This typology of process allows the deposition of an ink to the surface, thanks to a s pressure applied (extrusion force) that drives the in k through a nozzle[37]. . . . .	20
1.17	These curves report the response behaviour of different type of materials to te application of a shear rate.a) shear stress versus shear rate, b) apparent viscosity versus shear rate [37]. . . . .	22
1.18	Diagram of ink extrusion through a nozzle,, during a robocasting process[37]. . . . .	22
1.19	Diagram that represent the three different configurations used during the paste extrusion in a robocasting process. An electric motor can be utilized for drive a piston (a) or a screw b). Alternative solution implies the utilization of compressed air [39]. . . . .	23
1.20	Diagram representing three main type of ceramic inks for robocasting. The steric mechanism is here represented by black lines, connected to the particles.The negative charges are pictured in red, and the polymer chains are drawn like green lines [40]. . . . .	24
1.21	Three main mechanisms for particles stabilization: electrostatic, steric, and electrosteric. Steric interactions are represented by black lines, while electrostatic interactions by negative red charges [40]. . . . .	24
2.1	Robocasting instrument utilized for the paste deposition (ZMorph S.A. Company) . . . . .	28
2.2	Different plates configurations for rheological properties tests. . . . .	30
2.3	Printability test for the prepared pastes. The case here reported was about the GM31107 PG paste. . . . .	31
2.4	Schematic representation of a joining between a layer of FSS (dark grey), an half-cell (electrode green, and electrolyte brown), and a deposited layer of glass-ceramic sealant (light grey). On the right, there are two real joined samples, produced during this thesis work.	32
2.5	On the left there are all the samples prepared for the ageing test, with humid air (50%). On the right side, ageing test setup is shown.	33
2.6	Left figure report a diagram of the DSC internal configuration [42]. On the right there is a photo of the DSC used for this work (DSC 404 F3 Pegasus, Netzsch, Germany) . . . . .	34
2.7	HSM instrument used for the measurements (EM301 Heating Microscope, Hesse Instrument, Germany) . . . . .	35

2.8	Left diagram represent the internal structure of a dilatometry instrument. On the right, is possible to see the dilatometry utilized for the work (DIL402PC, Netzsch, Germany) . . . . .	36
2.9	Representation of the operating principles of an SEM (a), and the type of signals produced during the interaction between electrons and the material (b)[9]. . . . .	37
2.10	Two samples encapsulated in resin, ready for the SEM visualization.	38
2.11	Representation of operating principles of an XRD test (a), and XRD instrument (b)[9]. . . . .	38
3.1	DSC analysis on GM31107, compared with results from previous works on V11, V10, and GC2. . . . .	40
3.2	HSM measurements on GM31107, and data from previous works on V11, V10, and GC2. Characteristic temperatures are highlighted in the graphic with colored marker. The figures below explain the meaning of the numbers associated to the markers. . . . .	41
3.3	Curves relative to different HSM tests, made utilizing three typology of BCZY like substrate. The dashed line represent the values obtained in the case with $Al_2O_3$ . . . . .	42
3.4	Curves relative to the measurments made by HSM, on GC2, considering different BCZY like substrate. The dashed line represent the values obtained in the case with $Al_2O_3$ . . . . .	42
3.5	Curves relative to the dilatometry of GM31107 (three different measurements), and GC2, from previous works. CTE values obtained in the range 300-500°C are also reported. . . . .	44
3.6	Flow curves of GM31107 in terpineol paste (red dots), and GM31107 in PG paste (black squares). Empty markers represent the shear stress. . . . .	45
3.7	Flow curves of GC2(blue line) and V11(green line) terpineol pastes. In this case lines are used to underling the fact that these results came from a preavious study [48]. Dashed lines represent the shear stress. . . . .	46
3.8	Three interval thixotropy test for GM31107+PG paste. In the figure are also reported the percentage values of recovery. . . . .	46
3.9	Three interval thixotropy test for GC2 (blue dots) and V11 (green dots) terpineol pastes. Also in this case the data utilized came from a previous study [48] . . . . .	47
3.10	Two images of joined samples obtained through SEM: a) S02, and b) S01 . . . . .	48

3.11	SEM images of the samples S01 and S02, with the magnification of the interfaces between the layers. For S01, a) shows the interface among the glass and the AISI441, while in b) there are glass and BCZY1. The images of the S02 are reported below, where in c) there is the interface with the Crofer22APU, and in d) with the BCZY1 .	49
3.12	EDX of the interface between glass and AISI441, for the sample S01. The aim is to evaluate the possible interdiffusion of Cr in the glass phase. . . . .	50
3.13	EDX of the interface between glass and AISI441, for the sample S01. The aim is to evaluate the possible interdiffusion of Cr in the glass phase. . . . .	50
3.14	Focus on the formation of crystalline phase inside the glass in the case of a) S03 and b) S04 . . . . .	51
3.15	Focus on the formation of crystalline phase inside the glass in the case of a) S03 and b) S04 . . . . .	52
3.16	SEM images of the samples S03 and S04, with the magnification of the interfaces between the layers. For S03, a) show glass and $BCZY_1$ , while b) shows the interface among the glass and the AISI441. The images of the S04 are reported below, where in c) there is the interface with the $BCZY_1$ , and in d) with the Crofer22APU . . . . .	52
3.17	SEM images of the joined samples S05, with V11, $BCZY_1$ and AISI441. . . . .	53
3.18	Magnification of the interface between V11 and a) AISI441, and b) $BCZY_1$ . . . . .	53
3.19	On the left there is a magnification of a 8YSZ powder, which was utilized for the evaluation of particles size. On the right there is a size distribution of the particles. . . . .	54
3.20	Comparison of HSM results between pure GM31107 and modified one, with the adding of 8YSZ (5%wt). . . . .	55
3.21	All the results obtained during the HSM tests on GM31107+8YSZ(5%). Comp-1 and Comp-2 were made from a paste droplet, while comp-3 was a normal HSM test on a powder pellet. Under the chart are reported the samples after the HSM tests. . . . .	55
3.22	SEM images of joined samples, containing glass-ceramic sealant (GM31107+8YSZ). . . . .	56
3.23	SEM images of the samples with modified GM31107. First two are related to GM31107+3YSZ (2,5%), where a) show glass and AISI411, while b) shows the interface among the glass and the $BCZY_1$ . The remaining images are about GM31107+3YSZ (5%), where in c) there is the interface with the AISI441, and in d) with the $BCZY_1$ . . . . .	57

3.24	SEM magnifications of the glass phase: a) <i>AISI441+GM31107(+2.5%wt3YSZ)+BCZY<sub>1</sub></i> and b) <i>AISI441 + GM31107(+5%wt3YSZ) + BCZY<sub>1</sub></i> . . .	58
4.1	Geometry of the model from COMSOL software. . . . .	63
4.2	Magnification of the cell, from the model geometry . . . . .	63
4.3	Polarization curve i-V, from the COMSOL model of a PCEC. . . .	65
4.4	Power density vs Current density curve, from COMSOL model of a PCEC. . . . .	65
4.5	Molar fraction results, for a voltage equal to 1.6V, from COMSOL software. a) <i>H<sub>2</sub></i> molar fraction, b) <i>O<sub>2</sub></i> molar fraction, and c) <i>H<sub>2</sub>O</i> molar fraction . . . . .	66
4.6	Temperature trend inside the cell. Black curve represent the average temperature inside the cell, while the red and blue are the minimum and maximum temperature in the cell respectively. . . . .	67
4.7	Temperature distribution results, for different cell voltage, from COMSOL software. a) distribution at 1.2 V, so under the thermoneutral voltage, b) distribution at 1.5 V, so over the thermoneutral voltage . . . . .	68



# Acronyms

**AEC**

Alkaline electrolysis cell

**AM**

Additive manufacturing

**BOP**

Balance of plant

**BCZY**

$BaZr_{0.625}Ce_{0.2}Y_{0.175}O_{3-\sigma}$

**CTE**

Coefficient of thermal expansion

**DSC**

Differential scanning calorimetry

**EC**

Ethyl Cellulose

**EDX**

Energy dispersive X-Ray spectroscopy

**FSS**

Ferritic stainless steel

**GDE**

Gas diffusion electrode

**GDL**

Gas diffusiol layer

**GHG**

Greenhouse gasses

**HSM**

Hot stage microscopy

**MSEC**

Molten salt electrolysis cell

**OCV**

Open circuit voltage

**PCEC**

Proton conductive electrolysis cell

**PEM**

Proton exchange membrane electrolysis cell

**PG**

Propylene Glycol

**SEM**

Scanning electron microscopy

**SOEC**

Solid oxide electrolysis cell

**SRU**

Single repeating unit

**TPB**

Triple phase boundary

**YSZ**

Yttria stabilized zirconia

# Chapter 1

## Introduction

### 1.1 Role of hydrogen

In the last decades, renewable energy has gained more importance in the world energy system, as concerns about climate change and air pollution have grown. These energy sources, such as wind, solar, and hydropower, have become affordable and accessible all over the world, thanks to technological improvements and incentives. Despite this, many challenges are still present in the path to totally decarbonise our society. An IEA study has outlined several scenarios for energy transition, projecting the situation up to 2050 based on different actions, where, the most ambitious is the “Net Zero Emission by 2050”[1]. Achieving this target means to reach net zero emission of Carbon dioxide into atmosphere, and implies a focus on different key aspects like the electrification of consumption, enhancing energy system efficiency, and adopting low-carbon technologies such as nuclear and renewables[1][2]. The real problem inherent the depletion of fossil fuels is related to their central role in our society, and their many advantages such as convenience, utilization flexibility, and ease of transport and storage. Indeed, if for the affordability, renewable technologies are now on the path to becoming the best solution worldwide[2], their intermittency represent still a big issue. Here, hydrogen emerges as a potential solution. Beyond its industrial applications, hydrogen functions as an energy carrier, capable of storing electric energy as chemical energy via the “Power-to-gas” process. Energy surplus during overproduction periods can be used to produce hydrogen, that can be converted later in energy. Nowadays, hydrogen is mainly utilized in the industrial sector. Its demand is around 70 Mt/y, considering only the pure hydrogen (further 45 Mt/y of  $H_2$  mixed with other gasses is used in industry). In figure 1.1 these data are highlighted with the subdivision between pure hydrogen utilization and blend of hydrogen and other gas. The production processes depend almost entirely on fossil fuels, needing 6% and 2% of

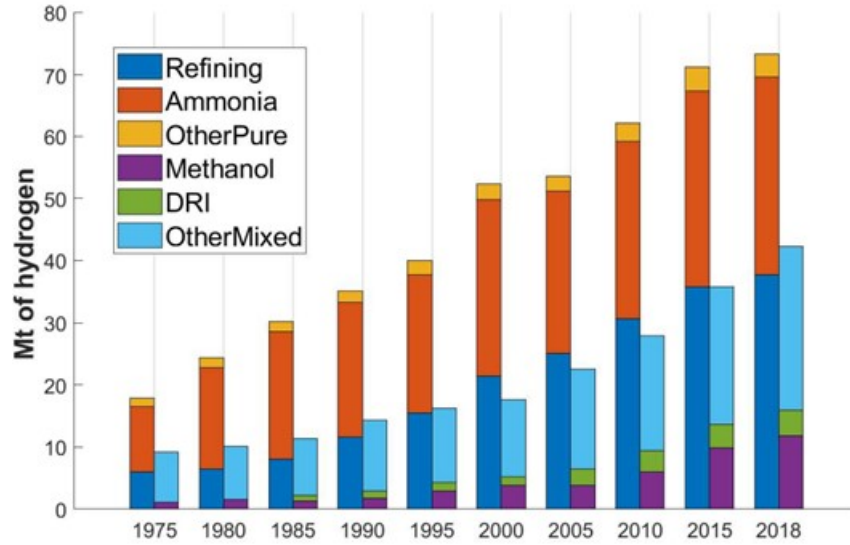


**Figure 1.1:** Hydrogen utilization, from 1975 to 2021, for different purpose. The first column is about utilities that need pure hydrogen, the second one considers hydrogen mixed with other gas. Data from 2019 IEA report on hydrogen [3].

global natural gas and coal utilization respectively. For these reasons, hydrogen is responsible for the emission of 830 Mt/y of CO<sub>2</sub>, equivalent to the CO<sub>2</sub> emissions of Indonesia and United Kingdom combined [3]. Hydrogen production is increased, reaching 94 Mt/y in the 2021, with associated emission of more than 900 Mt/y of CO<sub>2</sub> [4]. Figure 1.2 reports data, related the years 2020 and 2021, about the main routes of hydrogen production, with a total predominance of fossil fuel sources, over 80%[4]. In addition to that, hydrogen could be an opportunity for decarbonization in challenging hard-to-abate sector like heavy road transport, specific industries like steel and cement production, as well as maritime and aviation sectors[5]. In summary, hydrogen can facilitate energy transition and establishment of a sustainable system through two main pathways: 1) Transforming current hydrogen production using “green” H<sub>2</sub> technologies or incorporating CO<sub>2</sub> capture into existing processes to yield “blue” H<sub>2</sub>; 2) Employing hydrogen in new applications, as mentioned earlier, with both hard-to-abate and energy sectors.

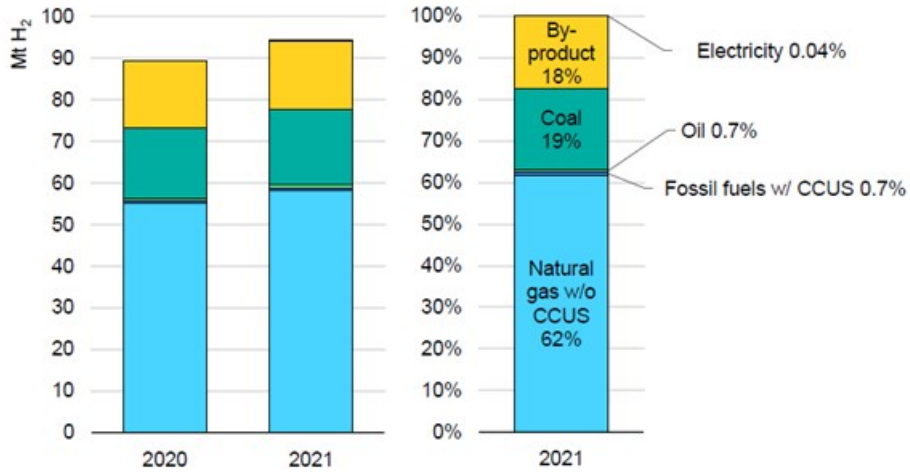


Figure 1.2: Sources utilized for hydrogen production. [4].

## 1.2 Electrolysis

### 1.2.1 Overview

Electrolysis cells are electrochemical devices, which utilize electrical energy to produce hydrogen, through a redox reaction. Even if, as shown previously, hydrogen production is nowadays led from fossil fuel-based process, in the recent years there has been a notable increase in the adoption of this technology [4][6]. In the end of 2021, the capacity was of 510 MW, with an increase of 70% respect the 2020, but remain in the order of 0.1% of the total hydrogen production[4]. Prediction from a global hydrogen review from IEA said that in 2030 the electrolyser capacity will be in the order of 134 GW, with an average plant size increase from 5MW (2021) to GW-scale by 2030, with Europe leading this development trend[4]. Exist different types of electrolysis cells, categorized according to electrolyte material, operational temperature, and charge carrier (there are also other classification parameters, but these are the most relevant). In table. 1.1 are reported different types of cells. Today, Alkaline electrolysis cells (AECs) dominate the market, with more than 70% of global manufacturing capacity. The reason behind that is related to the maturity of the technology compared with PEMECs and SOECs[4]. The name came from the electrolyte, like also in the other case, that is a liquid alkaline solution of  $KOH$ . Charge carrier is  $OH^-$ , which is produced, together with hydrogen, in the cathode, from the separation of the water molecule. Then the ion passes through a liquid  $KOH$  and a porous diaphragm, positioned between the two electrodes for avoids mixing of hydrogen and oxygen[7]. At the opposite electrode then, oxygen and water are formed. For the components, metallic materials are

used, like platinum and nickel for the cathode and other for the anode, like oxides or also here nickel[8][7]. Proton exchange membrane electrolysis cells (PEMECs) are based on conduction of protons through a polymeric membrane (Nafion). Water is split in the anode, applying a voltage to the cell, and obtaining protons, which pass through the polymeric membrane, arriving to the cathode, where pure hydrogen is produced. The temperature range of operation in this case is ( 50-80°C)[9][10]. Another technology, the molten salt electrolysis cells (MSECs), utilizes molten carbonates as electrolytes, and present  $CO_3^{2-}$  like charge carrier [11]. It works at medium-high temperatures (400-800°C) and the main use of these cells is related to the reduction of carbon dioxide, that lead to the production of solid carbon. For this reason, the cathode must be replaced often[12]. Differently from other solutions, solid oxide electrolysis cells (SOECs) utilize ceramic materials as components, such as a dense ceramic ionic conductor electrolyte, composed of  $ZrO_2$  doped with different composition of  $Y_2O_3$  (YSZ). For the fuel electrode is used a porous cermet composed of YSZ and Nickel, and for the oxygen electrode a lanthanum strontium manganite (LSM)/YSZ composite[13]. Working at high temperature (600-900°C), this solution represents an advantage in terms of kinetics and thermodynamic behavior, because it lowers the internal resistance and improves the conversion rates. These characteristics lead to a higher efficiency (around 80%) than other cells and represent a reason of interest for the research. However, the elevated operational temperature also drives to disadvantages like the necessities of expensive materials and a lower lifetime of the cell components. These are some of the drawbacks that make this technology more expensive than the other and make necessary further studies[13]. An alternative to SOECs is represented by PCEC. Indeed, these cells, compared with oxygen-conductive ones, can reduce of several hundreds of degrees the operational temperature, maintaining high efficiency. This is possible due to the conduction of protons ( $H^+$ ) like charge carriers. PCEC technology is still at a laboratory scale and research for the development of a multi-cell stack is required [14]. Further characteristic description about this solution will be available in the next section.

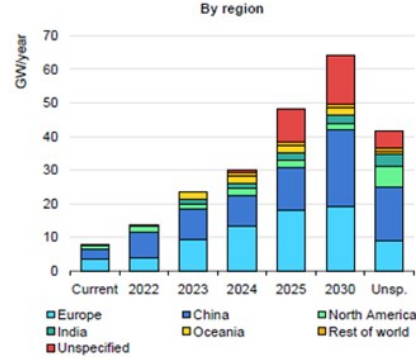


Figure 1.3: Electrolyser capacity in different region [4]

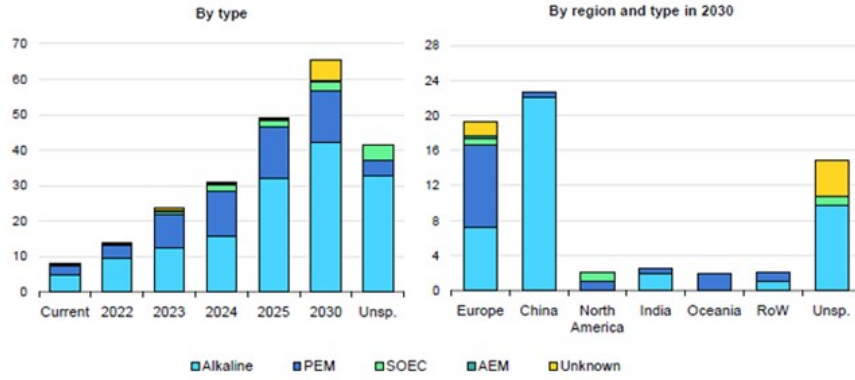


Figure 1.4: Electrolyser capacity, in GW/year for different technologies [4]

	PEMEC	AEC	MSEC	SOEC	PCEC
Electrolyte	Polymeric membrane	Liquid KOH	Molten salt	Ceramic	Ceramic
Charge Carrier	$H^+$	$OH^-$	$CO_3^{2-}$	$O^{2-}$	$H^+$
Operating Temp. (°C)	50-80	70-90	400-800	600-900	500-600
Pressure (atm)	30-80	1-30	1-6	1	1
Catalyst	Platinum	Platinum, Nickel	Nickel	Nickel	Nickel
Cell Components	Carbon based	Carbon based	Metal-based, oxides	Ceramic based	Ceramic based
Fuel Compatibility	$H_2O$	$H_2O$	$CO_2$	$H_2O, CO_2, CH_4$	$H_2O, CH_4$

Table 1.1: Comparison between different typer of electrolysis cell technologies

### 1.2.2 Thermodynamic behaviour of electrolysis cells

For non-spontaneous process like water splitting, energy is required to bring the reaction to completion. The total amount of energy necessary for the electrolysis process is given by the Gibbs free energy eq. 1.1:

$$\Delta G = \Delta H - T\Delta S \quad (1.1)$$

$\Delta H$  represents the total energy requirement,  $\Delta G$  is the Gibbs free energy and also the electrical part of the total energy, and  $T\Delta S$  the thermal contribution. Observing figure. 1.5, one can notice that when the operational temperature increases, electrical energy requirement decreases. Considering  $\Delta H$  quite constant, this means that thermal energy provides part of the energy necessary for the reaction.

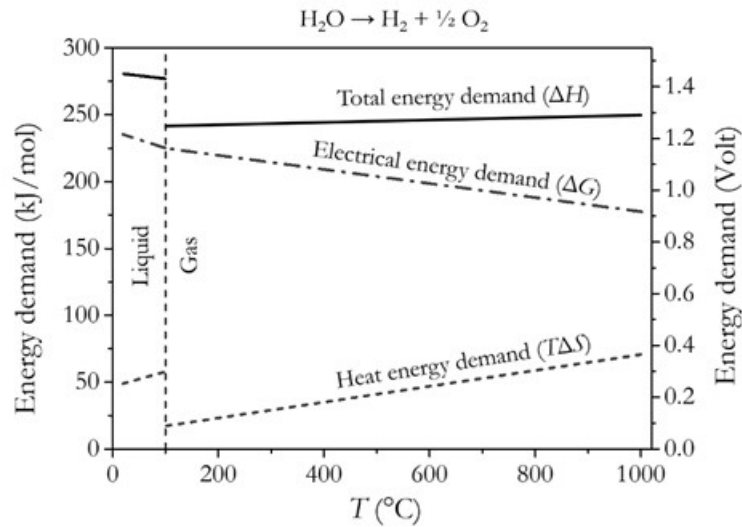


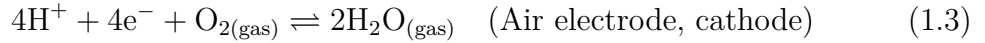
**Figure 1.5:** Energy demand for hydrogen production from water splitting[9]

### 1.3 Proton Conductive Cells (PCCs)

In the field of electrochemical technologies, an interesting area of research is represented by SOCs. These cells have gained substantial attention, due to their impressive operational efficiencies and remarkable adaptability to different fuel sources. However, the path to their industrial feasibility is slowed down by several challenges, the majority of which arise from their requirement for high operational temperatures (600-900°C). These challenges include fast degradation of performance and components, an overall complexity of the balance of plant (BoP), and the necessity for advanced and costly materials. As a result, the management complexity

of the system is heightened, accompanied by a significant increase in overall costs. To overcome these challenges, researchers have turned their focus to the reduction of operational temperatures in these devices. This attempt has given rise to the emergence of low-temperature solid oxide cells (LT-SOCs), which achieve a reduction in operational temperature to approximately 650°C. Nonetheless, challenges associated with this solution involve the compromise of certain benefits, especially those related to kinetics and activity that are typically associated with higher temperatures. Among these developments, another solution has gained substantial attention: PCCs. These cells present a viable potentially alternative due to their reduced activation energy for proton transport, which is roughly half that required for oxygen ion transport. The underlying equations governing their operational dynamics are delineated as follows:

Fuel cell mode:



Electrolysis cell mode:

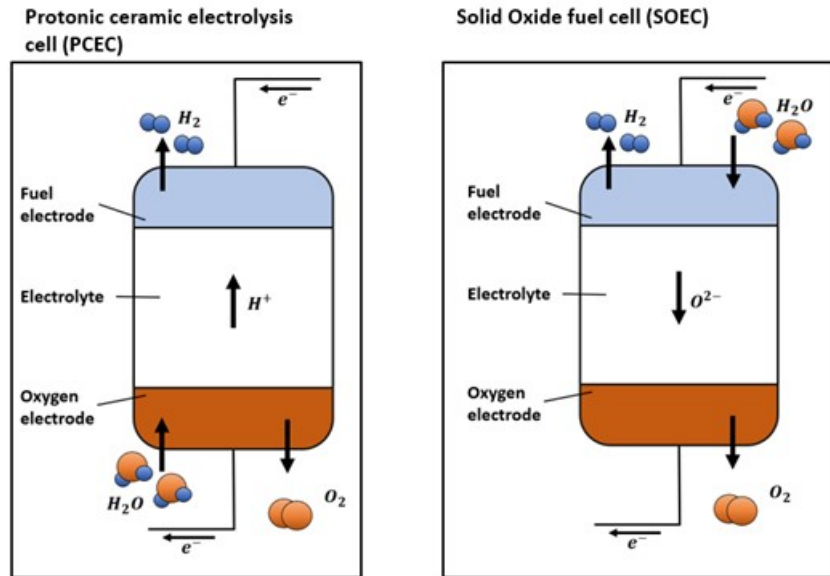
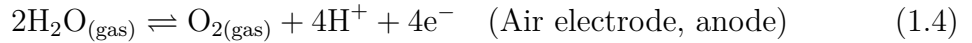
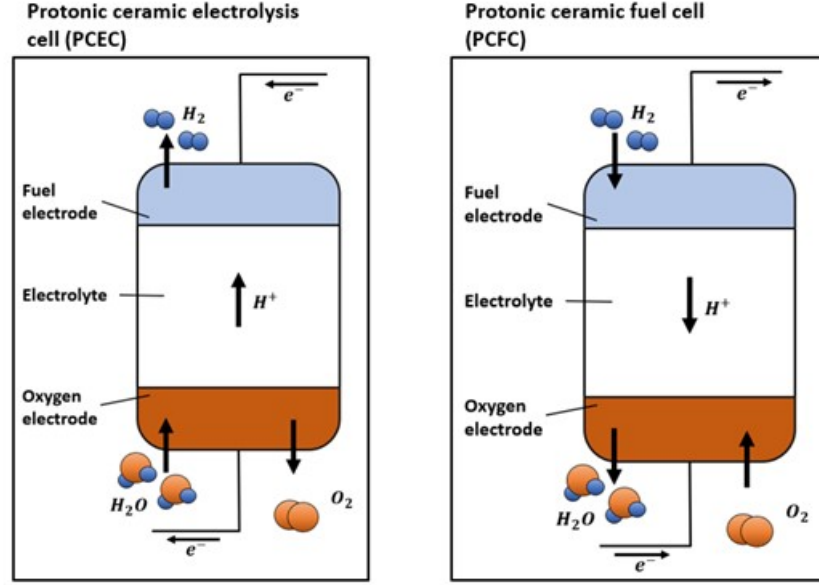


Figure 1.6: Difference between a SOC and a PCC in a electrolyser mode.



**Figure 1.7:** Two configuration for a PCC: a) fuel cell mode, and b) electrolysis mode

For the configuration of the electrolyser, which is of primary interest for the following study, there is an Air electrode, where a water vapor flow is supplied, and water molecules are electrochemically split into oxygen, electrons, and protons. These protons then travel through the ceramic electrolyte, eventually reaching the cathode (Fuel electrode). Here, the previously separated protons and electrons recombine, and a flow of pure hydrogen is produced at the output. The production of pure dry hydrogen simplify the process in comparison with SOECs, concept highlighted in figure. 1.6[15]. These devices can work also in fuel cells mode. In contrast to the previous scenario, this mode involves the oxidation of hydrogen at fuel electrode, followed by retracing the previous path in reverse, ultimately reaching the air electrode with the formation of water vapor. In figure. 1.7 are graphically reported the4 difference between PCFC and PCEC process.

### 1.3.1 PCC operation

The operation of a PCEC can be effectively represented by the i-V polarization curve, which shows voltage measurements as a function of current density applied to the devices. The operational voltage ( $V_{op}$ ) is calculated by considering the contribution of all overpotentials:

$$V_{op} = V_{eq} + \eta_{act} + \eta_{Ohmic} + \eta_{conc} \quad (1.6)$$

Vop like said is precisely the operational voltage, derived from the sum of various contributions, including  $V_{eq}$ , which is the equilibrium voltage, also known as open-circuit-voltage (OCV). The remaining components, as mentioned above, are overpotentials resulting from different causes.  $\eta_{act}$  is due to activation processes of the reaction,  $\eta_{ohm}$  is due to ohmic contributions, like ionic conduction in the electrolyte, and finally,  $\eta_{conc}$  is caused by mass transport phenomena. In the polarization curve, overpotentials are highlighted, each with specific areas of influence. It's important to note that these phenomena are always present during cell operation; each of them simply has a greater influence on a particular operating section. The OCV can also be calculated using the Nernst equation as follows:

$$V_{eq} = V^0 + \frac{RT}{2F} \ln \left( \frac{p_{H_2} \sqrt{p_0}}{p_{H_2O}} \right) \quad (1.7)$$

where  $V^0$  represent the potential under standard conditions,  $F$  is Faraday's constant,

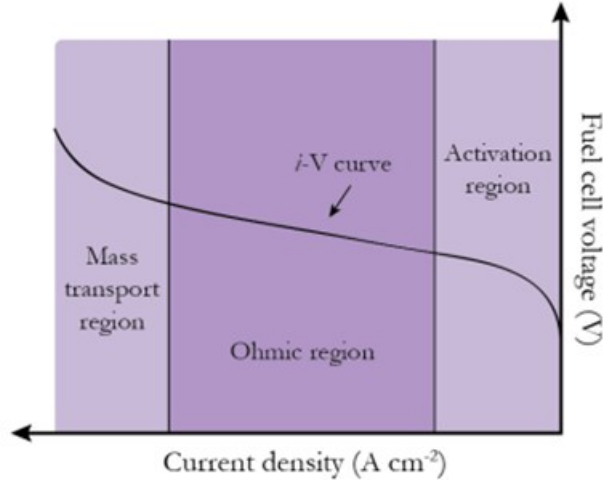


**Figure 1.8:** Polarization i-V curve for electrolysis configuration. The over-voltage losses zones are highlighted [9].

$R$  is the universal gas constant,  $T$  is the temperature, and the  $p_i$  represent partial pressures of the different  $i$  components of the reaction at the electrodes. Through Faraday's equation, it is possible to derive the theoretical hydrogen production:

$$x_{produced} = \frac{|i|}{nF} \quad (1.8)$$

where " $i$ " is the current applied to the cell, and  $n$  is the number of electrons involved in the redox reaction. Additionally, a power curve can be obtained by multiplying the measured voltage with the applied current.

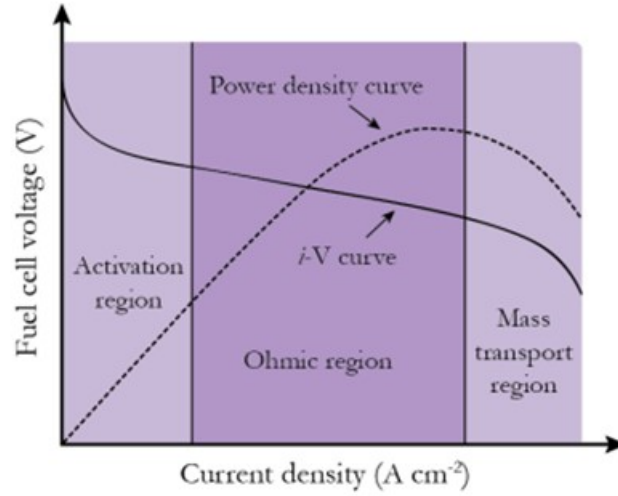


**Figure 1.9:** Polarization  $i$ - $V$  curve for fuel cell configuration. Also in this case the over-voltage zones are highlighted, and is also present a dotted line representing the power density curve[9].

### 1.3.2 State of the art materials for PCEC stack

The stack is the set of components that make up an electrolyser. It's the assembly of electrochemical cells in series, in order to increase the final power output, compared the single cell case. Numerous studies have been conducted over the past decades concerning the single cell, yet only a few concerning to a complete stack. Several reasons underlie this gap, related to unresolved issues inherent to this specific type of cell. Given the requirement for assembling cell stacks to make this technology industrially viable, further research are needed. This section briefly introduces all the components present inside a complete stack: the cell (electrodes and electrolyte), interconnector, and the sealants.

#### Electrodes

Electrodes are the components where the redox reaction take places, in the triple phase boundary (TPB) region, where there is the simultaneously presence of gas, electrode, and electrolyte phase. For this reason, their materials must exhibit specific characteristic, including the conduction of electron,  $O^{2-}$  ions, and protons. Moreover, they should be porous to allow flow of the gas. The necessary characteristics for these materials are the following[16][17]:

1. Good chemical stability.
2. High values of electron, ion, and proton conduction.

3. High porosity. This should be  $>30\%$ , to facilitate the diffusion of gaseous species within it, reaching the active zones.
4. Coefficient of thermal expansion (CTE) compatible with that of the other components they are in contact with (interconnectors, electrolytes, and sealants).
5. High catalytic activity. This is crucial for reducing polarization resistance, by enhancing oxidation and reduction reactions.

In the case of air electrode, exist four typology of conductive material utilized: pure electronic conductor, mixed protonic-electronic conductor (MPEC), mixed ionic-electronic conductor (MIEC), and triple protonic-electronic-ionic conductor (THOEC)[18]. The first category includes, like the name suggest, material with the capability to conduct only electrons (figure. 1.11a). From them there are Lanthanum strontium manganite  $\text{La}_{0.8}\text{Sr}_{0.2}\text{MnO}_3$  (LSM), and simple platinum (Pt), which is however too expensive. The problem with LSM is that the optimum, in terms of performances, is reached at high temperatures, like  $800^\circ\text{C}$ , so the aim to reduce the operative temperature of the cell would lead to a decrease of electrons conductivity[18]. MPEC conducts protons and electrons, such as represented in figure. 1.11c expanding the active area for the electrochemical reaction[18]. Examples of materials are doped  $\text{BaCeO}_3$  or BCZY-LNF. One of the most used typologies of air electrode material is MIEC, figure. 1.11b. They allow the conduction of electrons and oxide ions, thanks to the vacancy hopping process, facilitate by the large number of vacancies present into this material[18]. This led to great performances in

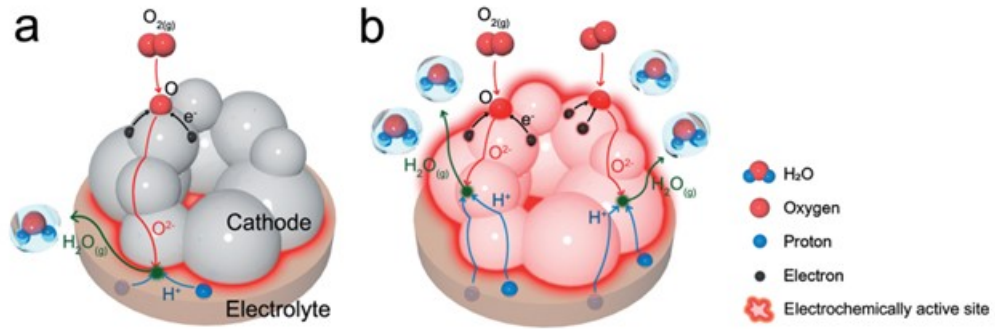


**Figure 1.10:** Representation of the active area in the cathode, in the case of MIEC (a) and TCO (b) material[19].

both electronic and ionic conduction, and to a good catalytic activity. State-of-the-art materials includes  $\text{La}_{0.6}\text{Sr}_{0.4}\text{Fe}_{0.8}\text{Co}_{0.2}\text{O}_{3-\sigma}$  (LSCF),  $\text{Ba}_{0.5}\text{Sr}_{0.5}\text{Co}_{0.8}\text{Fe}_{0.2}\text{O}_{3-\sigma}$  (BSCF),  $\text{Sm}_{0.5}\text{Sr}_{0.5}\text{O}_{3-\sigma}$  (SSC) and yttria-stabilized zirconia (YSZ)-lanthanum strontium manganite (LSM) composite [15]. Despite that, they don't represent

the best solution for PCC technology, as the proton conduction is restricted to the interface area with the electrolyte. This highlights the necessity of materials with also a good conduction of protons, figure. 1.10d. THOEC materials present a mixed ion, proton, and electron conduction, which expand the active area of the electrode, and consequently improving the performance [20][18] Figure.tot represent through a schematic diagram the conduction behaviour of a MIEC electrode, compared with a THOEC one. For what concern fuel electrode, different solutions were tested, like single-phase graphite, platinum, iron, cobalt, and nickel. However, all of them have presented some issues [17][21]. Indeed, graphite is susceptible to corrosion, Pt shows a good stability and catalytic performance, but fail on the bonding with the electrolyte, due to the formation of water vapor in the interface [21]. For transition metal, iron also have corrosion problems, and cobalt is too expensive [21]. Ni had been used for several years like anode, but its thermal expansion coefficient considerably differ from the electrolyte materials one[17]. As alternative to single-phase electrode, “cermet” began to be used. Cermet is a porous composite of an electronic conductor material (metal) and a protonic conductor material (ceramic)[21]. The most common is nickel-zirconia cermet. In that case, Ni phase provide the electronic conductivity and catalytic activity needed, and zirconia lowers the CTE of the composite, making it compatible with the electrolyte. The overall effect is to increase the active area for the reaction, and consequently enhance the efficiency[17]. Some examples of other ceramic material utilizer are:  $BaCe_{1-x-y}Zr_xY_yO_{3-\sigma}$  (BCZY) or  $BaCe_{1-x-2y}Zr_xY_yYb_yO_{3-\sigma}$  (BCZYb). Indeed, possible solution are represented by NiO-BCZYb or NiO-BCZY[9][6].

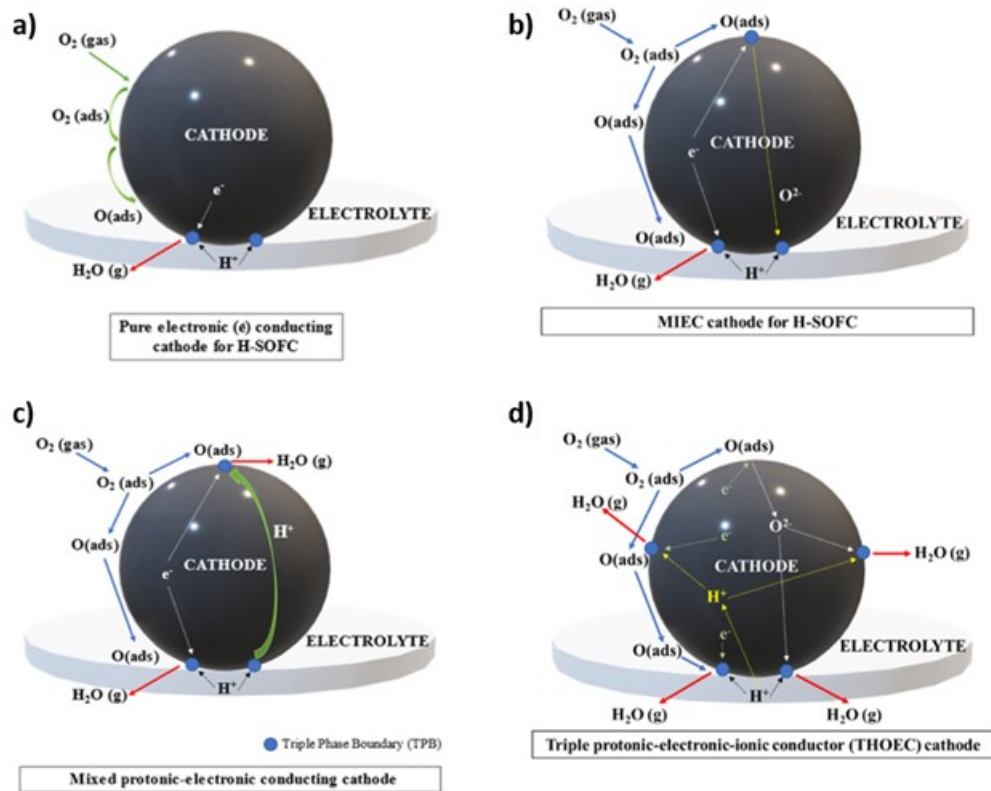


**Figure 1.11:** Schematic representation of the conduction of different charged species, considering the four main typology of air electrode materials: a) pure electronic conductor, b) MIEC, c) MPEC, d) THOEC.

## Electrolyte

The electrolyte constitutes a crucial layer within cells, serving to separate the two electrodes where redox reactions occur. This necessitates specific characteristics enabling it to function in contact with both atmospheres while maintaining excellent ionic conductivity. Below are outlined several essential characteristics for defining a good electrolyte:

1. **Effective gas tightness:** The electrolyte's primary role is to act as a membrane separating the two semi-reactions. It's therefore critical to prevent gases leakage, from one electrode to the opposite, which could degrade cell efficiency. This underscores the need for the electrolyte material, in this case ceramic, to be highly dense even at relatively low sintering temperatures. Detailed insight into the challenges of low-temperature sintering can be found in articles on the topic[22].

2. High ionic conductivity: The goal is to minimize the ohmic resistance due to ionic conduction, thereby enhancing cell performance. This can be achieved by reducing the electrolyte layer's thickness or using materials with elevated ionic conductivity.
3. Low electrical conductivity: While reducing resistance for ionic conduction is essential, the passage of electrons through the electrolyte layer must be avoided as it leads to short-circuiting, significantly diminishing efficiency.
4. Thermodynamic compatibility with other stack components: During operation, the electrolyte remains in contact with the two electrodes and the sealant. Hence, the thermodynamic characteristics of the materials must be compatible to avoid cracks, deterioration, efficiency loss, and reduced stack lifetime.

Among potential materials for proton-conductive electrolytes are certain families of perovskites, such as ABO<sub>3</sub>-based compositions. Previous studies have highlighted the excellent results in terms of ionic conductivity and low activation energy. The current state-of-the-art is represented by materials with barium in the A-site and cerium/zirconium in the B-site (*BaCeO<sub>3</sub>* and *BaZrO<sub>3</sub>*) [20]. However, these materials also exhibit operational challenges. *BaCeO<sub>3</sub>*-based electrolytes prove chemically unstable in atmospheres containing *H<sub>2</sub>O* or *CO<sub>2</sub>*, leading to the formation of hydroxides and carbonates, respectively, due to Ce's basic nature [23][24]. This issue is not encountered in *BaZrO<sub>3</sub>*-based oxides, which remain stable in such atmospheres under operational conditions, particularly when doped with Ytria. However, the challenge with these materials lies in the need for high sintering temperatures, resulting in a high number of grain boundaries with elevated protonic resistance [25]. As mentioned earlier, the addition of Y to both oxide families leads to enhanced performance. This gives rise to BCY and BZY, exhibiting increased conductivity and improved chemical stability. Building on this premise, the exploration led to the attempt of combining these two, forming a solid solution encompassing both elements. The idea behind this experiment comes from the intention to find a trade-off between the limited stability of Ce-containing oxides and the conductivity issues observed in Zr-containing ones, by altering the Ce/Zr ratio inside the composition *BaCe<sub>1-x</sub>Zr<sub>x</sub>Y<sub>0.1</sub>O<sub>2.95</sub>* ( $0 < x < 1$ ). The outcome is BCZY, which demonstrates favourable conductivity values and robust chemical stability, making it a widely utilized material for these applications. Ongoing composition optimizations are underway through doping with various elements like Yb, requiring further research to better understand the link between composition, structure, and resulting performance. For further information on this subject, refer to the following articles [26][27][28]. Figure. 1.12 shows the ionic conductivity of different electrolyte materials, as function of the temperature. Is possible to notice the positive impact of temperature increase on conduction.

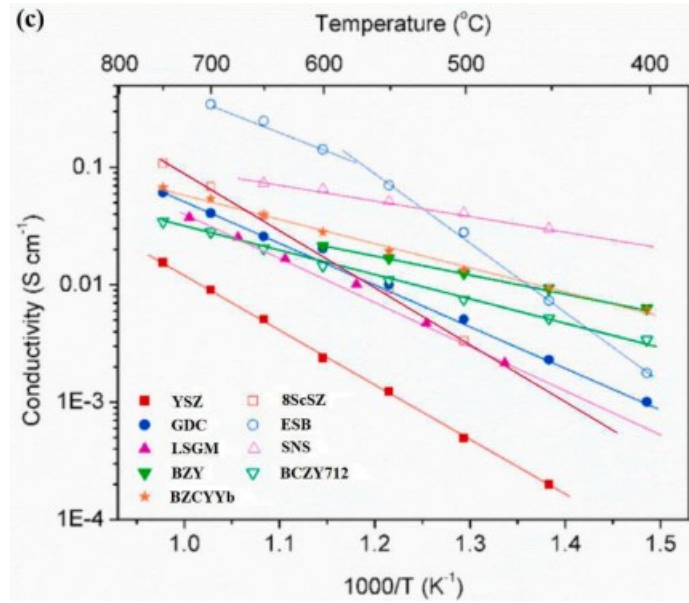


**Figure 1.12:** Ionic conductivity of different electrolyte materials, function of the temperature[29].

### Interconnector

To develop a PCC stack, the selection of a suitable interconnector is of primary importance, as it must be compatible with the other materials, in particular atmosphere and temperature conditions. Indeed, for PCFC and PCEC, the interconnector is exposed to an atmosphere composed of pure hydrogen, and another one of steam and oxygen. This led to a rapid degradation of the materials. The role of this component is to guarantee an electrical connection between a fuel electrode and an oxygen electrode, belonging to neighbouring cells, and to separate the two environments (reducing and oxidating zone). Like other materials, it must fulfil some conditions: 1) it must exhibit excellent electric conduction; 2) should have a good stability (in terms of chemistry, microstructure, and dimension), in the operative conditions; 3) must show low permeability to gas (hydrogen and oxygen), in order to avoid diffusion between the atmosphere; 4) need a CTE comparable with other components is needed; 5) have to avoid reaction with other components; 6) should have a good thermal conductivity; 7) must have quite good resistance to oxidation; 8) should be easily producible, in order to simplify the industrial scal production; 9) need good resistance to thermal stress, avoiding degradation[30]. The most used materials for similar application are high temperature alloy, thanks to their oxidation resistance at high temperature conditions. they can be classified into Ni-, Fe- and Co-based superalloys, Cr-based alloys and stainless steels. The

resistance to oxidation is due to the presence of Cr and Al, that led to the generation of  $Cr_2O_3$  and  $Al_2O_3$  protective layers[31]. That's also represent an issue, driving to a voltage loss. For this reason, critical maximum of Al and minimum of Cr are considered in the interconnector choice. The super alloys were developed for elevated temperature purposes, and they are characterized by a FCC matrix and secondary phase. Cr-base alloys don't have Al, and because of that they don't need maximum Al content study. They are characterized by a body-centered-cubic (BCC) structure. In the end, there are stainless steel alloys, that include a wide range of alloys, characterized by hih oxidation resistance[31]. Today, for the SOCs applications, ferritic stainless-steel alloys are the state-of-the-art, often with the addition of a coating materials[32]. For PCC also FSS seems to be the best solution in terms of compatibility with the other components. Further study about it are still needed[32].

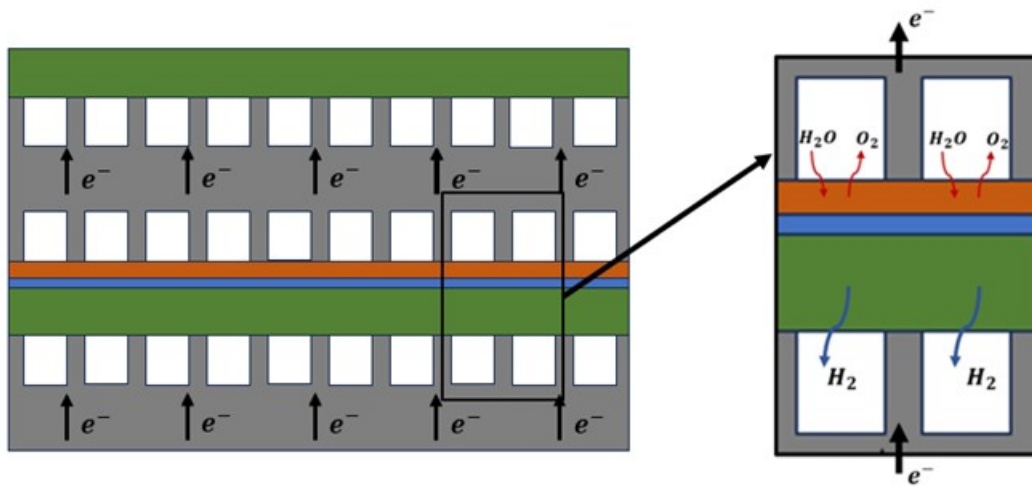


**Figure 1.13:** Diagram of a portion of stack for a PCEC. Is possible to notice the aim of the interconnector, which allow the diffusion of the gas, through the channel, in and out of the electrodes, and represent a pathway for the electrons. The cell is portrayed with the following colors: Fuel electrode (green), electrolyte (blue), and air electrode (red).In the right there is a magnification of the boxed zone. The proportion are not observed here for a simpler comprehension.

### Sealant

Sealant materials are utilized in stacks to isolate the various components (electrodes, electrolyte, and interconnector) from gas leakage and under the electrical point of view, preventing from shunting. Following figures ( 1.14), help to understand the location where this component is needed, for a planar configuration [33]. The main

requirements for sealings materials are the following: 1) CTE comparable with the one of the sealed materials; 2) thermal stability in the operational temperature range (500-600°C); 3) good resistance to chemical composition change, avoiding reaction due to the exposure to reducing and oxidizing atmosphere; 4) resistance to thermal cycling failure during start-up and shut-down; 5) good electrical resistivity at operating temperature; 6) must avoid gas leakage; 7) low cost and flexible design. Nowadays three main type of sealing materials are used and studied: compressive sealant, compliant sealant, and rigidly bonded sealant. The first type is composed by materials deformable under pressure application. It isn't bounded with the components, but only adhering to them, reducing the influence of CTE to the performance. Indeed, deformations due to de differences of CTE with other materials are absorbed from the sealant, and don't generate cracks. Examples of these sealing materials are mica, mica-based, ceramic fiber-based, and  $Al_2O_3$ -based seals. Also, compliant sealant are deformable materials, but in this case only noble materials are used, like platinum or gold. Considering the high cost of the latter, other materials were investigated, like silver and copper. For these two categories of sealing materials some issues have been encountered, such as cracks and deterioration during the operation, gas leakage and corrosion phenomena. At the end there are rigidly bonded seals, also known as glass and glass-ceramic seals. They represent the best solution for this type of application. Differently from the other, these materials form a chemical bond with the components, allowing to obtain higher performance in the prevention of gas leakage. Main advantages of this type of seal are the ability of flow over the cell, forming a hermetic adhesion, and the possibility to tune the glass composition, modifying the properties. In addition to these, however, there are also a lot of study to develop in this field, trying to satisfy all the requirements [33].

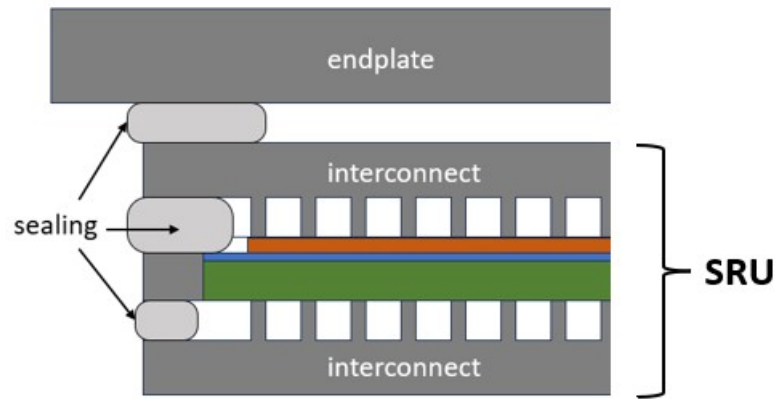


**Figure 1.14:** This diagram shows the possible position of the sealant for a PCEC stack.

## 1.4 Glass and glass-ceramic seals

Glass and glass-ceramic sealants are very common in the field of SOEC, due to the resistance to high temperature operation and to possibility to tune their properties changing their composition. Indeed, modification of the glass network structure can lead to important modifications of the material behaviour. Here is reported a summary of the main components of a glass structure, and their impact on the characteristics. In glass structure are present network formers, intermediates, network modifiers, and additives. Between formers, oxides of Si and B are the most common, and can be alone or combined. From network modifiers instead, are included alkaline and alkaline earth oxides, such as  $Li_2O$ ,  $Na_2O$ ,  $BaO$ ,  $SrO$ , and so on. They are called modifiers because provide additional oxygen ions, modifying the structure. Most common intermediate oxide is  $Al_2O_3$ . They can act like glass former or modifier, based on their participation in the glass network or not. Additives are not necessary component of the glass structure but are useful for the modification of the properties. Between these there are rare earth metal oxides ( $La_2O_3$ ) and transition metals such as  $ZnO$  and  $Y_2O_3$ [33].

### 1.4.1 Effect of composition on thermal characteristics

Here is briefly presented a summary of the main thermal properties of a sealing glass and their possible tuning through the modification of the glass composition. The properties considered are transition temperature ( $T_g$ ), softening temperature ( $T_s$ ), and CTE. The first two are related with the viscous behaviour of the glass. Glasses

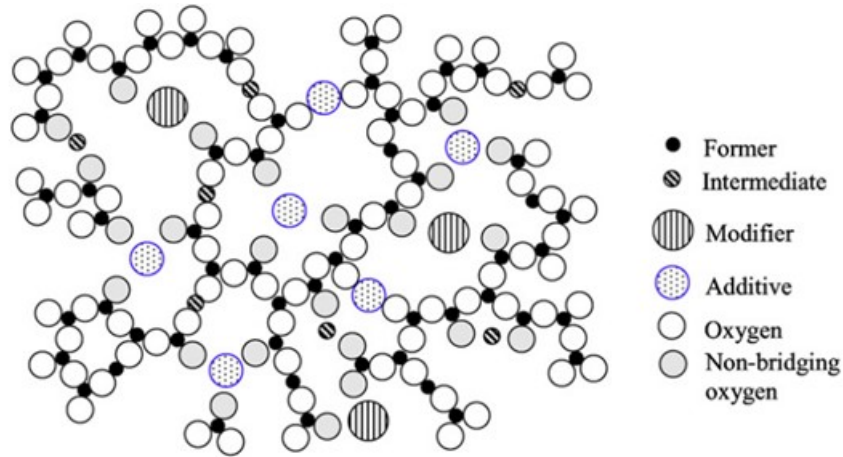


**Figure 1.15:** Representation of a glass network structure. All the possible type of glass network components are here reported[33].

are brittle below the  $T_g$  and viscous above it. Considering the requirement of a viscous behaviour of the glass, for obtain a good joining with the other components,  $T_g$  value must be lower than the operating temperature of the cell. This can lead to a decrease in thermal stress and possibility of obtaining self-healing cracks by a viscous flow [34]. At the same time,  $T_s$  should be higher than operational temperature, in order to avoid excessive glass flow[34]. Some paper works have highlighted the impact that composition modification have on glass behaviour. For example, in silicate glass, the addition on  $SiO_2$  lead to the increasing of  $T_g$  and  $T_s$ [35][34]. In the case of borosilicate glass,  $T_g$  and  $T_s$  decrease with the addition of  $B_2O_3$ , due to its own low  $T_g$ [36]. Is important to notice that the same oxide can play different role for different glass system.  $B_2O_3$  can increase  $T_s$  if added to a  $MgO$ - $BaO$ -silicate seal glass[34]. Not only network former changes drive to modification on behaviour, but also network modifiers also have an important role in it, that depends on their influence on glass structure. Adding modifiers into a glass forming oxide lead to a decrease of the characteristic temperatures, and if done on borosilicate glasses that have the opposite effect[34]. Particularly used for  $T_g$  and  $T_s$  tailoring are the additives, like  $ZrO_2$  and  $Al_2O_3$ . Mixing them to the glass powder bring to a composite seal [34]. Like for the previous, their effect must be well analysed case by case. CTE is another property that can be tuned. Particularly important in terms of thermomechanical compatibility of the components, it must be closest as possible to the value of the joining materials. Indeed, if at the interface the CTE of the seal is lower than the other, that lead to tensile stress. Otherwise, if is higher, that can drive to the formation of compressive stress in the glass. Previous research has established  $\pm 1 * 10^{-6} K^{-1}$  like difference

limit value. In this case the effect of network formers is simpler to understand. The addition of oxides with high CTE values increases the total CTE of the seal, like for  $B_2O_3$  ( $14.4 * 10^{-6} K^{-1}$ ), and the addition of low CTE oxides, like  $SiO_2$  ( $0.6 * 10^{-6} K^{-1}$ ), decrease it. For network modifiers and additives, the trends are again dependent on seal composition and other factors. Further insights are provided in other paper works[6][34].

### 1.4.2 Additive manufacturing

Fundamental step, after the definition of the material, is to introduce the process utilized to deposit the glass-ceramic paste on the cell. Indeed, the reaching of optimum performances during the deposition process, is pivotal for the correct functioning of the entire technology. The process briefly introduced is the Additive manufacturing (AM). AM include different method for the 3D printing of a material, adding layer by layer. Usually utilized for the deposition of deposition of polymeric and metallic material, it could be used to also print ceramics. This is particularly challenging as these materials are characterized by high melting points[37]. Seven

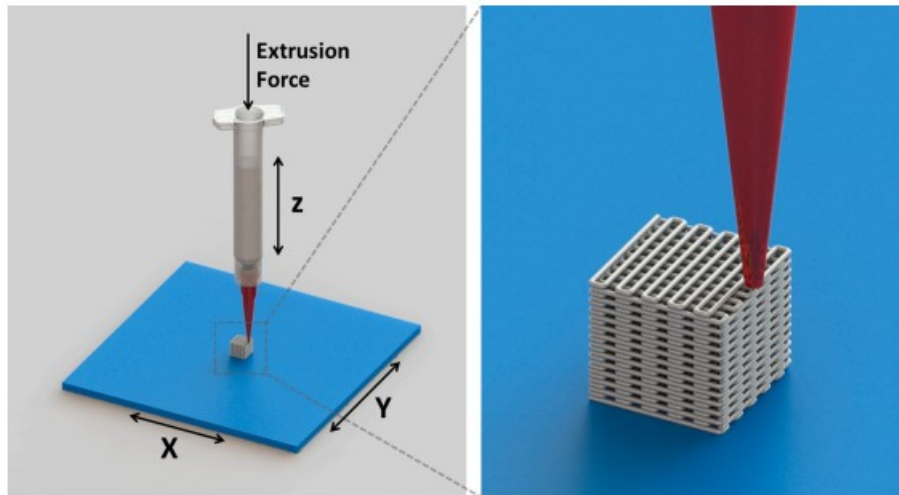


**Figure 1.16:** Additive manufacturing process of robocasting. This typology of process allows the deposition of an ink to the surface, thanks to a s pressure applied (extrusion force) that drives the in k through a nozzle[37].

different AM methods are defined: extrusion, material jetting, binder jetting, photopolymerization, powder bed fusion, sheet lamination, and direct energy deposition [38]. Focusing on material extrusion, this is a technique were a mixture of ceramics and a solvent is forced through a nozzle. There are several methods to print a ceramic, including: vat polymerization, powder bed-based methods or

material extrusion. In particular, extrusion via robocasting proved to be the most convenient choice for the on-demand deposition of glass ceramic layers. This is based on the extrusion of a ceramic paste through a nozzle. This option brings some advantages like the rapidity and ease to develop structures and the relatively low cost[37]. This technology utilizes a ceramic ink, composed by a suspension of ceramic particles, also known as paste or slurry. This is what represents one of the greatest challenges for the application of robocasting method. Indeed, the design of the ink require a high ceramic charge, for minimize shrinkage, a good homogeneity of the paste and suitable rheological properties for the extrusion and deposition process[37]. For the deposition, robocasting pastes should fulfil some requirements. Indeed, the paste must be extrudable, avoiding uneven molding, and have shape-retention capacity, that allow to maintain the shape after the deposition. This means that the behaviour of the ink must be like a fluid for the extrusion step, and elastic after that. For describe the previously mentioned behaviour, different equations are used, like Ostwald-de Waele power law (eq. 1.9), and the equation of the apparent viscosity(eq. 1.10), that together gave the eq. 1.11.

$$\tau = k(\dot{\gamma})^n \quad (1.9)$$

$$\eta = k(\dot{\gamma})^{n-1} \quad (1.10)$$

$$\tau = \eta(\dot{\gamma}) \quad (1.11)$$

These equations show the relationship between shear stress ( $\tau$ ), shear rate ( $\dot{\gamma}$ )and apparent viscosity ( $\eta$ ). Where  $k$  is the flow consistency parameter and  $n$  the flow behaviour index, that is  $n = 1$  in case of Newtonian material (independency of the viscosity from shear rate),  $0 < n < 1$  for shear-thinning material (pseudoplastic), and  $n > 1$  for shear-thickening (dilatant) [37]. As shown in figure. 1.17 the viscosity for the shear-thinning materials decreases as the shear rate increase. Instead, completely opposite behaviour is shown by the shear-thickening materials. Additionally some pastes may follow the Herschel-Buckley model (eq. 1.12), starting to flow only after the exceeding a critical level for the shear stress. This limit stress is known as yield stress ( $\tau_y$ ).

$$\tau = \tau_y + k(\dot{\gamma})^n \quad (1.12)$$

Figure. 1.18 presents a schematic of the ink extrusion process. One can be observe the different solicitation that the paste should adapt to. Is possible to define a first rest state zone inside the syringe, a second region that present a fast acceleration of the paste, the nozzle where the maximum velocity is reached, and the deposition region where the paste rest again. For the nozzle region a good flowability of the ink is required, guaranteeing so a shear-thinning behaviour. Indeed, this part of the process need a reduction of the viscosity in correspondence of a highly increase of the shear rate. After that, in the second rest region, a fast recovery is needed,

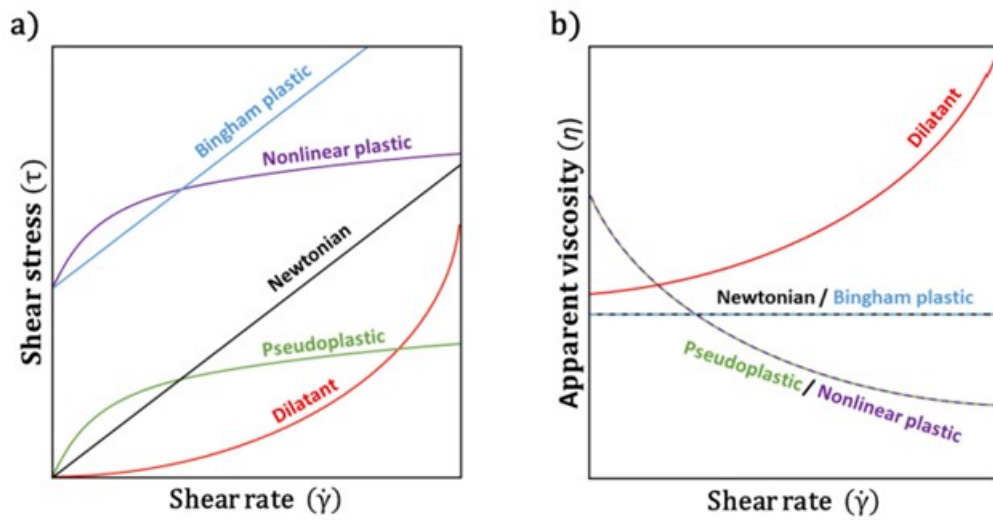


**Figure 1.17:** These curves report the response behaviour of different type of materials to the application of a shear rate. a) shear stress versus shear rate, b) apparent viscosity versus shear rate [37].

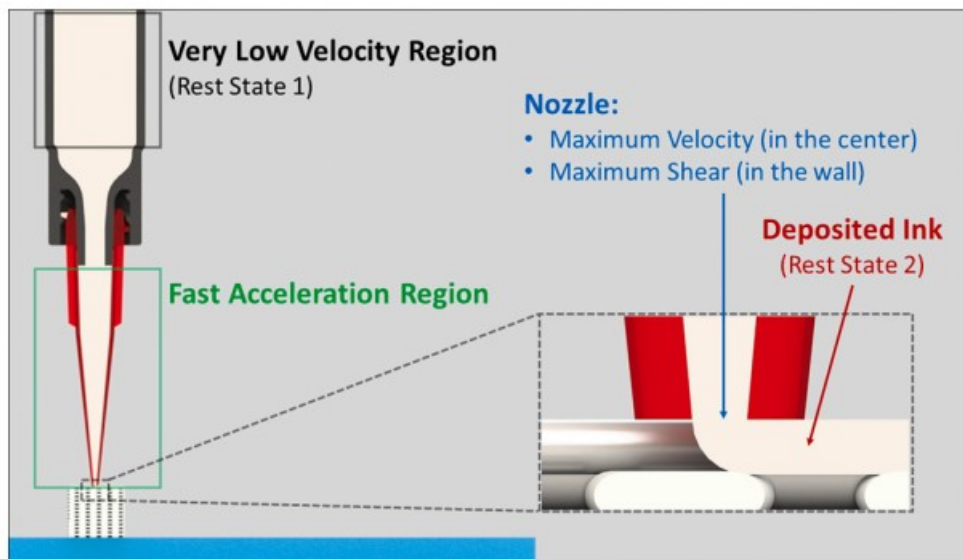


**Figure 1.18:** Diagram of ink extrusion through a nozzle, during a robocasting process [37].

allowing to obtain an appropriate shape retention, and a self-supporting capacity by the paste. Figure Y shows different types of robocasting syringes. In figure Ya, b, and c the pistons are respectively moved by a screw, in an infinite screw that

push the paste and is moved by compressed air.

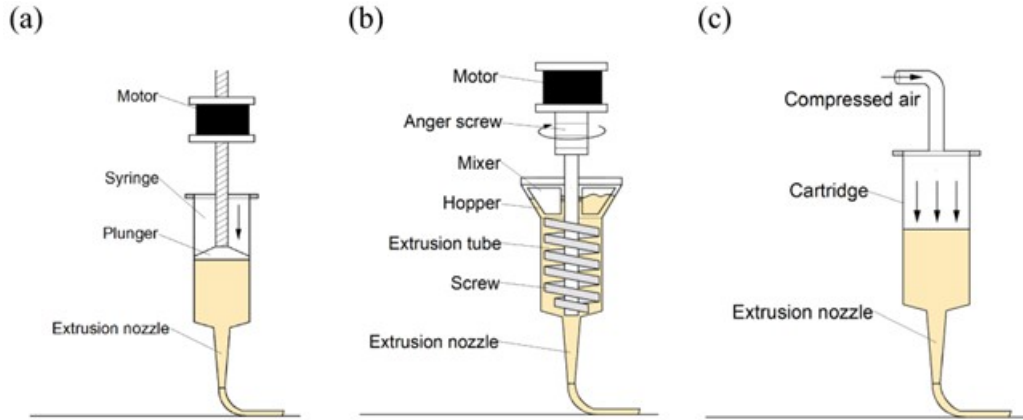


**Figure 1.19:** Diagram that represent the three different configurations used during the paste extrusion in a robocasting process. An electric motor can be utilized for drive a piston (a) or a screw b). Alternative solution implies the utilization of compressed air [39].

### 1.4.3 Ceramic inks

Ceramic inks can be formed by colloidal suspensions, and gel-embedded suspensions. The first ones present a high concentrated slurry of solid particles, with a weight percentage in the range of 60-80%wt. They are dispersed in a liquid and low viscosity solvent, and with the addition of a small fraction of organic additives that allow to optimize the interaction forces between particles, stabilizing them. Instead, gel-embedded suspension differs from the first category for the source of the rheological properties. Indeed, if in the previous case the properties were influenced by the particle's interactions, in this case they depend on the gel phase, in which the particles are dispersed[37]. This category can also be divided in two different types: hydrogel ink and organogel ink. Adding additives is fundamental to tune the rheological properties of a slurry. Additives can have multiple functions, e.g., they can work as dispersants or as binders. Dispersants are mainly polymeric materials, which are adsorbed on the surface of the ceramic particles. This allows to overcome van der Waals interparticle forces and to obtain a homogeneous structure. The mechanisms that permit to stabilize the ink are electrostatic steric, and electrosteric mechanism (figure. 1.21)[9][40]. Binders also are mainly composed by polymer, with a high molecular weight, used for increasing the viscosity and drive to a joining between the particles. The tuning of this additives inside the paste is one of the most important steps of the process, in order to allow their elimination through

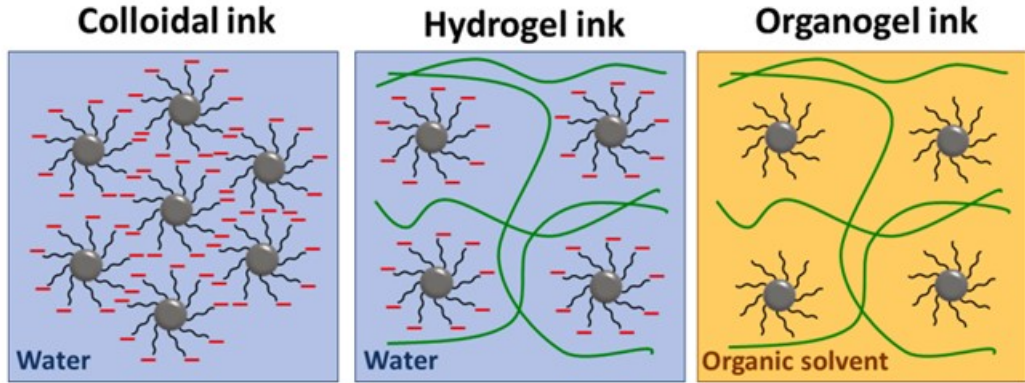


**Figure 1.20:** Diagram representing three main type of ceramic inks for robocasting. The steric mechanism is here represented by black lines, connected to the particles. The negative charges are pictured in red, and the polymer chains are drawn like green lines [40].

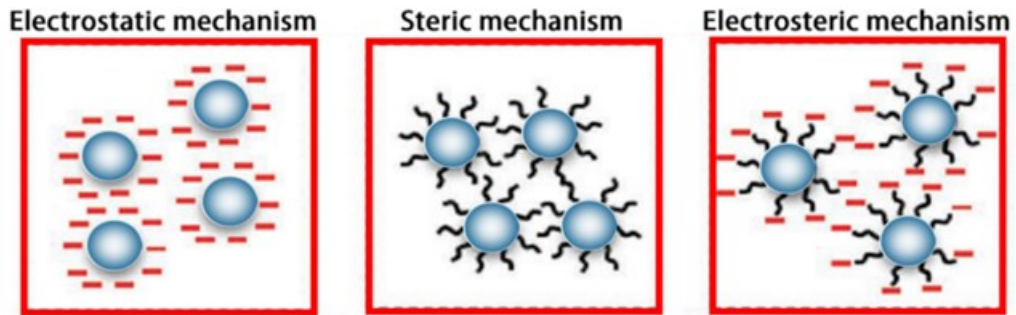


**Figure 1.21:** Three main mechanisms for particles stabilization: electrostatic, steric, and electrosteric. Steric interactions are represented by black lines, while electrostatic interactions by negative red charges [40].

thermal treatment, avoiding the formation of cracks in the final microstructure [40].

## 1.5 Goal of the thesis

This thesis aims to increase the knowledge in the field of stack of large area, Proton Conductive Cells. The reasons behind the improving attentions to this technology are related to its ambitions on solving all the challenges highlighted in the case of Solid Oxide Cells (SOCs), like lowering the operational temperature, and consequently allow to the utilization of cheaper materials, impacting on the

overall system cost. To reach the final stack, however, substantial efforts remain necessary to gain a deeper knowledge on the thermochemical compatibility of various components. This includes identify optimal materials and investigate their interactions within the temperature range of interest, which in this case is between 550-600°C. Specifically, this study aims to delve deeper into the glass-ceramic sealant component, evaluating different glass compositions and conducting various tests to thoroughly characterize them. Once accomplished, the analysis extends to the interaction between these glasses and the other components that will ultimately form the stack, aiming to identify any potential undesired effects. Within this context, the study also introduces the robocasting deposition process, an automated moulding methodology that streamlines the sealant deposition phase, rendering it readily scalable for industrial applications. Naturally, this entails additional glass analysis, focusing on viscosity and the rheological behaviour of the paste used for cell deposition. Ultimately, in the pursuit of a comprehensive model simulating the system's behaviour, a basic 2D numerical model has been developed to begin assessing the cell's thermo-mechanical behaviour.

# Chapter 2

## Experimental Methods

### 2.1 Glass-ceramic preparation

During this work, four glasses were analysed, with three being designed and produced in the laboratory of the Politecnico di Torino as part of previous studies. These are V10, V11, and GC2. The fourth glass, GM31107, is a commercial glass provided by SCHOTT and was initially tested as received. For what concern the BCZY utilized in this work, three different compositions were taken in consideration (tab. 2.1), but for the joining sample only one was utilized ( $BaZr_{0.625}Ce_{0.2}Y_{0.175}O_{3-\sigma}$ ), because it presents the state of the art for electrolyte in these applications.

#### 2.1.1 Composition of the glasses and casting procedure

Three of the considered glass-ceramica system are Si-based (V10, V11, and GC2), while the commercial glass is Ba-based. A more detailed description is provided in the following table (tab. 2.2). During the laboratory work, two of the examined

Type of BCZY	Composition
BCZY-1	$BaZr_{0.625}Ce_{0.2}Y_{0.175}O_{3-\sigma}$
BCZY-2	$BaCe_{0.7}Zr_{0.2}Y_{0.1}O_{3-\sigma}$
BCZY-3	$BaZr_{0.3}Ce_{0.6}Y_{0.1}O_{3-\sigma}$

**Table 2.1:** Three different BCZY considered, with their composition and nomenclature utilized inside the work.

glasses, GC2 and V11, were prepared to being used in the conducted tests. The casting process involves blending various precursors in precise weight percentages in a plastic bottle, which is then left on a roller overnight to achieve a homogeneous powder. To prevent the formation of clumps, the powder can be ground in a mortar using a pestle. Then, the powder is transferred to a platinum crucible, closed with a platinum lid, which is subsequently placed in a furnace (Nabertherm). The thermal cycle requires reaching 1500°C before the crucible is inserted. After 30 minutes, the furnace is opened, the lid is removed, and the crucible is placed in the furnace for an additional 30 minutes. The entire thermal treatment lasts for an hour. The glass labelled as GC2 is casted directly on a metal plate. For the glasses V10 and V11 a quenching process is required. The melted glass is deposited into a container of deionized water. After cooling, the glass is collected and placed in an 80°C oven overnight to eliminate any remaining moisture. Once this is done, the glasses are grounded, using a miller with a zirconia ball, and sieved to achieve particle sizes below 25 $\mu$ m.

Oxydes	V11	V10	GC2	GM31107
<i>SiO<sub>2</sub></i>	46.37	49.30	38.21t	1-10
<i>Al<sub>2</sub>O<sub>3</sub></i>	8.34	8.30	4.72	10-50
<i>CaO</i>	14.34	14.30	4.54	1-10
<i>B<sub>2</sub>O<sub>3</sub></i>	5.76	5.80	6.44	10-50
<i>Na<sub>2</sub>O</i>	9.26	9.30	-	-
<i>MgO</i>	16.00	13.00	-	-
<i>ZrO<sub>2</sub></i>	2.92	-	-	-
<i>BaO</i>	-	-	46.09	>50

**Table 2.2:** Evaluated glasses composition

## 2.2 Paste preparation

Another step in this study involves the utilization of an automated deposition method for the sealant. The aim is to optimize the deposition process on the cell and make it scalable for industrial purposes. However, this necessitates the development of pastes suitable for molding, with specific rheological characteristics that maintain the sealant’s application requirements. In this work, two distinct

pastes were developed, differing in the organic components used. The first and most

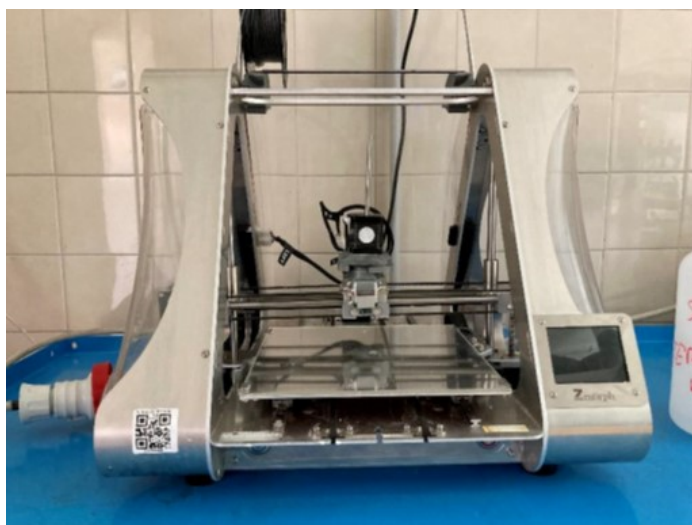


**Figure 2.1:** Robocasting instrument utilized for the paste deposition (ZMorph S.A. Company)

frequently employed paste during testing is the propylene glycol (PG)-based paste. PG is a viscous hygroscopic organic solvent with low toxicity. Along with PG, two additional components, a dispersant, and a binder, are added. For this paste, PVP K30 and K90 are respectively used as the dispersant and binder. Both are long chain polyvinylpyrrolidones. The formulation process for this paste involves pre-mixing these two components separately with PG, each at a weight percentage of 5%. K30 is completely poured into a container containing PG, and the mixture is mechanically stirred for 15 minutes at 300 rpm. For K90, it is recommended to divide it into three portions, which are added to the PG-containing container, with intervals of 15 minutes of mixing at 300 rpm. These two containers are then placed on rollers for two days to achieve as homogeneous a distribution as possible. Once this is done, the two containers are mixed with the remaining PG for 15 minutes at 600 rpm, using a mechanical stirrer. Following this, the solid component, in this case the glass for which the paste is being formulated, is added, divided into 3-4 portions to prevent the formation of lumps. Again, between each portion of glass, the mixture is stirred for 10-15 minutes at 600 rpm. The composition of the paste used in this work is presented below tab. 2.3. Similar considerations can be made for the terpineol-based paste, analogous to the previous case.  $\alpha$ -Terpineol (Carl Roth GmbH + Co. KG, Karlsruhe, Germany) is a tertiary alcohol used as an organic solvent for paste preparation. Here, too, a dispersant and a binder are present, which are Targon and ethyl cellulose, respectively. In this case, the binder EC is initially mixed with terpineol. The percentage of EC used is 3% relative

Material	Amount (%wt)
Solid load	75.00
PG	5.00
PG + K30	15.00
PG + K90	5.00

**Table 2.3:** PG paste composition (%wt).

Material	Amount (%wt)
Solid load	75.00
Terpineol	23.5
Targon	0.75
EC	0.75

**Table 2.4:** Terpeneol paste composition (%wt).

to the solvent. The two components are then mixed using a mechanical stirrer for 20 minutes at 700 rpm. Once this is done, the dispersant is added as well, at a percentage of 1% relative to the solvent, followed by mixing for 10 minutes at 700 rpm. Like the previous case, the solid loading is then introduced in 3-4 portions, with intervals of 10 minutes at 800 rpm. To ensure proper distribution of the various components, an additional mixing step of 20 minutes at 700 rpm is performed. The composition of the paste used in this study is outlined below tab. 2.4.

### 2.2.1 Glass modification

With the aim to improve the performances of the commercial glass, changes on the composition were made. In this case, a zirconia oxide, doped with yttria (YSZ), was used for the purpose. Test were made on GM31107 with the addition of 3YSZ and 8YSZ, differentiated by different molar content of yttria (3 and 8%mol respectively). The aim was to allow the generation of a crystalline phase in the glass, improving the performance and modifying viscosity and CTE[41]. First step was to evaluate the particle size of the two YSZ, in order to characterize them. Aiming to ensure a good dispersion of the YSZ particles within the glass and avoid agglomeration, glass and YSZ powders have been dispersed in a solvent. 8YSZ was poured into a test tube, with 5%wt fraction of the solid load, before the glass, allowing the dispersant to act on it. For this test, PG paste was utilized.

## 2.3 Rheological characterization of ceramic inks

After the preparation, the paste is tested using a rotational rheometer, that allow to apply a wide range of shear stresses and rates to a sample, also controlling the environment conditions. There are different configurations and test mode, but in this case the paste was tested using a parallel plane, rotational mode (figure. 2.2). This test is particularly suggested and used for the characterization of ceramic pastes [37].

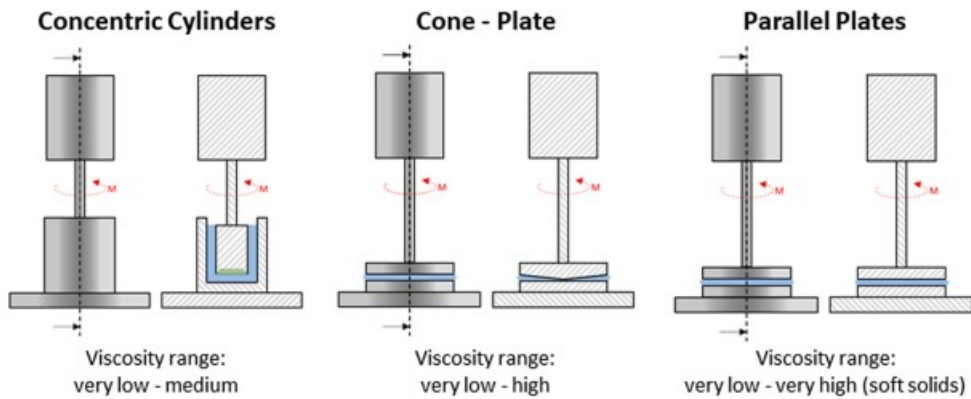


**Figure 2.2:** Different plates configurations for rheological properties tests.

Using a controlled stress rotational rheometer (DHR-2, TA Instruments, Waters, USA), two different tests were made: flow sweep test and three interval thixotropy test. The flow sweep test is useful for the characterization of the shear-thinning behaviour of the paste. Indeed, it is a rotational test, where an increasing shear rate is applied to the sample, measuring the corresponding viscosity. Instead, the three interval thixotropy test has the purpose to evaluate the velocity of the solid-like behaviour, after the extrusion, and the restored modulus. The first characterizes the ability to retain the nozzle shape, instead, the second has to be high to ensure a good shape fidelity. This test implies three consecutive steps, with different shear stress: a small shear stress, simulating the first rest region, a second step characterized by a stress near to the maximum one, like in the nozzle during the extrusion process, and the last one again with a small stress that simulates the behaviour of the paste after the deposition. These steps are repeated two times, in order to study the possibility of a time-dependency of the viscosity.

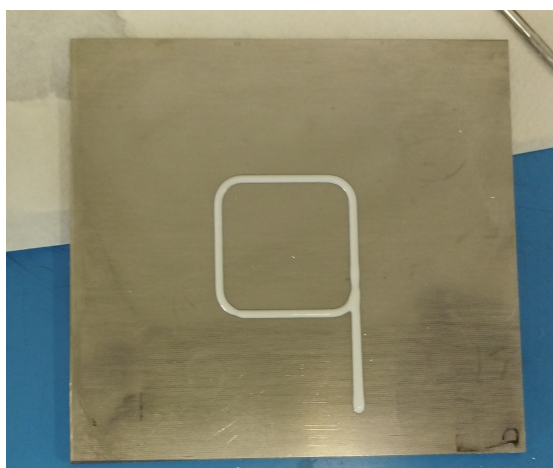


**Figure 2.3:** Printability test for the prepared pastes. The case here reported was about the GM31107 PG paste.

## 2.4 Joining fabrication

### 2.4.1 Sample preparation

Aiming to observe the thermochemical compatibility of the selected glass-ceramic systems with the metallic interconnector and the ceramic electrolyte, several samples were prepared and joined at high temperature. The samples have the following structure: FSS/Glass-ceramic/BCZY (figure. 2.4). Pieces of FSS (AISI441 or CroferAPU22) were cut, using a cutting machine, with dimension of 1.5x1.5 cm<sup>2</sup>. The glass-ceramic studied in this thesis have been deposited between the 1.5x1.5 cm<sup>2</sup> FSS pieces and equally sized pieces of BCZY (for the analyses performed, fragments of a half-cell with the composition  $BaCe_{0.7}Zr_{0.2}Y_{0.1}O_{3-\sigma}$ ). After forming the junction, it undergoes a drying phase by being placed in an oven at around 80-90°C for approximately 30 minutes. This step aims to remove the organic portion within the sealant. Subsequently, the sample undergoes a heat treatment to join the various components. The samples joined with V11 and V10, have been kept in the furnace for 1 hour at 850°C. The ones with GC2, have been treated at 950°C for 1 h; and finally. Finally, for the commercial glass, a thermal treatment at a temperature of 700°C for 30 minutes was used. For all these thermal cycles, a heating rate of 10°C/min is used to reach the desired temperature, followed by a cooling rate of 2°C/min down to 25°C.

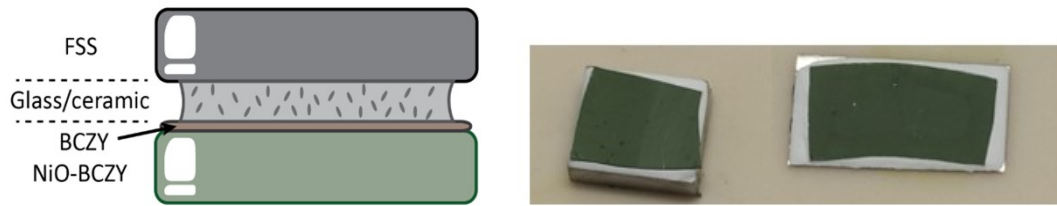


**Figure 2.4:** Schematic representation of a joining between a layer of FSS (dark grey), an half-cell (electrode green, and electrolyte brown), and a deposited layer of glass-ceramic sealant (light grey). On the right, there are two real joined samples, produced during this thesis work.

## 2.4.2 Ageing of samples

Different samples have been produced and characterized in relevant conditions. In this case, the samples previously joined (as described in the previous procedure) are placed within a humidified atmosphere (approximately 50% humidity) and subjected to an aging treatment, lasting about tot hours at a temperature of 600°C. Compared to a simple aging test, the introduction of humid air allows for the evaluation of potential material degradation due to contact with an atmosphere rich in water vapor, and simulate the real operation conditions. For assessments related to simple aging in a dry atmosphere, reference is made to earlier studies. The samples subjected to this treatment include:

- Crofer22APU/GM31107/ BCZY-1
- AISI441/V11/  $BCZY_1$
- AISI441/GM31107/ $BCZY_1$
- AISI441/GM31107+3YSZ (5%) / $BCZY_1$
- AISI441/GM31107+3YSZ (2.5%) / $BCZY_1$

At the end of the treatment, the samples are evaluated using SEM and XRD techniques to identify any potential degradation or generation of new phases. This investigation aims to provide insights into the performance of the joined materials in conditions closely resembling operational environments.



**Figure 2.5:** On the left there are all the samples prepared for the ageing test, with humid air (50%). On the right side, ageing test setup is shown.

## 2.5 Thermal analysis

### 2.5.1 Differential scanning calorimetry (DSC)

DSC is widely used thermal analysis techniques, applied across various fields and for different materials. For the present work, its application is related to characterizing the behaviour of glassy materials, allowing the study of property changes during glass transition, crystallization, melting, and other related phenomena. The following analyses specifically focus on these characteristic temperatures:  $T_g$  - glass transition temperature,  $T_x$  - crystallization temperature, and  $T_m$  - melting temperature. The ultimate objective of this analysis is to gather useful information for optimizing the thermal treatment employed during the joining process. There are two types of DSCs: heat flux DSC and power compensation DSC, and the difference between them is related to the measure technique, where the first the temperature difference among the sample and a reference, while, in the power compensation the measured difference regard the electric power used to maintain the samples and the reference at the same temperature [42][43]. The instrument used in the following experiments (DSC 404 F3 Pegasus, Netzsch, Germany) belongs to the former type, so further details on the latter will not be presented here and are instead referred to the relative literature [42]. The operational principle of a heat flux DSC is based on evaluating the heat flow exchanged between the sample and the environment. This evaluation can be conducted within a temperature range between  $-190$  and  $1900^\circ\text{C}$ , depending on the instrument used, and may involve the use of gases for studies conducted under specific atmospheres (nitrogen, argon, oxygen, or air). Inside the apparatus, two crucibles are present: one containing the sample for analysis and the other left empty, serving as a reference for result calibration. The calculation of the heat flow exchanged with the sample is obtained by comparing it

to the reference crucible, utilizing the difference in heat flow within the machine's chamber [42]. In detail, the apparatus is heated through internal resistors, and this heat flow reaches the two crucibles. At this point, the temperature difference  $\Delta T$  is assessed. In cases where phase transitions or other characteristic phenomena are occurring, the resulting signal due to thermal disequilibrium is generated and utilized to calculate the difference in thermal flow, following Fourier's law, where the subscripts S stand for sample, R for reference, and  $R_{th}$  represents the thermal resistance of the sensor.

$$\Phi = \Phi_S - \Phi_R = \frac{T_S - T_R}{R_{th}} = \frac{\Delta T}{R_{th}} \quad (2.1)$$

The operational parameters used for the analyses conducted in this study, were: 50 ml/min of air and 20 ml/min of argon, used as a protective gas. The final temperature reached was 1200 degrees Celsius, with a heating rate of 5°C/min.

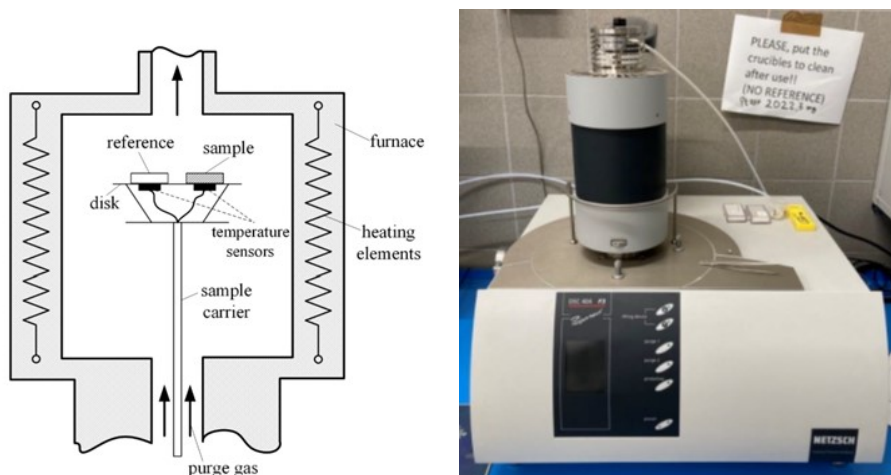


**Figure 2.6:** Left figure report a diagram of the DSC internal configuration [42]. On the right there is a photo of the DSC used for this work (DSC 404 F3 Pegasus, Netzsch, Germany)

### 2.5.2 Heating stage microscopy (HSM)

Heating Stage Microscopy (HSM) is an excellent method to observe thermal processes. This apparatus (EM301 Heating Microscope, Hesse Instrument, Germany) primarily consists of a light source, an electric furnace, and an observation unit, which allows for image acquisition and faithful reproduction on the control device. The measurement is carried out by placing a sample pellet on a substrate. The choice of the substrate material depends on the specific measurement. An alumina substrate is often used as a reference for various measurements. However,

it's possible to replace it with a substrate of a different material to observe the interaction between the sample and the specific substrate. Typical applications of this instrument involve assessing the thermal behaviour of a material, particularly identifying characteristic temperatures of shrinkage, softening, and melting. This is made possible by evaluating the silhouette evolution of the pellet, indicative of the occurrence of the processes [44]. Specifically, the characteristic temperatures identified by the instrument are as follows: a)  $T_{FS}$  - First Shrinkage or Sintering Temperature is when the glass begins to shrink, and necks form due to viscous flow ( $\eta = \text{viscosity}$ ;  $\log\eta = 9.1 \pm 0.1$ ). This step begins around 50°C to 70°C above the glass transition temperature  $T_g$ . b)  $T_{MS}$  - Temperature of Maximum Shrinkage occurs during powder densification before the glass starts to soften ( $\log\eta = 7.8 \pm 0.1$ ). c)  $T_D$  - Softening or Deformation Point is the temperature where the initial signs of softening manifest, evidenced by rounding of the sample corners ( $\log\eta = 6.3 \pm 0.1$ ). d)  $T_B$  - Sphere Temperature represents the point at which the sample's height equals its base width. e)  $T_{HB}$  - Half-Ball Point is where the sample's height is half its base width ( $\log\eta = 4.1 \pm 0.1$ ). f)  $T_F$  - Flow Temperature marks the point where the sample's height is less than a third of its base, and the sample is considered completely "molten" ( $\log\eta = 3.4 \pm 0.1$ ). Specifically, the temperatures  $T_{FS}$ ,  $T_{MS}$ , and  $T_D$  provide insight into the temperature range wherein the glass sintering process occurs and where the onset of crystallization can be detected. The latter observation is facilitated by comparing the graphs obtained through this instrument with those derived from DSC measurements. As for the thermal process employed, it remained consistent for all tested glasses and their respective substrates. It involves a heating rate of 60°C/min up to 300°C, followed by a rate of 5°C/min up to the maximum temperature of 1300°C. The measurements also include stopping criteria, allowing the test to be halted before reaching the maximum temperature.

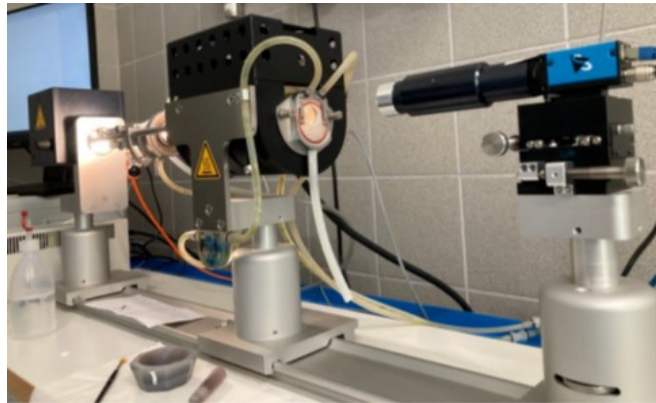


**Figure 2.7:** HSM instrument used for the measurements (EM301 Heating Microscope, Hesse Instrument, Germany)

### 2.5.3 Dilatometry (DIL)

A dilatometer is an instrument used to determine the volume changes of a sample with respect to temperature. More precisely, what is obtained is a deformation trend with temperature, and through the following formula, a coefficient known as the Coefficient of Thermal Expansion (CTE):

$$CTE = \frac{1}{L_0} \frac{\Delta L}{\Delta T} \quad (2.2)$$

Here,  $L_0$  represents the initial dimension of the sample, and  $\Delta L$  and  $\Delta T$  represent the changes in dimension and temperature, respectively. This measurement is conducted by inserting a cylindrical sample, obtained in this case by compacting the glass powder to be measured, with a size of approximately 5 mm (where size refers to the measurement direction  $L$ ), into the instrument. The sample is held in place by an alumina rod. In addition to CTE, this measurement also allows for the identification of characteristic glass transition temperature ( $T_g$ ) and softening temperature ( $T_s$ ) through the analysis of the obtained graph.

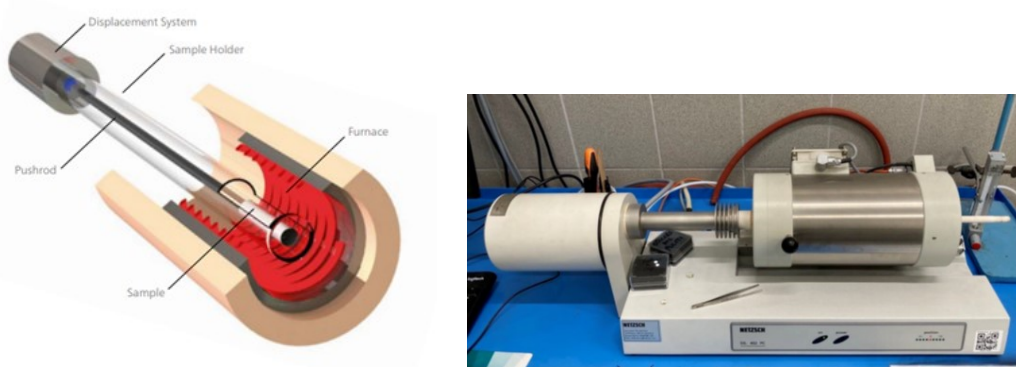


**Figure 2.8:** Left diagram represent the internal structure of a dilatometry instrument. On the right, is possible to see the dilatometry utilized for the work (DIL402PC, Netzsch, Germany)

## 2.6 Microstructural characterization

### 2.6.1 Scanning electron microscopy (SEM)

The scanning electron microscope (SEM) is an instrument that uses an electron beam to obtain microscopic-scale information about a specimen. The electron beam is generated from an electron gun, and then accelerated and focused using magnetic or electrostatic lenses. The sample is kept in high vacuum conditions to avoid

interaction between the electron beam and the atmosphere. Once the electrons reach the samples they can be elastically scattered away, with a large part of their energy intact, forming the backscattered electrons (BSEs), or their energy induce the emission of secondary electrons (SEs), X-rays or Auger electrons. All these electron signals are captured by using the proper detector. More in detail, BSE constitute a significant source of information about the specimen characteristics. Indeed, they provide information on specimen composition, topography, mass thickness, and crystallography[9][45]. SEs are created from an inelastic scattering of the beam and can provide information about the topography of the sample's surface. Another possible study that can be done regards the X-ray emitted from the atoms due to the interaction with the electron beam. These X-rays are characteristic of each atom species, and for that reason this principle is used to detect the presence of an element and its amount in a specific area of the sample, using an Emission Dispersive X-Ray spectroscopy (EDX).

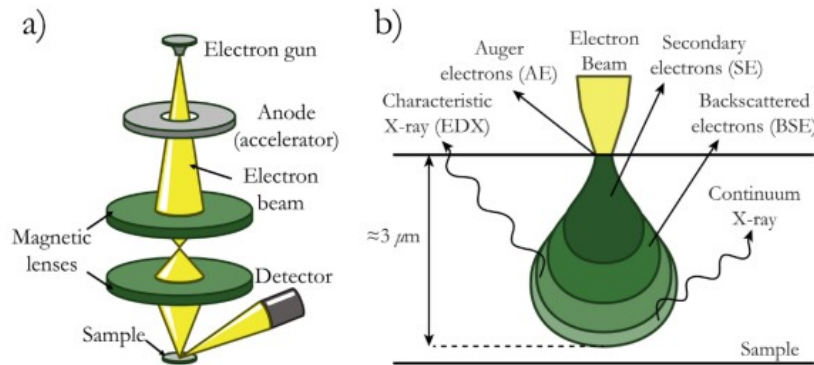


**Figure 2.9:** Representation of the operating principles of an SEM (a), and the type of signals produced during the interaction between electrons and the material (b)[9].

### Joined samples evaluation

Once the junction is obtained, it's prepared for subsequent examination under the SEM. This process involves encapsulating the junction within a cylindrical container, using a mixture of epoxy resin (Epofix) and a hardener, with a volume ratio of 8:1 for the resin. After allowing it to rest overnight, the encapsulated sample is extracted from the cylinder to undergo polishing using a polishing machine with SiC discs. It's important to evaluate the actual polishing of the sample before using optical microscopes. Next, silver paste traces are applied onto the sample for good conductivity during SEM testing. Finally, to further enhance sample conductivity, it's coated with nebulized platinum using a specialized machine (figure. 2.10).

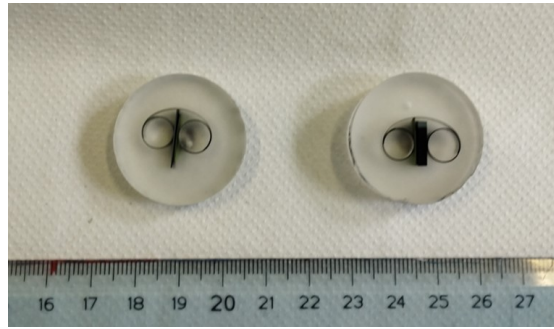


**Figure 2.10:** Two samples encapsulated in resin, ready for the SEM visualization.

### 2.6.2 X-ray diffraction (XRD)

X-ray Diffraction (XRD) analysis is a highly effective tool for examining the structure of materials and extracting vital information, including the study of crystalline phase formation within glassy materials. The operational principle involves the emission of X-rays in the form of coherent radiation with a fixed wavelength. These X-rays then strike the sample, leading to scattering phenomena in all directions, without undergoing any wavelength changes. This diffraction phenomenon follows Bragg's law:

$$2d\sin\theta = n\lambda \quad (2.3)$$

Here,  $\theta$  represents the angle of incidence,  $\lambda$  denotes the wavelength of the radiation,  $d$  stands for the distance between planes, and  $n$  corresponds to the order of reflection. The outcome of this analysis provides a diffraction distribution across an angle range from  $0$  to  $2\theta$ , offering insights into position and intensity. This, in turn, facilitates the identification of various structural characteristics[9].

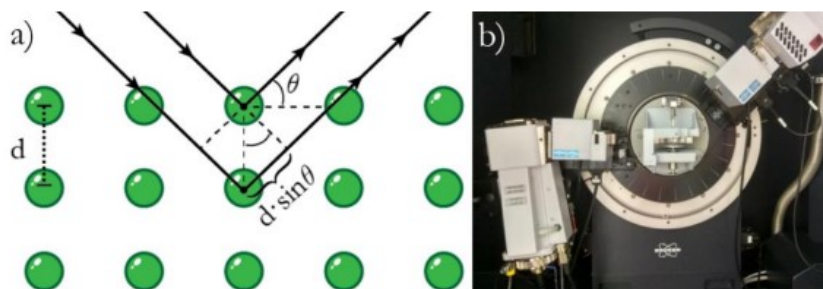


**Figure 2.11:** Representation of operating principles of an XRD test (a), and XRD instrument (b)[9].

# Chapter 3

## Results and discussion

### 3.1 Glass characterization

In this work four different glasses were studied. Two of them Ba-based (V10 and V11) and the other Na-based glasses (GC2 and GM31107). This allowed to compare different glass composition on thermal characteristics and behaviour under operative conditions, with a focus on interface between different components. Furthermore, other studies let to evaluate the possibility to modify the composition of the commercial glass, trying to meet the requests for this application.

#### 3.1.1 Evaluation of characteristic temperatures

The characteristic temperatures evaluation is carried out through DSC and HSM measurements. Figure. 3.1 shows the measurements obtained during the DSC analysis for all four glasses. It should be noted that the results for V10, V11 and GC2 were taken from previous works, and for differentiate them, dotted lines will be used in the graphs. One can notice that V10 and V11 shows a crystallization temperature peak in the range of 820-840°C. For GC2, a smaller crystallization peak is identified at an higher temperature, i.e. 910°C. In the case of GM31107, no peak associated to crystallization was found, indicating the preservation of its amorphous nature even at higher temperatures. Further evaluations about this behaviour will be done in following sections. DSC analyses allows to identify other important characteristic temperatures, as the transition temperature ( $T_g$ ) of the glass, which falls between 600-700°C for V10, V11, and GC2. Lower value instead for the GM31107, around 533°C. These results are particularly important, as the  $T_g$  is a crucial parameter for what concern the glass behaviour. For a glass seal, the  $T_g$  must be lower than the operational temperature [46][47]. The first three glasses, as mentioned, come from previous studies about SOC sealings. This is the reason

behind their high value of  $T_g$ , compared to the operational temperature considered for PCC. GM31107 instead, shows a value that falls within the desired ranges.

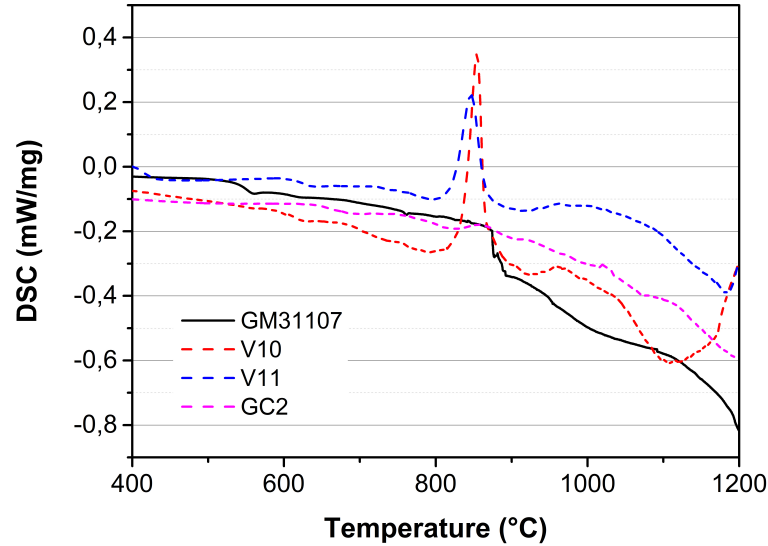


**Figure 3.1:** DSC analysis on GM31107, compared with results from previous works on V11, V10, and GC2.

By means of the HSM measurements, as shown in figure. 3.2, is possible deduce the temperatures related to the sintering range and the softening temperature. All the measurements considered below refer to the case with an alumina substrate. One can notice that the three silica-based glasses generally exhibit higher temperatures compared to the case of the commercial glass. This difference is also noticeable in terms of the presence of the crystallization plateau. Following the temperature of maximum shrinkage, the first three glasses display a flat zone, which is likely attributed to the crystallization process mentioned in the previous analyses. In the case of GM31107, no plateau was observed, in agreement with the DSC analysis made on the glass. Specifically, the crystallization phenomenon occurs between 700-900°C for V10 and V11, and between 750-920°C for GC2. After conducting the measurements to characterize the glasses, the assessment shifted to potential modifications arising from interactions with other components within the stack. Figure. 3.4 and figure. 3.3 illustrate the curves related to GC2 and GM31107 glasses, respectively, in both the alumina substrate case and when in contact with various types of BCZY ( $BCZY_1$ ,  $BCZY_2$ ,  $BCZY_3$ ), which compositions are reported in the previous chapter. In this instance, dashed lines indicate measurements taken on the alumina substrate. It is evident that there are no significant variations in the curve

shapes and characteristic temperature values, except for minor deviations. Among these, we highlight a reduction in temperature after the sintering temperature ( $T_s$ ) in the case of the commercial glass and slightly lower shrinkage values in the case of GC2 with the  $BCZY_1$  substrate. These variations warrant further analysis to confirm any actual trends or attribute these deviations to simple measurement errors.

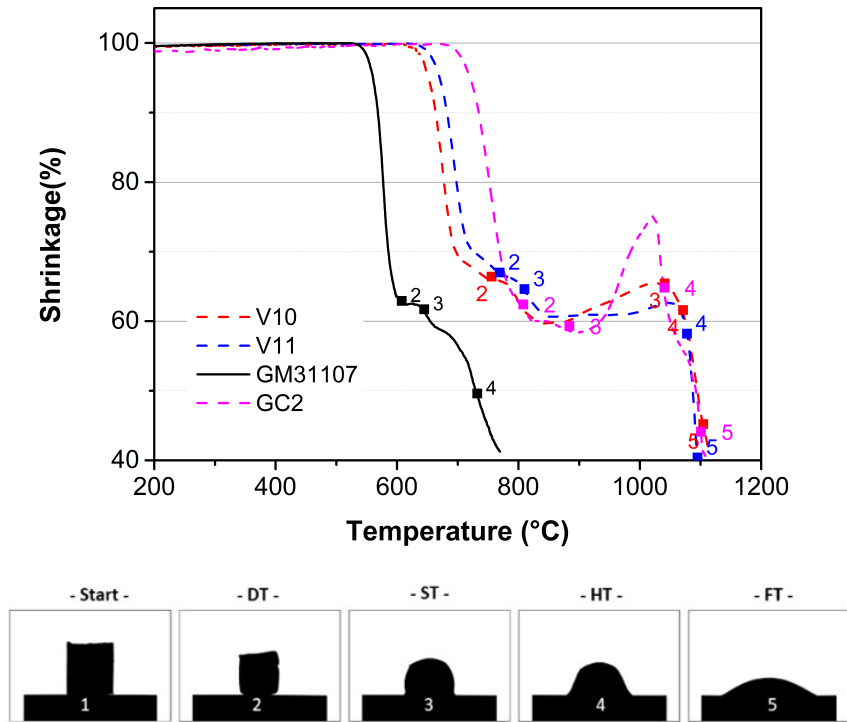


**Figure 3.2:** HSM measurements on GM31107, and data from previous works on V11, V10, and GC2. Characteristic temperatures are highlighted in the graphic with colored marker. The figures below explain the meaning of the numbers associated to the markers.

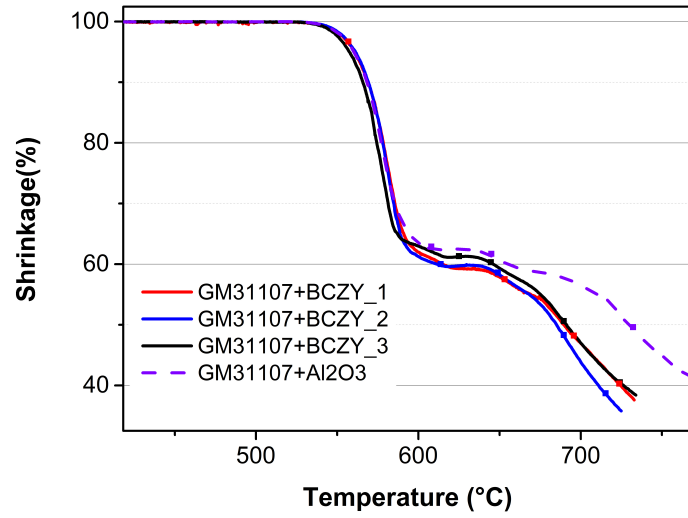


**Figure 3.3:** Curves relative to different HSM tests, made utilizing three typology of BCZY like substrate. The dashed line represent the values obtained in the case with  $Al_2O_3$

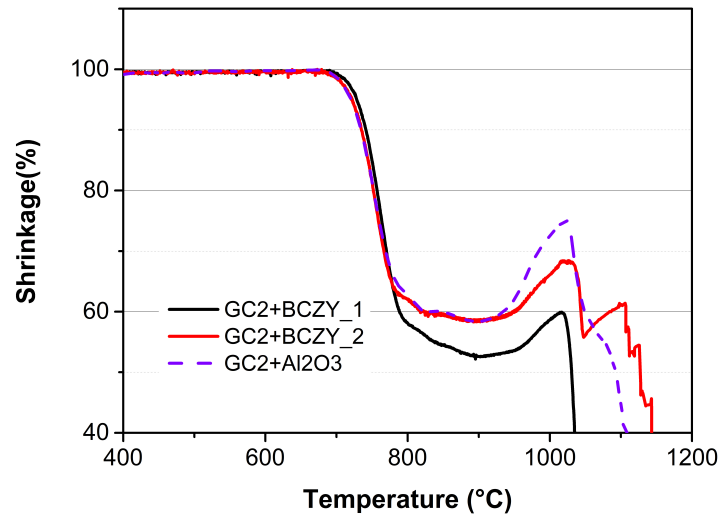


**Figure 3.4:** Curves relative to the measurements made by HSM, on GC2, considering different BCZY like substrate. The dashed line represent the values obtained in the case with  $Al_2O_3$

### 3.1.2 Coefficient of thermal expansion (CTE)

Another fundamental parameter for the thermal characterization of the different glasses is represented by the Coefficient of Thermal Expansion (CTE). In this case, a dilatometer was used as the tool to evaluate this coefficient. In figure. 3.5, we present the DIL measurements obtained. Similar to previous instances, measurements not conducted during this laboratory work are depicted with dashed lines. It's noticeable that for the commercial glass, the values lie within the range of  $11.2 - 12.7 * 10^{-6} K^{-1}$ . In this case, three different measurements were taken, with one exhibiting an error after  $500^{\circ}C$ , which is considered negligible as it does not significantly impact the CTE value. Considering the range of values covered by these results (averageCTE= $12.2E - 6K^{-1}$ , standard deviation = 0.7071) , it would be advisable to repeat these tests in the future to avoid potential measurement errors and narrow down the value within a more precise range. Among the three measurements about GM31107, figure.tot reports also the curve of GC2, taken from previous works, that shows a CTE value of  $10.88 * 10^{-6} K^{-1}$ . Recalling the information from preceding chapters, the CTE value should not deviate excessively from those of the materials that will interface within the stack junction. The following table tab.tot summarizes the measurement values, considering also V11 and V10, along with those associated with the junction materials. From these data, it can be observed that glasses V11 and GC2 exhibit values comparable to those of the other components, with a tolerance of  $\pm 1 * 10^{-6} K^{-1}$  in mind as a benchmark. A similar consideration applies to the commercial glass, but with an assumption that the actual CTE is in the range of  $11.2 - 12 * 10^{-6} K^{-1}$ , rather than trending towards higher values in the range. On the other hand, V10 presents a value lower than the acceptable limits for this application, which could potentially lead to consequences at the interface when joined with such materials.

Material	CTE ( $10^{-6} K^{-1}$ )
<b>GM31107</b>	$\approx 12.2$
<b>GC2</b>	$\approx 10.88$
<b>V11</b>	$\approx 10.59$
<b>V10</b>	$\approx 9.21$
<b>AISI441</b>	$\approx 11.5$
<b>Crofer22APU</b>	$\approx 11.2$
<b>BCZY</b>	$\approx 10-14$

**Table 3.1:** CTE of different materials

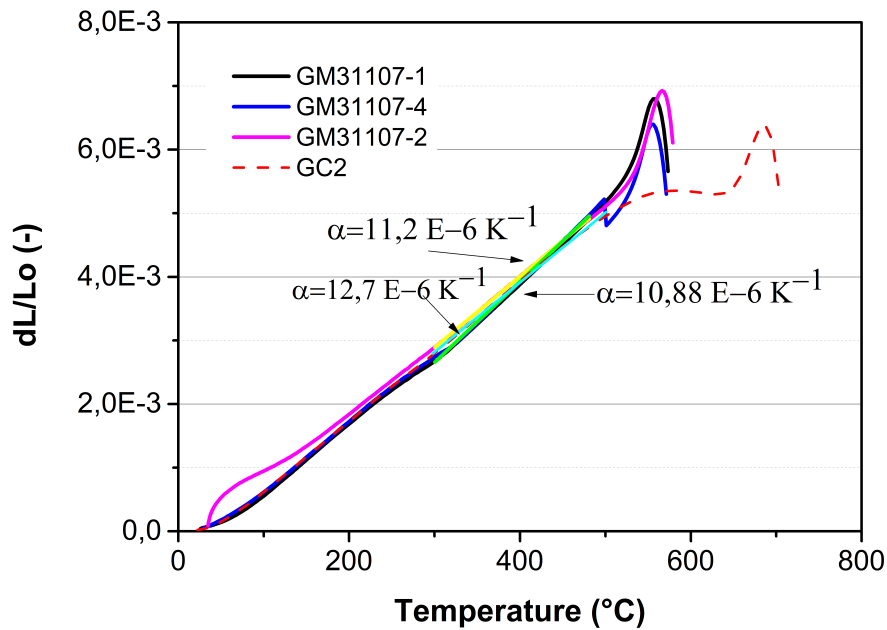


**Figure 3.5:** Curves relative to the dilatometry of GM31107 (three different measurements), and GC2, from previous works. CTE values obtained in the range 300-500°C are also reported.

## 3.2 Paste characterization

The rheological properties of the pastes produced during this work have been characterized and the results are here presented. Figure. 3.6 shows the flow sweep tests, made for the evaluation of the shear thinning behaviour, and three interval thixotropy test, that allow to study the recovery time of solid-like behaviour after the extrusion, were carried out. In this laboratory work, the two pastes composition were utilized, with GM31107 like solid load. Further comparison with GC2 and V11 were made for the shear thinning behaviour analysis, using data from previous works. In figure. 3.7 is possible to see the curves obtained during the flow sweep test. For both, the trends suggest a shear thinning demeanour, most highlighted for the terpeneol paste. Indeed, for the PG-paste is possible to notice an initial region where the paste shows a shear stress independent behaviour. Another interesting information is the high level of viscosity of the terpeneol paste, at the beginning of the test, right after the rest state, followed by a fast decrease. For what concern the old measurements on GC2 and V11, also them show a shear thinning behaviour, with intermediate values of initial viscosity respect the other. All the results are

considerable good, taking in consideration the advantages of using a shear thinning paste during the extrusion process[9]. Figure. 3.8 show the result for the three interval thixotropy test, considering only the PG-based paste with GM31107. The paste exhibit encouraging results in terms of velocity and dimension of the recovery. Also, in this case the paste shows a good behaviour, reaching a 73% of recovery after the first stress. For allowing a comparison among the pastes, fig.tot outline the test made on GC2 and V11 terpineol-based pastes. GC2 paste shows a higher initial viscosity, like already seen in the previous test, and also in this case a good recovery, even if lower that the commercial glass (63.6%). V11 present lower initial viscosity and a high recovery, around 70%.

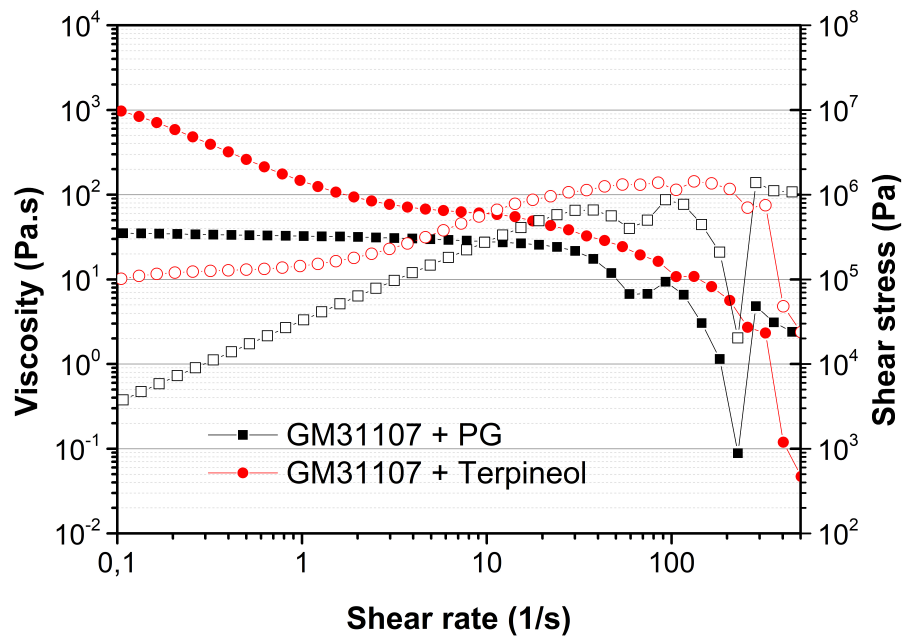


**Figure 3.6:** Flow curves of GM31107 in terpineol paste (red dots), and GM31107 in PG paste (black squares). Empty markers represent the shear stress.

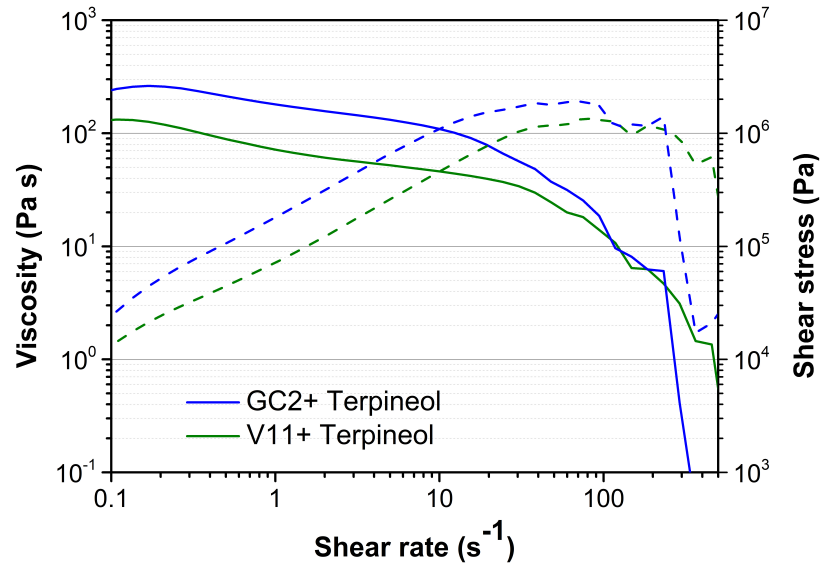


**Figure 3.7:** Flow curves of GC2(blu line) and V11(green line) terpeneol pastes. In this case lines are used to underling the fact that these results came from a preavious study [48]. Dashed lines represent the shear stress.

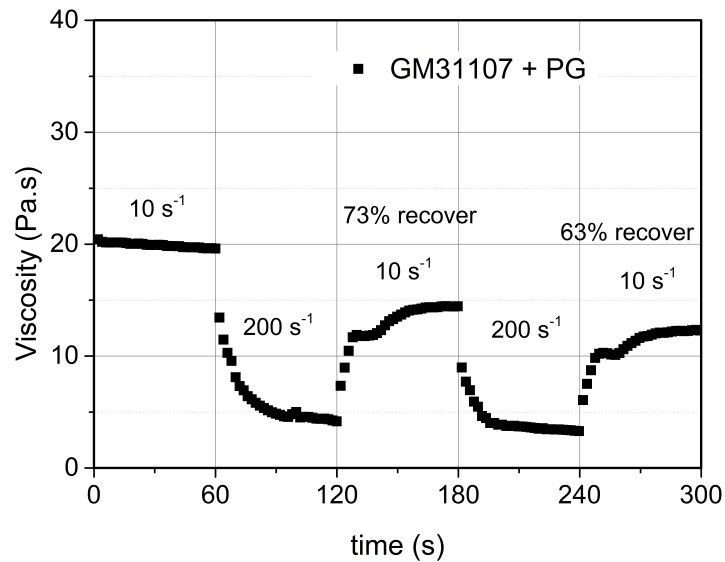


**Figure 3.8:** Three interval thixotropy test for GM31107+PG paste. In the figure are also reported the percentage values of recovery.

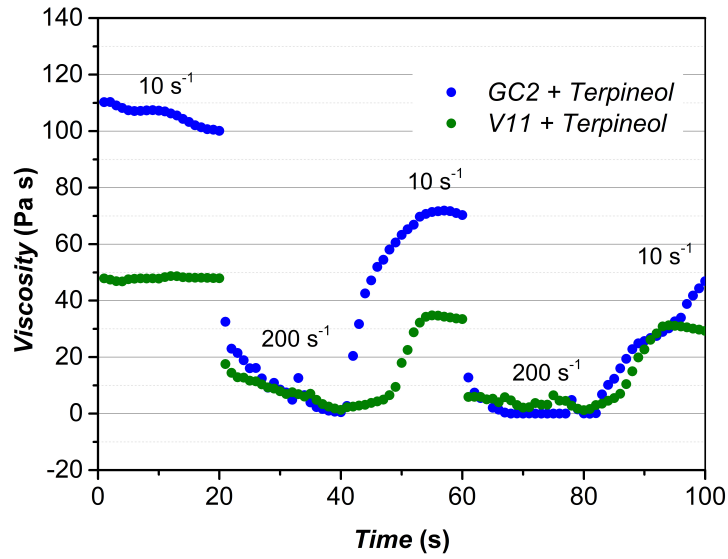


**Figure 3.9:** Three interval thixotropy test for GC2 (blue dots) and V11 (green dots) terpineol pastes. Also in this case the data utilized came from a previous study [48]

### 3.3 Microstructural characterization

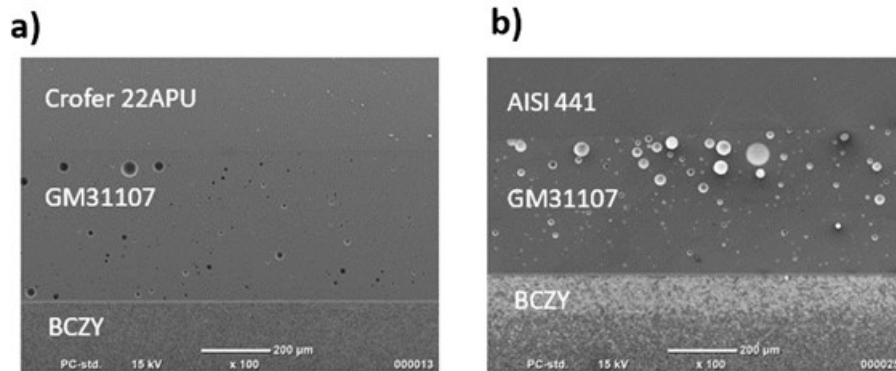
Once the thermal characterizations of the different glasses have been conducted, the focus shifts to studying their behaviour within a junction. Specifically, the compatibility of these glasses with the other two components they interface within a standard stack configuration is analysed (stainless steels and the electrolyte). As previously mentioned, for these applications, two different types of stainless steel have been chosen: AISI441 and Crofer22APU. As for the electrolyte, the choice is the one widely recognized in the literature as one of the best solutions for proton conduction,  $BCZY_1$ . In this specific case, it is part of a half-cell. The samples are first brought to the temperatures identified in the preceding sections before undergoing an aging process, which, in this instance, involves the use of a humidified atmosphere. To simplify the reading, the following nomenclature will be used in this section, for identify the samples (table. 3.2):

AISI441+GM31107+ $BCZY_1$ (pre-ageing)	S01
Crofer22APU+GM31107+ $BCZY_1$ (pre-ageing)	S02
AISI441+GM31107+ $BCZY_1$ (after-ageing)	S03
Crofer22APU+GM31107+ $BCZY_1$ (after-ageing)	S04
AISI441+V11+ $BCZY_1$ (after-ageing)	S05

**Table 3.2:** Samples nomenclature

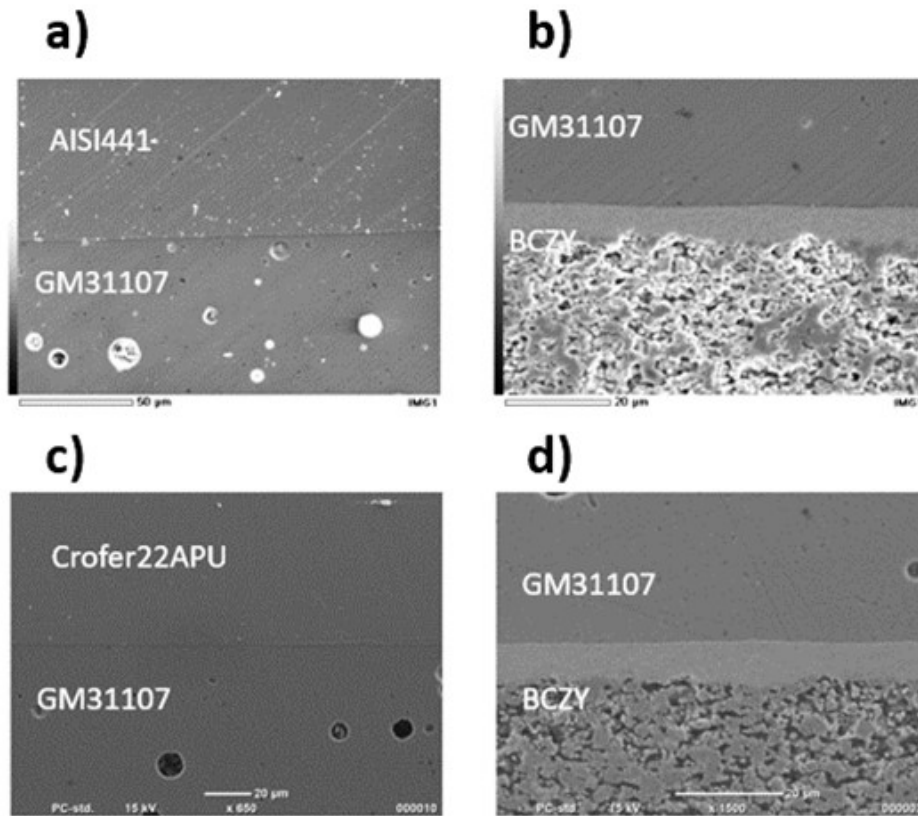
### 3.3.1 Joined samples

Figure. 3.10 shows the samples with the commercial glass (S01 and S02), which only did the joining treatment, with static air. More in detail, in figure. 3.10a there is the S01 sample, with commercial glass joined with Crofer22APU as FSS. Instead figure. 3.10b shows the sample S02, which is joined with AISI441. For both the configuration is possible to notice a good homogeneity inside the glass phase, with a limited number of pores. Also, at the interface the samples shows a good behaviour, without evident cracks or holes. In figure. 3.11 are reported



**Figure 3.10:** Two images of joined samples obtained through SEM: a) S02, and b) S01

different magnification, which better highlight the good compatibility between commercial glass, the two interconnectors and the electrolyte. Other important characteristic to notice in these SEM images is the complete absence of crystalline phase. This result confirms the ones previously obtained with HSM and DSC, which didn't show crystalline phase formation signs. To confirm the good results in



**Figure 3.11:** SEM images of the samples S01 and S02, with the magnification of the interfaces between the layers. For S01, a) shows the interface among the glass and the AISI441, while in b) there are glass and BCZY1. The images of the S02 are reported below, where in c) there is the interface with the Crofer22APU, and in d) with the BCZY1

terms of adhesion, present in figure. 3.11a,c, an EDX evaluation was made on the sample with the AISI441/GM31107/BCZY, to exclude possible Cr interdiffusion. Figure. 3.12 shows the distribution of the Cr at the interface between AISI441 and commercial glass, confirming the absence of interdiffusion. To accurately determine any reactions between the sealant glass and the BCZY electrolyte, an XRD of a mixture of powders from both was performed. In particular, it was observed that GM31107, when mixed with BCZY powder and heat-treated at 700°C for 30 minutes, does not react with BCZY to form new phases. Figure. 3.13 displays the XRD of the powder, comparing it with that of various BCZY samples, where no significant differences were detected.

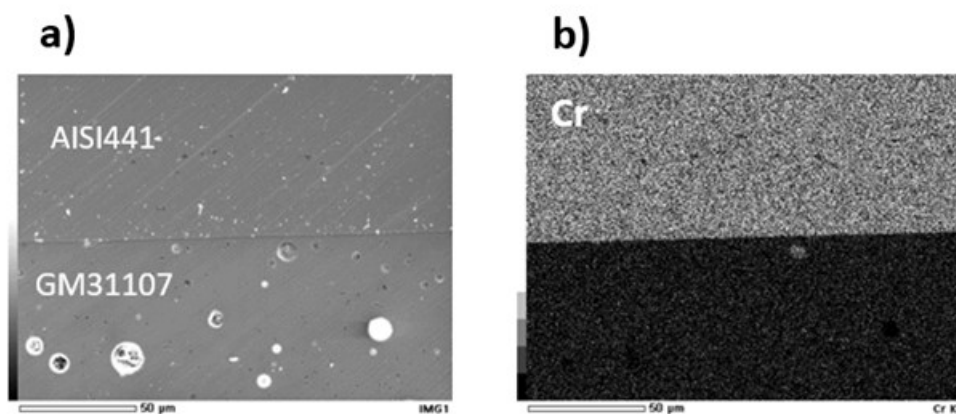


**Figure 3.12:** EDX of the interface between glass and AISI441, for the sample S01. The aim is to evaluate the possible interdiffusion of Cr in the glass phase.

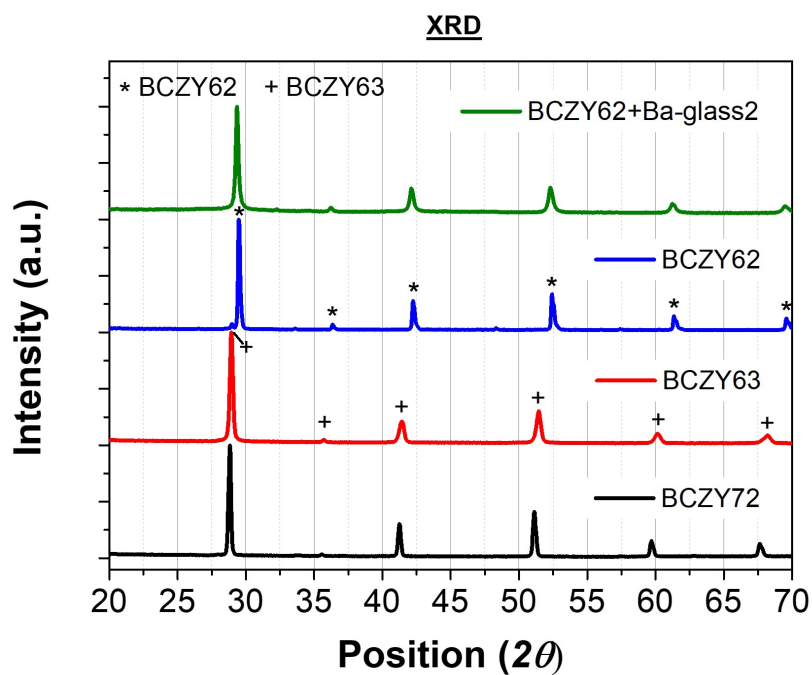
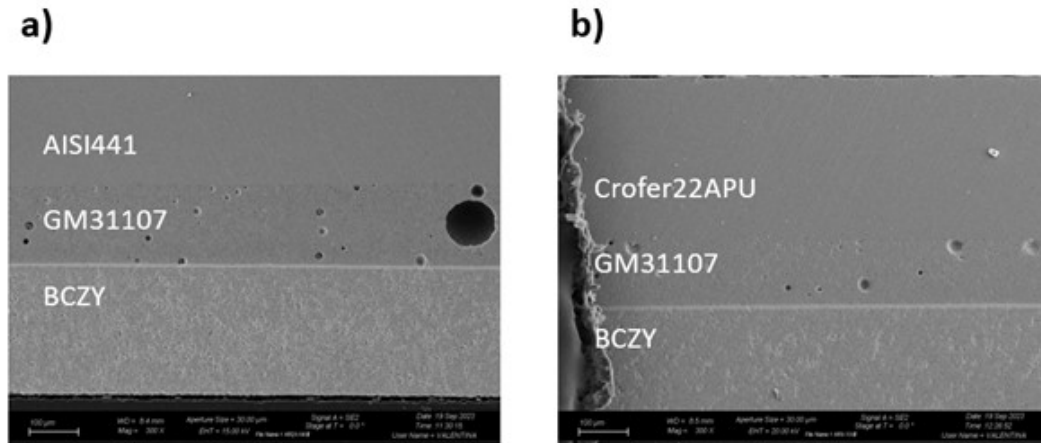


**Figure 3.13:** EDX of the interface between glass and AISI441, for the sample S01. The aim is to evaluate the possible interdiffusion of Cr in the glass phase.

### 3.3.2 After ageing

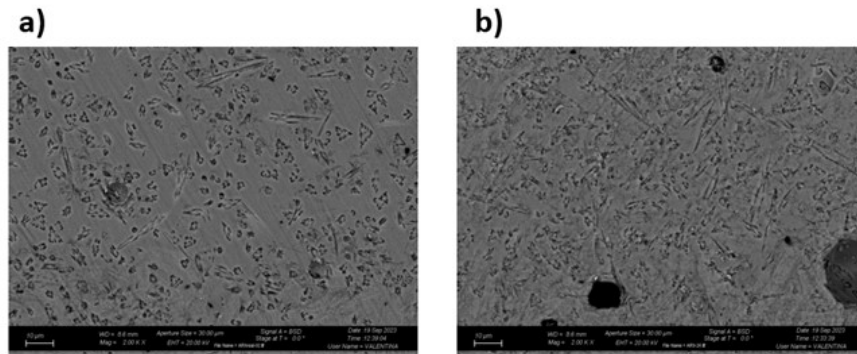
#### GM31107

Figure. 3.14 shows the samples S03, with commercial glass joined with AISI441 and  $BCZY_1$  (figure. 3.14a), and S04, with Crofer22APU as FSS(figure. 3.14b). Similar to the result obtained after the joining treatment, the glass doesn't show any cracks or imperfections at the interfaces or in the middle. The few holes present inside the glass phase may be due to the introduction of air in the deposition process.



**Figure 3.14:** Focus on the formation of crystalline phase inside the glass in the case of a) S03 and b) S04

Figure. 3.16 gives a magnification of the interfaces between the glass and the other two layers in both the cases. Important outcome from this test, for the commercial glass, is the formation of a crystalline phase. Different from the previous treatment, in static air at 700°C, in this one, with the humidified atmosphere at 600°C, seems to have an influence on reaction inside the glass phase. Figure. 3.15 exhibits magnification of the glassy phase, with the presence of an evident crystalline phase. These results need further investigation, to understand the causes behind this behaviour.



**Figure 3.15:** Focus on the formation of crystalline phase inside the glass in the case of a) S03 and b) S04

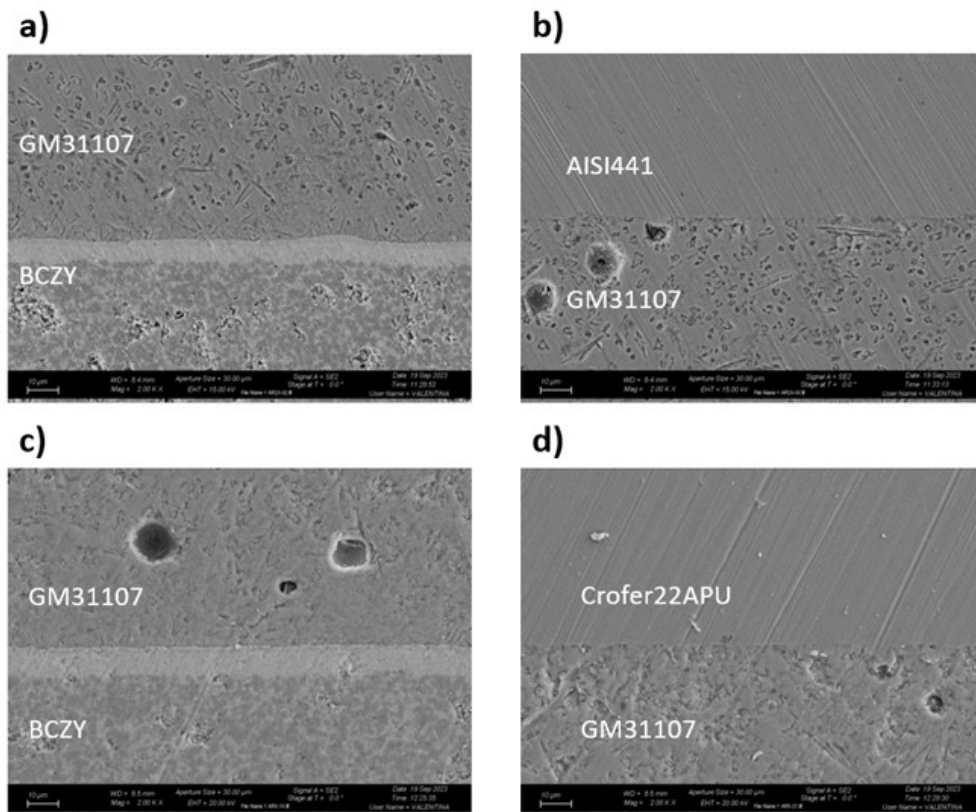


**Figure 3.16:** SEM images of the samples S03 and S04, with the magnification of the interfaces between the layers. For S03, a) show glass and  $BCZY_1$ , while b) shows the interface among the glass and the AISI441. The images of the S04 are reported below, where in c) there is the interface with the  $BCZY_1$ , and in d) with the Crofer22APU

## V11

Figure 3.17 shows the sample S05, constituted by the following layers: *AISI441* + *GM31107*+*BCZY*<sub>1</sub>. Once again, there is notable compatibility between these layers, despite an increased number of imperfections within the glass phase compared to other glasses. Along the interface, adhesion is generally good along most of its length, although certain regions exhibit significant pores or separation between the layers. A closer look at these interfaces can be seen in Figure 3.18a, b. Regarding V11, previous research focused on its behaviour post-joining treatment and aging in a static air environment[48]. In that investigation, no significant imperfections were observed either within the glass or at the interfaces with other components. However, after 1000 hours of aging in static air, there was evidence of Cr interdiffusion within the glass[9], a phenomenon distinct from aging in humidified air, where no new interdiffusion layers were detected.

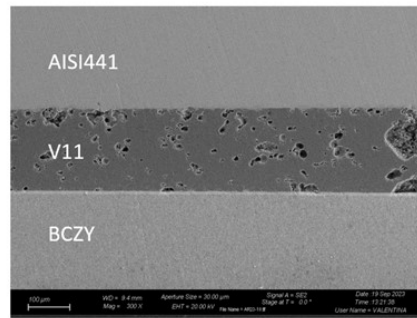


**Figure 3.17:** SEM images of the joined samples S05, with V11, *BCZY*<sub>1</sub> and *AISI441*.

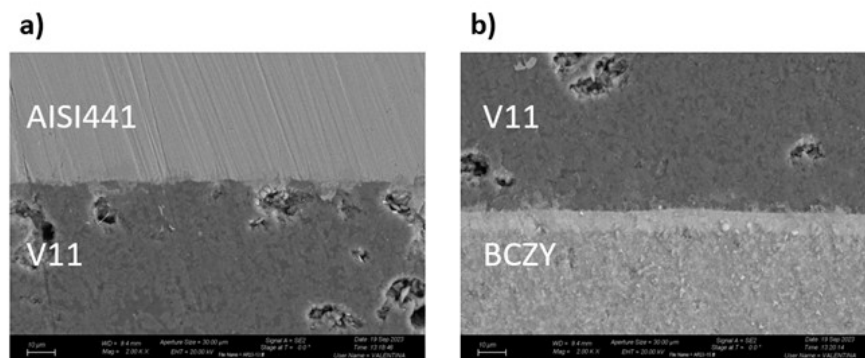
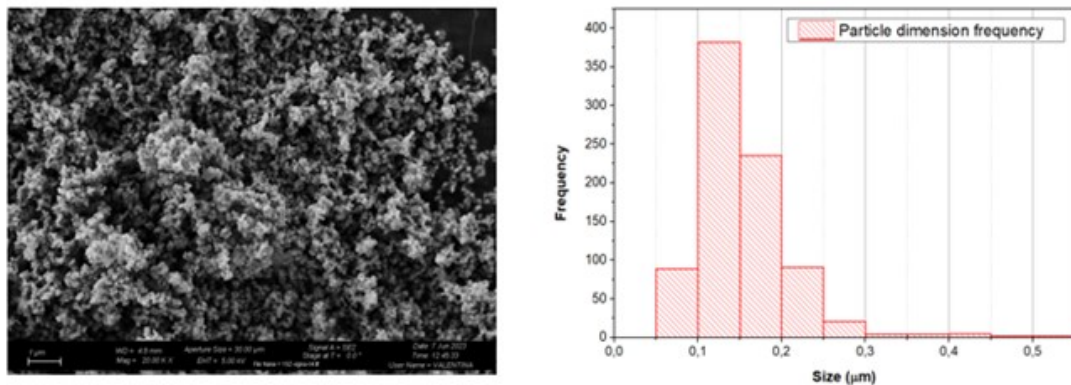


**Figure 3.18:** Magnification of the interface between V11 and a) *AISI441*, and b) *BCZY*<sub>1</sub>

## 3.4 Modification of glass composition

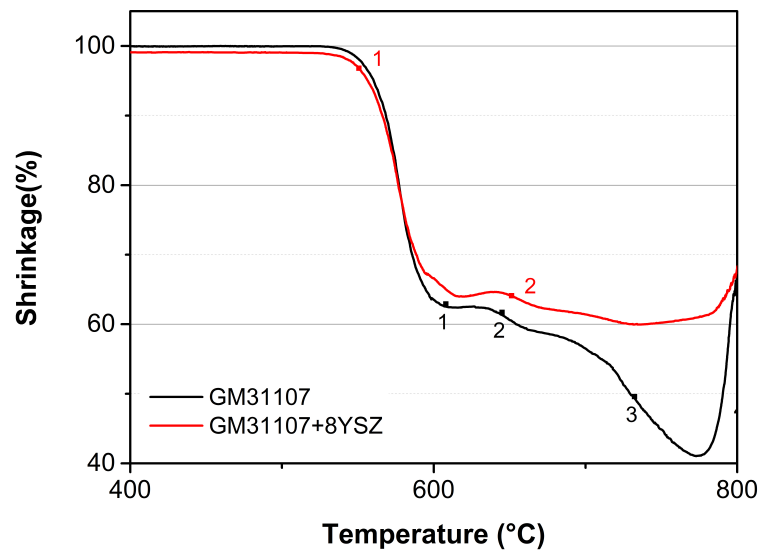
### 3.4.1 GM31107+8YSZ

Figure. 3.19 report the average size of the particles of 8YSZ, and an image of the powder taken from the SEM. The average value was  $0.15353\mu m$  in the 8YSZ case. Following is reported a comparison between HSM curves about pure GM31107 and



**Figure 3.19:** On the left there is a magnification of a 8YSZ powder, which was utilized for the evaluation of particles size. On the right there is a size distribution of the particles.

mixed with 8YSZ (figure. 3.20). Is possible to notice that the difference among the two behaviours is negligible. For this evaluation, powder pellets were used. Figure. 3.21 report the three HSM measurements made on modified glass, where Comp-01 and Comp-02 represents the samples made of a paste droplet, while Comp-03 is the previous mentioned powder pellet sample.



**Figure 3.20:** Comparison of HSM results between pure GM31107 and modified one, with the adding of 8YSZ (5%wt).

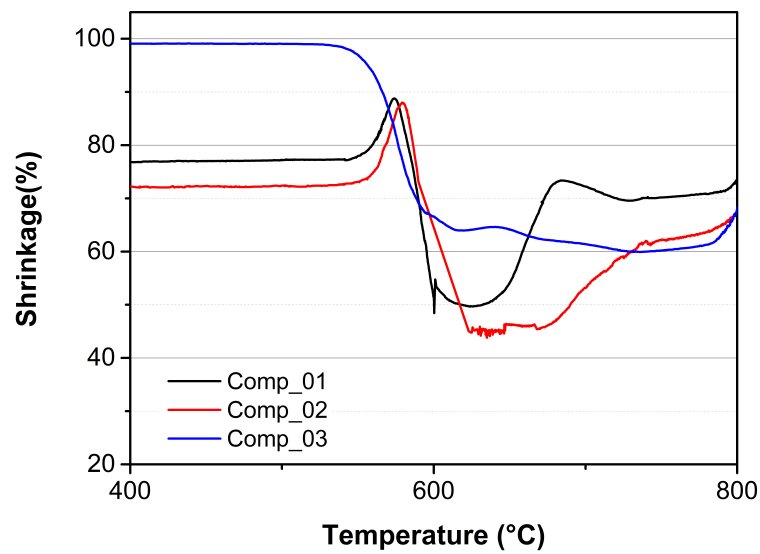


**Figure 3.21:** All the results obtained during the HSM tests on GM31107+8YSZ(5%). Comp-1 and Comp-2 were made from a paste droplet, while comp-3 was a normal HSM test on a powder pellet. Under the chart are reported the samples after the HSM tests.

From the SEM micrographs showed in Figure. 3.22, is possible to notice that the glass appears cracked after the joining process. These cracks are present on the whole surface and in the interfaces with other components. Possible reason to this result could be the marked differences between the CTE ( $10.5 * 10^{-6} K^{-1}$  for the 8YSZ, and  $12.2 * 10^{-6} K^{-1}$  for GM31107), or the small size of the particles. One can observe the good dispersion of the 8YSZ particles inside the glass matrix. This result was obtained using PVP as dispersant in the PG solvent.

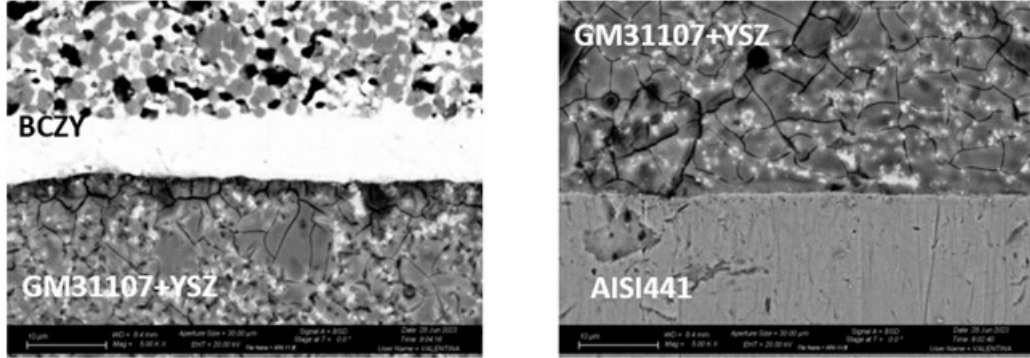


**Figure 3.22:** SEM images of joined samples, containing glass-ceramic sealant (GM31107+8YSZ).

### 3.4.2 GM31107+3YSZ

Due to the problems obtained with the addition of 8YSZ inside the commercial glass, another try was made using a different type of YSZ. In this case 3YSZ was mixed with the glass. Differently from the previous modification, this time YSZ is characterized by a 3% of yttria, and a particle size higher than the 8YSZ. The following test were made trying to reproduce the operational condition of the cell, so with a humidified atmosphere. Figure. 3.23a,b reports the SEM images of the sample with the addition of 2.5%w.t. of 3YSZ, while figure. 3.23c,d shows the sample with 5%w.t. of 3YSZ. It is noteworthy that, instead of observing cracks and defects within the glass, both samples exhibit a crystalline phase in this case, as shown in figure. 3.24. Additionally, the compatibility of the glass at the interfaces remains satisfactory. Further analyses are required to comprehend the distinct behaviours of these two YSZ types and to assess the potential enhancements that this addition could introduce to the thermal and rheological properties of the glass.

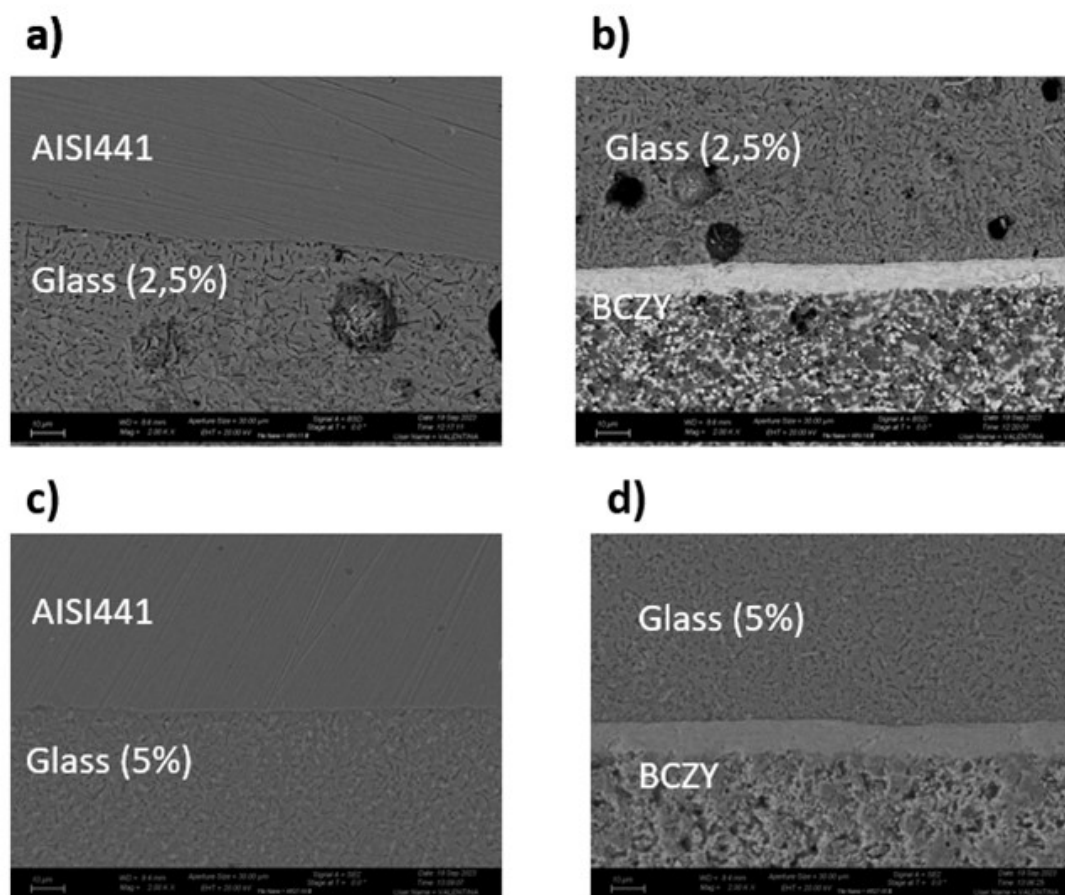


**Figure 3.23:** SEM images of the samples with modified GM31107. First two are related to GM31107+3YSZ (2,5%), where a) show glass and AISI411, while b) shows the interface among the glass and the  $BCZY_1$ . The remaining images are about GM31107+3YSZ (5%), where in c) there is the interface with the AISI441, and in d) with the  $BCZY_1$ .

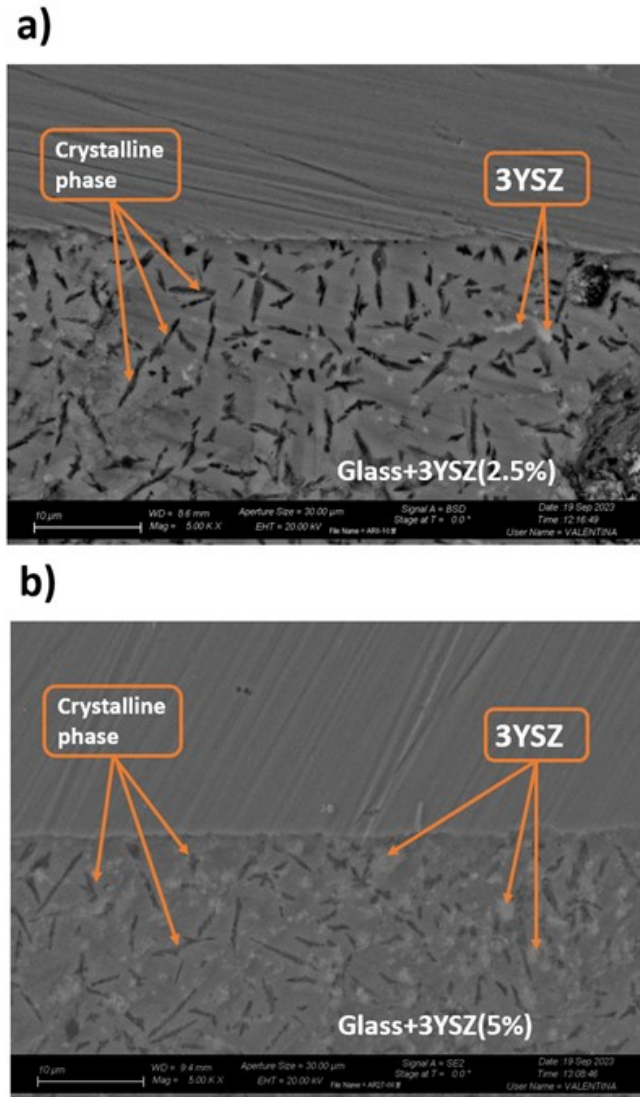


**Figure 3.24:** SEM magnifications of the glass phase: a) *AISI441 + GM31107(+2.5%wt3YSZ)+BCZY<sub>1</sub>* and b) *AISI441+GM31107(+5%wt3YSZ)+BCZY<sub>1</sub>*.

# Chapter 4

## Numerical modelling

The following chapter delineates the modelling of a single PCEC. Given the need to develop a comprehensive model for a PCC stack (for both the fuel cell and electrolysis configurations), here is presented the initial step toward achieving this objective. To obtain necessary data for optimizing the design of an entire stack, it is imperative to deeply characterize and investigate the thermo-electric behavior of a single cell. For this purpose, a 2D computational fluid dynamics model for a PCEC is proposed, which takes in account the governing equations of mass and momentum transport, charge, and species conservation, and energy transfer in a two-dimensional domain.

### 4.1 Model development

For the development of this simulation model, different mathematical models from the literature, developed for SOFC, SOEC, and PCFC were used, because of the similitude of these systems. For what concern the parameters that are necessary during the simulation, they were taken from literature, and other works [48]. The model has been developed using COMSOL Multiphysics software.

#### 4.1.1 Charge balance

PCEC technologies include materials with electric conduction, ionic conduction, or both, in the case of the electrodes. The transport of these charges is described by the Ohm's law equation. 4.1, expressed as:

$$-\nabla(\sigma_i \nabla V_i) = S_{i,a,c} \quad (4.1)$$

Where  $\sigma_i$  represent the ionic or electronic conductivity.  $V_i$  is the electric potential, and  $S_i$  is the charge source term. This equation (equation. 4.1) must be applied ion

both the electrodes and the electrolyte. For this simulation, the ion conductivity of the electrolyte was considered fixed, and equal to  $1.4 * 10^{-2} S/cm$  [49][50], while the ionic conductivity of the active part of the electrodes, was taken equal for anode and cathode, following this equation (equation. 4.2):

$$\sigma_{GDE} = \sigma_{elect} f_l \quad (4.2)$$

Where  $\sigma_{elect}$  is the conductivity of the electrolyte,  $f_l$  is a correction factor, which consider the volume of ionic conductor inside the active volume of the electrode (GDE). In this case is considered equal to 0.2 [48]. For what concern the electronic conductivity of the electrodes, it is equal to  $10^5 S/m$  [48]. The parameter  $S_i$  (equation. 4.1), is defined by the equation (equation. 4.3):

$$S_{i,a,c} = \pm A_{TPB} j_{a,c} \quad (4.3)$$

Where  $A_{TPB}$  is the specific surface area of the TPB, taken equal to  $1 * 10^9 1/m$  in this case, which is considered uniformly distributed in the GDE layer of the electrodes.

### 4.1.2 Mass balance

Transportation phenomena are mainly driven by diffusion and convection in the porous electrodes of the cell and in the gas channel equation (equation. 4.4):

$$\frac{\partial}{\partial t}(\rho\omega_i) + \nabla(\rho\omega_i u) = -\nabla J_i + R_i \quad (4.4)$$

where, considering the mixture of N species (with i that goes from 1 to N),  $\rho$  is the density, u the mass average velocity,  $\omega_i$  the mass fraction,  $J_i$  the diffusion flux, and  $R_i$  the rate of consumption or production of a species i [51]. The diffusion flux of chemical species  $J_i$  is written as below (equation. 4.5):

$$J_i = -\rho\omega_i \sum_k D_{i,k,eff} (\nabla\chi_k + \frac{1}{p}[(\chi_k - \omega_k)\nabla p]) \quad (4.5)$$

Where  $D_{i,k,eff}$  is the effective diffusivity and  $\chi_k$  is the molar fraction of the k specie [51]. Assuming the porous electrode to be composed by a solid phase made of spheres and the bed phase surrounding the spheres treated as the void fraction of the electrode, the Buggerman's equation can be used for the calculation of the effective diffusivity (equation. 4.6):

$$D_{i,k,eff} = \epsilon^{1.5} D_{ik} \quad (4.6)$$

Where  $\epsilon$  represent the porosity of the electrodes, that in this case is set as 0.4 [48][49].

### 4.1.3 Heat balance

Temperature is a fundamental parameter for this simulation, due to the dependence of different parameters to its value. In this case, considering the operational temperature, around 600°C, radiative heat transfer could be neglected. So, the only heat transfer phenomena are convection and conduction. Conductive heat transfer (equation. 4.7) can be expressed as:

$$\rho C_{p,eff} u \nabla T = \nabla(k_{eff} \nabla T) + Q_{gen} \quad (4.7)$$

Where  $\rho$  is the density,  $cp$  the specific heat capacity and  $k_{eff}$  the conductivity. This equation is applied to all the domains, (solid, gas and porous), so they depend on the domain considered. For porous materials, these three parameters are weighted for the solid and fluid component, obtaining effective parameters.  $Q_{gen}$  is the heat source term, that varies depending on the part of the cell considered. the thermal conductivity term can be written as follow (equation. 4.8):

$$k_{eff} = \epsilon_p k_f + (1 - \epsilon_p) k_s \quad (4.8)$$

Where  $k_f$  and  $k_s$  represent the thermal conductivity of the gas and solid phase respectively. Convection heat transfer is related to the flow of the species and can be expressed like follow (equation. 4.9):

$$(\rho c_p) \frac{\partial T_f}{\partial t} = -\nabla(k_f \nabla T_f) - (\rho c_p)_f u \nabla T_f \quad (4.9)$$

Where  $T_f$  is the temperature of the fluid,  $k_f$  its thermal conductivity, and  $u$  the velocity field vector. In the present application, the heat sources evaluated are the electrochemical reaction irreversibilities (equation. 4.10), and the Joule's effect in electrodes and electrolyte (equation. 4.11). No heat sources are considered in the gas channel.

$$Q_{chem} = -\Delta S_e \frac{T J a_v}{n_e F} \quad (4.10)$$

$$Q_{ohm} = \frac{J^2}{\sigma} \quad (4.11)$$

Where, in the equation. 4.11, the  $\sigma$  is the electrolyte ionic conductivity or electrode electronic conductivity, depending by the case, while in equation. 4.10,  $\Delta S_e$  is the change in entropy of the reaction [52].

### 4.1.4 Electrochemical reaction

The potential of the cell was described previously described, in the introduction chapter, by the following equation (equation. 1.6). In that equation, different over-potential are added, accounting for the polarization phenomena, to  $V_{oc}$ , that is the

open circuit voltage. The charge transfer kinetics is expressed by the Butler-Volmer equation (eq.x), that here is reported for the anode (equation. 4.12) and for the cathode (equation. 4.13):

$$i_a = i_{0,a} \left[ \exp\left(\frac{\alpha_{b,a} F \eta_{act,a}}{RT}\right) - \exp\left(\frac{-\alpha_{f,a} F \eta_{act,a}}{RT}\right) \right] \quad (4.12)$$

$$i_c = i_{0,c} \left[ \exp\left(\frac{\alpha_{b,c} F \eta_{act,c}}{RT}\right) - \exp\left(\frac{-\alpha_{f,c} F \eta_{act,c}}{RT}\right) \right] \quad (4.13)$$

Where  $i_{0,a}$  and  $i_{0,c}$  are the exchange current densities for anode and cathode respectively, alphas are the backward and forward transfer coefficients [48]. For this simulation, the value of exchange current densities was calculated starting from the physics given by COMSOL software, here reported (equation. 4.14, 4.15):

$$i_{0,a} = i_{0,a,ref} \prod_{i:v_i>0} \frac{p_i^{\frac{\alpha_c v_i}{n}}}{p_{i,ref}} \prod_{i:v_i<0} \frac{p_i^{\frac{-\alpha_a v_i}{n}}}{p_{i,ref}} \quad (4.14)$$

$$i_{0,c} = i_{0,c,ref} \prod_{i:v_i>0} \frac{p_i^{\frac{\alpha_c v_i}{n}}}{p_{i,ref}} \prod_{i:v_i<0} \frac{p_i^{\frac{-\alpha_a v_i}{n}}}{p_{i,ref}} \quad (4.15)$$

Where  $i_{0,a,ref}$  and  $i_{0,c,ref}$  are the references value for anode and cathode respectively. In this case the value for both was taken equal to  $1.00 A/cm^2$ .

## 4.2 Geometry

The design employs a 2D rectangular anode-supported PCC, as detailed in a prior study [48], featuring an area equivalent to that of a circular geometry with a 3 cm radius. The materials considered are BCZY for the electrolyte, NiO-BCZY as fuel electrode, and BCZY-BGLC for the air electrode. The model is composed, starting from the top, by fuel flow channel, fuel electrode gas diffusion electrode layer (GDL), active volume of the fuel electrode (GDE), membrane, active volume of air electrode (GDE), air electrode gas diffusion electrode layer (GDL), and air flow channel (figure. 4.1). The flow channels represent the channels of the interconnector. The electrodes were divided into two volumes: a gas diffusion layer, where the reaction doesn't take place, and an active volume, where reaction takes place (figure. 4.2). Geometry parameters were taken from [48] and are here reported in tab. 4.1.

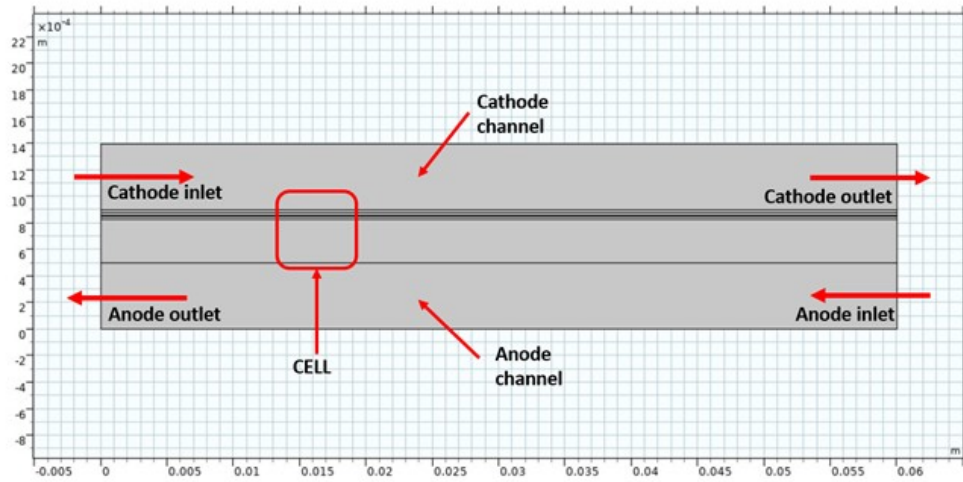


Figure 4.1: Geomtry of the model from COMSOL software.

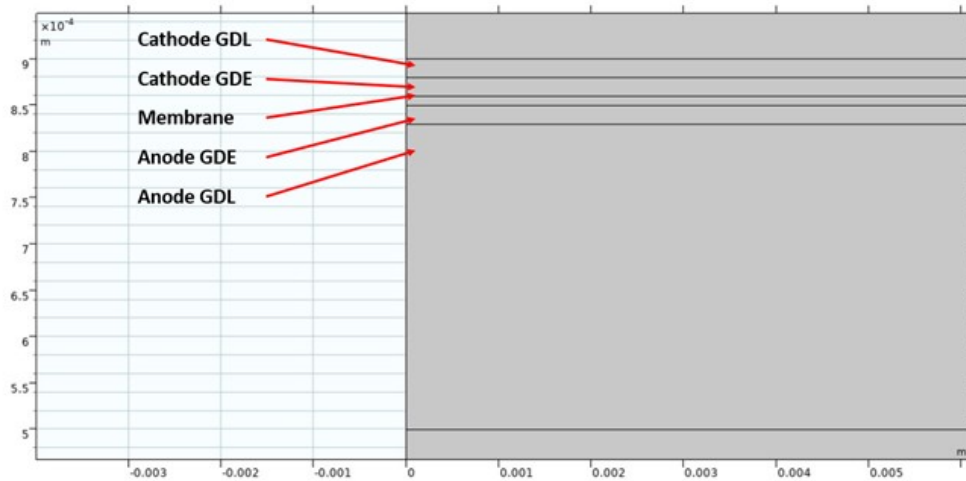


Figure 4.2: Magnification of the cell, from the model geometry

## 4.3 Simulation results

### 4.3.1 Boundary conditions

Boundary conditions and cell parameters have been calibrated using data from previous work [48], with the necessary modification due to the change in configuration, from fuel cell to electrolysis mode. In this case, a mixture of steam and oxygen is introduced at the anode with a molar fraction of water vapor of 0.97, assuming steam recirculation with oxygen separation (i.e. not complete separation as it is

Length	6cm
Air and fuel flow channels thickness	500 $\mu$ m
Fuel GDL thickness	20 $\mu$ m
Fuel GDE thickness	20 $\mu$ m
Electrolyte thickness	10 $\mu$ m
Air GDE thickness	20 $\mu$ m
Air GDL thickness	330 $\mu$ m

**Table 4.1:** Geometry parameters of the PCEC

not necessary) on the anodic side. Hydrogen is considered slightly humidified, with a molar fraction of water vapor of 0.1. The operating temperature considered for the simulation is 600°C, imposing it as inlet temperature of the fluids. For what concern the potential of the cell, ground potential is fixed to the anode, and the cell voltage is imposed at the cathode, starting with a value of 0.98 V (OCV). For the calculation of i-V polarization curve and power density curve, the Vcell was varied within a range of 0.98V to 1.2V. No flux condition was imposed for all the boundaries of the cell, except for inlet and outlet section, where a mass flow rate and atmospheric pressure were imposed respectively. Considering the thermal model, thermal symmetry was applied to the upper and lower boundary, while a thermal insulation was applied for the side boundaries of the cell.

### 4.3.2 Electrochemical behaviour curves

The simulation was conducted for an electrolysis setup, where hydrogen flowed at the cathode with a mole fraction of water equal to 0.1, while oxygen flowed at the anode with a mole fraction of water equal to 0.97. Figure. 4.3 displays the i-V polarization curve obtained from the simulation. The Open Circuit Voltage (OCV) is registered at 0.98 V, with subsequent current densities showing negative values. This outcome can be attributed to the specific electrolysis mode chosen for this scenario. In figure. 4.4, power density vs current density graph is reported. In this case also, the value of current and power are negative, for the reason previous mentioned. The peak of power density is obtained for a current density of 2.03A/cm<sup>2</sup> and is 3.25W/cm<sup>2</sup>.

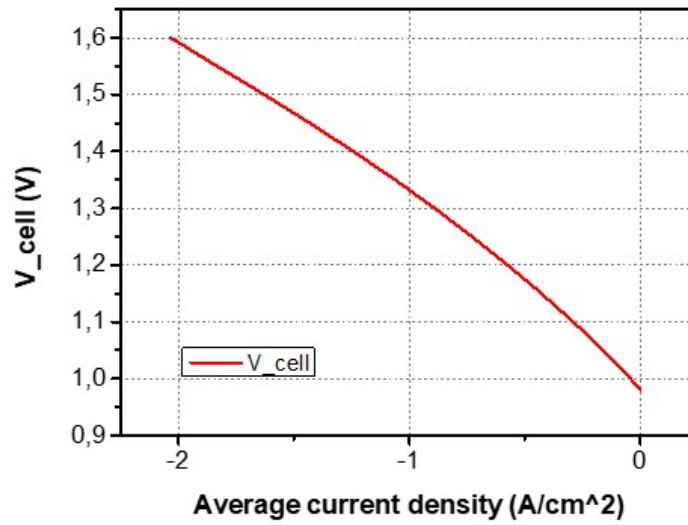


**Figure 4.3:** Polarization curve  $i$ - $V$ , from the COMSOL model of a PCEC.

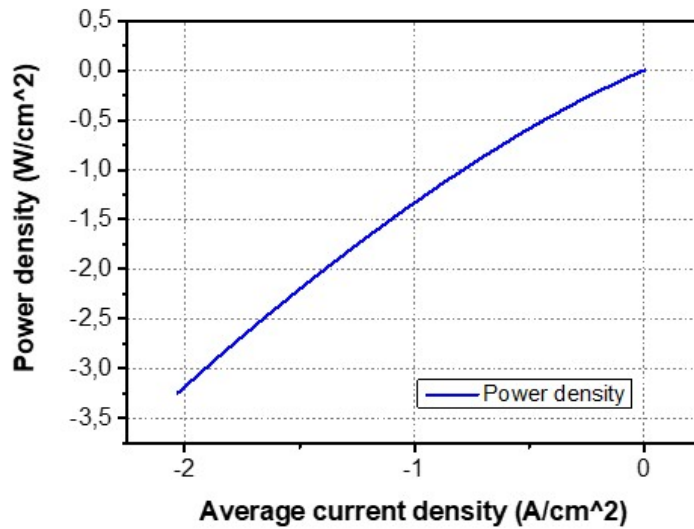


**Figure 4.4:** Power density vs Current density curve, from COMSOL model of a PCEC.

### 4.3.3 Species mole fraction

The model was also utilized to highlight the distribution of species mole fraction. Figure. 4.5 shows the distribution of  $H_2$ ,  $O_2$ , and  $H_2O$  mole fraction for a cell

voltage equal to  $1.6V$ , and a current density of  $2.03A/cm^2$ . It is possible to notice the formation of hydrogen along the cathode side, and the respectively consumption of water at the anode.

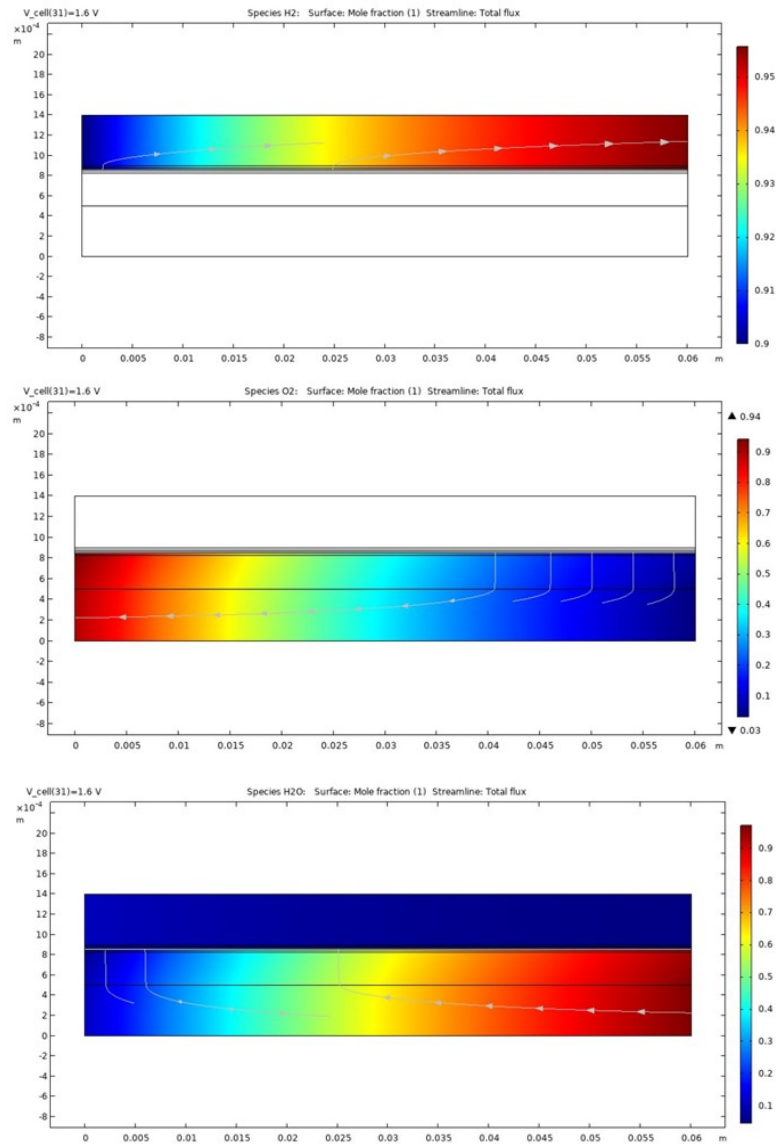


**Figure 4.5:** Molar fraction results, for a voltage equal to  $1.6V$ , from COMSOL software. a)  $H_2$  molar fraction, b)  $O_2$  molar fraction, and c)  $H_2O$  molar fraction

### 4.3.4 Heat balance

In the context of the electrolysis configuration, the occurring reaction is characterized as endothermic, meaning it necessitates the input of heat ( $\Delta H > 0$ ) to proceed. However, the heat associated with the irreversibility, is generated during the operation. These two opposite contributions lead to three possible scenarios:

- Endothermic EC ( $Phi_{tot} > 0$ )
- Adiabatic EC ( $Phi_{tot} = 0$ )
- Exothermic EC ( $Phi_{tot} < 0$ )

Where  $Phi_{tot}$  represents the total heat exchanged by the cell. The cell voltage at which the heat consumption of the electrochemical reaction is balanced by the heat generated by the irreversibilities is called thermoneutral voltage. At  $600^{\circ}\text{C}$  the thermoneutral voltage is  $1.282\text{ V}$  [53]. Figure. 4.6 illustrates the trend of temperature within the cell, representing the curves of average, maximum, and minimum temperature as a function of current density. At a voltage of  $1.282\text{V}$ ,

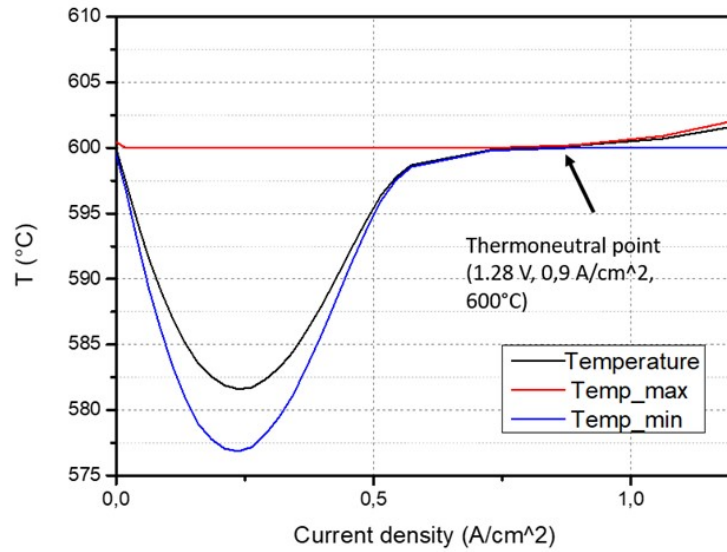


**Figure 4.6:** Temperature trend inside the cell. Black curve represent the average temperature inside the cell, while the red and blue are the minimum and maximum temperature in the cell respectively.

the condition of thermoneutrality, as previously described, is reached, where the temperature inside the cell becomes uniform. Figure. 4.7 shows the temperature distribution in the case below and over the thermoneutral respectively. In both

cases is possible to notice the difference of the temperature in the inlet and outlet zones, for both the electrode.

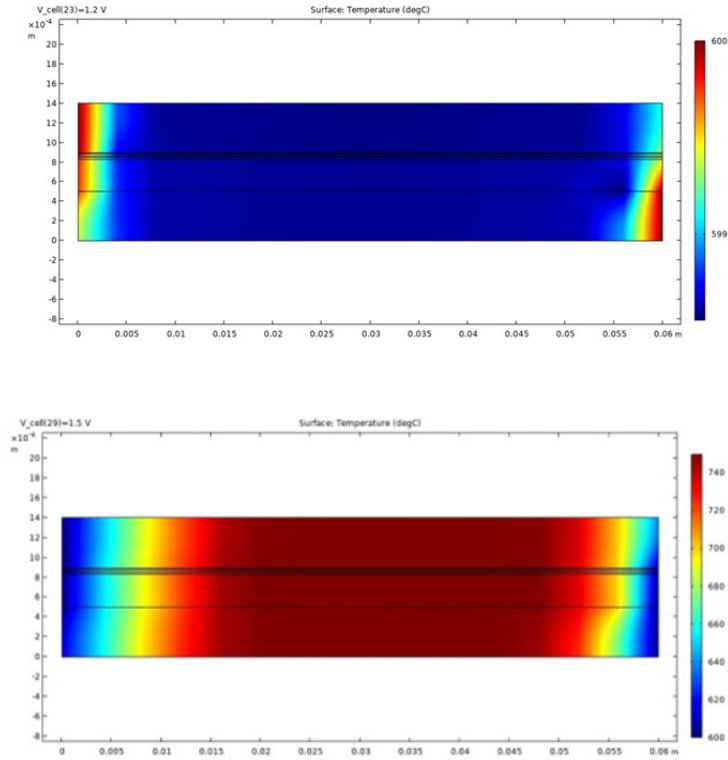


**Figure 4.7:** Temperature distribution results, for different cell voltage, from COMSOL software. a) distribution at 1.2 V, so under the thermoneutral voltage, b) distribution at 1.5 V, so over the thermoneutral voltage

# Chapter 5

## Conclusion

In conclusion, this work was focused on the study of PCEC technology, with the specific aim to increase the knowledge of about material compatibility and performance of a single repeating unit of a stack. Specifically, this thesis set out to analyse technological solutions related to the glass-ceramic sealant component of the cell which is an important element in the assembly of an SRU. The sealant ensures electrical insulation between parts and prevents gas leaks both internally and externally to the cell. This research included the evaluation of different Si-based glass systems, labelled V10, V11 (Na-containing) and, (Ba-containing) GC2. Moreover, a commercial Ba-based glass, labelled GM31107 was studied. The thermal and chemical behaviour of these glasses, both individually and in contact with other SRU components, such as electrolytes and metallic interconnects, was studied. Additionally, considering the need to develop a repeatable and scalable industrial deposition process for the glass via robocasting, viscous pastes were formulated, and their rheological properties characterized. Finally, using COMSOL Multiphysics software, a 2D model of the cell was developed to characterize the electrochemical and thermal behaviour of the cell, with the goal of subsequent development of a 3D model. The study into pastes for robocasting involved two distinct formulations: one utilizing terpineol as a solvent and the other employing PG. Both formulations exhibited highly promising characteristics in terms of extrusion behaviour, with viscosity ranging from  $10^1$  to  $10^2$  for a shear stress in the range of 1 to 100 1/s. This shear-thinning behaviour mirrors previous findings with pastes of GC2 and V11 glasses. Additionally, in terms of recovery after deposition, the PG paste demonstrated favourable outcomes, boasting an initial recovery rate of 73%. When considered together with earlier outcomes, these results emphasize the good performance of the GM31107-PG paste and its suitability for the deposition process in robocasting. Assessments of the thermal behaviour of the different glasses provided important results. The Si-based glasses, exhibited high characteristic temperatures, with glass transition temperatures ( $T_g$ ) between 600°C and 700°C.

In contrast, the commercial glass showed more favourable values, around 500-550°C. Considering the typical operating temperatures of PCEC devices (550-700 °C) these last T<sub>g</sub> range below the operating temperature makes the commercial glass a good candidate for this application. SEM analyses of interactions between different cell materials were made on joined (BCZY/glass-ceramic/AISI 441), after the selected joining thermal treatment and later after ageing. The second part, conducted only for GM31107, showed excellent results regarding adhesion with the metallic interconnector and the electrolyte, with no interdiffusion or formation of secondary phases. As for the glass, it initially did not develop any crystalline phase after the joining heat treatment, but later did so after ageing in a humidified atmosphere. Further studies will be necessary to evaluate this behaviour in more detail and, especially, the mechanisms that may generate it. Moreover, YSZ was added into the commercial glass to tune its properties. The outcomes revealed that for 8YSZ, after a simple joining thermal treatment, the glass exhibited extensive cracking, suggesting a difference on the CTE between the GM31107 and the adding compound. In contrast, with the 3YSZ, after the joining thermal treatment and an ageing in humidified atmosphere, good results were achieved, in terms of integrity of the glass, distribution of the YSZ, and adhesion in the interfaces. This underscores the potential use of YSZ for setting the properties of the glass. In conclusion, the 2D model allowed the evaluation of the cell's behaviour under operational conditions, both in terms of voltages and the thermal aspect. Polarization and power density curves were obtained, both of which followed the expected trend for electrolyser operation. The Open Circuit Voltage (OCV) in this case was around 0.98 V. After studying the electrochemical behaviour, a thermal analysis was conducted to identify the temperature distribution within the cell for different applied voltages. The thermal neutral point was reached at a voltage of 1.28 V, where the behaviour transitions from endothermic to exothermic, with the dominant contribution being the thermal power generated through the irreversibilities for voltages beyond the neutral point. The results obtained here are of significant interest for future model developments, serving as a foundational basis for creating 3D models of the cell, with the additional inclusion of studies on mechanical stress.

# Bibliography

- [1] «Net Zero by 2050 - A Roadmap for the Global Energy Sector». en. In: () (cit. on p. 1).
- [2] Dr Fatih Birol. «World Energy Outlook 2022». en. In: () (cit. on p. 1).
- [3] «The Future of Hydrogen». en. In: () (cit. on p. 2).
- [4] «Global Hydrogen Review 2022». en. In: (2022) (cit. on pp. 2, 3, 5).
- [5] Iain Staffell, Daniel Scamman, Anthony Velazquez Abad, Paul Balcombe, Paul E. Dodds, Paul Ekins, Nilay Shah, and Kate R. Ward. «The role of hydrogen and fuel cells in the global energy system». en. In: *Energy & Environmental Science* 12.2 (2019), pp. 463–491. ISSN: 1754-5692, 1754-5706. DOI: 10.1039/C8EE01157E. URL: <http://xlink.rsc.org/?DOI=C8EE01157E> (visited on 09/08/2023) (cit. on p. 2).
- [6] M.A. Laguna-Bercero. «Recent advances in high temperature electrolysis using solid oxide fuel cells: A review». en. In: *Journal of Power Sources* 203 (Apr. 2012), pp. 4–16. ISSN: 03787753. DOI: 10.1016/j.jpowsour.2011.12.019. URL: <https://linkinghub.elsevier.com/retrieve/pii/S0378775311024384> (visited on 08/08/2023) (cit. on pp. 3, 12, 20).
- [7] Stefania Marini, Paolo Salvi, Paolo Nelli, Rachele Pesenti, Marco Villa, Mario Berrettoni, Giovanni Zangari, and Yohannes Kiros. «Advanced alkaline water electrolysis». en. In: *Electrochimica Acta* 82 (Nov. 2012), pp. 384–391. ISSN: 00134686. DOI: 10.1016/j.electacta.2012.05.011. URL: <https://linkinghub.elsevier.com/retrieve/pii/S001346861200713X> (visited on 08/07/2023) (cit. on pp. 3, 4).
- [8] Merit Bodner, Astrid Hofer, and Viktor Hacker. «H<sub>2</sub> generation from alkaline electrolyzer: H<sub>2</sub> generation from alkaline electrolyzer». en. In: *Wiley Interdisciplinary Reviews: Energy and Environment* 4.4 (July 2015), pp. 365–381. ISSN: 20418396. DOI: 10.1002/wene.150. URL: <https://onlinelibrary.wiley.com/doi/10.1002/wene.150> (visited on 08/08/2023) (cit. on p. 4).
- [9] Simone Anelli. «Advanced strategies for Solid Oxide Electrolysis Cells». en. In: () (cit. on pp. 4, 6, 9, 10, 12, 23, 37, 38, 45, 53).

- [10] Frano Barbir. «PEM electrolysis for production of hydrogen from renewable energy sources». en. In: *Solar Energy* 78.5 (May 2005), pp. 661–669. ISSN: 0038092X. DOI: 10.1016/j.solener.2004.09.003. URL: <https://linkinghub.elsevier.com/retrieve/pii/S0038092X04002464> (visited on 09/09/2023) (cit. on p. 4).
- [11] Jiawen Ren, Jason Lau, Matthew Lefler, and Stuart Licht. «The Minimum Electrolytic Energy Needed To Convert Carbon Dioxide to Carbon by Electrolysis in Carbonate Melts». en. In: *The Journal of Physical Chemistry C* 119.41 (Oct. 2015), pp. 23342–23349. ISSN: 1932-7447, 1932-7455. DOI: 10.1021/acs.jpcc.5b07026. URL: <https://pubs.acs.org/doi/10.1021/acs.jpcc.5b07026> (visited on 09/09/2023) (cit. on p. 4).
- [12] H. Morita, M. Kawase, Y. Mugikura, and K. Asano. «Degradation mechanism of molten carbonate fuel cell based on long-term performance: Long-term operation by using bench-scale cell and post-test analysis of the cell». en. In: *Journal of Power Sources* 195.20 (Oct. 2010), pp. 6988–6996. ISSN: 03787753. DOI: 10.1016/j.jpowsour.2010.04.084. URL: <https://linkinghub.elsevier.com/retrieve/pii/S0378775310007755> (visited on 09/09/2023) (cit. on p. 4).
- [13] A. Hauch, R. Küngas, P. Blennow, A. B. Hansen, J. B. Hansen, B. V. Mathiesen, and M. B. Mogensen. «Recent advances in solid oxide cell technology for electrolysis». en. In: *Science* 370.6513 (Oct. 2020), eaba6118. ISSN: 0036-8075, 1095-9203. DOI: 10.1126/science.aba6118. URL: <https://www.science.org/doi/10.1126/science.aba6118> (visited on 08/06/2023) (cit. on p. 4).
- [14] Dmitry Medvedev. «Trends in research and development of protonic ceramic electrolysis cells». en. In: *International Journal of Hydrogen Energy* 44.49 (Oct. 2019), pp. 26711–26740. ISSN: 03603199. DOI: 10.1016/j.ijhydene.2019.08.130. URL: <https://linkinghub.elsevier.com/retrieve/pii/S0360319919331441> (visited on 08/08/2023) (cit. on p. 4).
- [15] Chuancheng Duan, Jake Huang, Neal Sullivan, and Ryan O’Hayre. «Proton-conducting oxides for energy conversion and storage». en. In: *Applied Physics Reviews* 7.1 (Mar. 2020), p. 011314. ISSN: 1931-9401. DOI: 10.1063/1.5135319. URL: <https://pubs.aip.org/apr/article/7/1/011314/124364/Proton-conducting-oxides-for-energy-conversion-and> (visited on 08/06/2023) (cit. on pp. 8, 11).
- [16] Paul A. Connor et al. «Tailoring SOFC Electrode Microstructures for Improved Performance». en. In: *Advanced Energy Materials* 8.23 (Aug. 2018), p. 1800120. ISSN: 16146832. DOI: 10.1002/aenm.201800120. URL: <https://onlinelibrary.wiley.com/doi/10.1002/aenm.201800120> (visited on 08/25/2023) (cit. on p. 10).

- [17] Neelima Mahato, Amitava Banerjee, Alka Gupta, Shobit Omar, and Kantesh Balani. «Progress in material selection for solid oxide fuel cell technology: A review». en. In: *Progress in Materials Science* 72 (July 2015), pp. 141–337. ISSN: 00796425. DOI: 10.1016/j.pmatsci.2015.01.001. URL: <https://linkinghub.elsevier.com/retrieve/pii/S0079642515000195> (visited on 08/25/2023) (cit. on pp. 10, 12).
- [18] Nur Nadhihah Mohd Tahir, Nurul Akidah Baharuddin, Abdullah Abdul Samat, Nafisah Osman, and Mahendra Rao Somalu. «A review on cathode materials for conventional and proton-conducting solid oxide fuel cells». en. In: *Journal of Alloys and Compounds* 894 (Feb. 2022), p. 162458. ISSN: 09258388. DOI: 10.1016/j.jallcom.2021.162458. URL: <https://linkinghub.elsevier.com/retrieve/pii/S0925838821038688> (visited on 09/10/2023) (cit. on pp. 11, 12).
- [19] Junyoung Kim, Sivaprakash Sengodan, Goeun Kwon, Dong Ding, Jeeyoung Shin, Meilin Liu, and Guntae Kim. «Triple-Conducting Layered Perovskites as Cathode Materials for Proton-Conducting Solid Oxide Fuel Cells». en. In: *ChemSusChem* 7.10 (Oct. 2014), pp. 2811–2815. ISSN: 18645631. DOI: 10.1002/cssc.201402351. URL: <https://onlinelibrary.wiley.com/doi/10.1002/cssc.201402351> (visited on 08/30/2023) (cit. on p. 11).
- [20] Miguel Angel Laguna-Bercero, ed. *High Temperature Electrolysis*. en. Vol. 95. Lecture Notes in Energy. Cham: Springer International Publishing, 2023. ISBN: 978-3-031-22507-9 978-3-031-22508-6. DOI: 10.1007/978-3-031-22508-6. URL: <https://link.springer.com/10.1007/978-3-031-22508-6> (visited on 08/13/2023) (cit. on pp. 12, 14).
- [21] B. Singh, S. Ghosh, S. Aich, and B. Roy. «Low temperature solid oxide electrolytes (LT-SOE): A review». en. In: *Journal of Power Sources* 339 (Jan. 2017), pp. 103–135. ISSN: 03787753. DOI: 10.1016/j.jpowsour.2016.11.019. URL: <https://linkinghub.elsevier.com/retrieve/pii/S0378775316315439> (visited on 08/06/2023) (cit. on p. 12).
- [22] Anna V. Kasyanova, Inna A. Zvonareva, Natalia A. Tarasova, Lei Bi, Dmitry A. Medvedev, and Zongping Shao. «Electrolyte materials for protonic ceramic electrochemical cells: Main limitations and potential solutions». en. In: *Materials Reports: Energy* 2.4 (Nov. 2022), p. 100158. ISSN: 26669358. DOI: 10.1016/j.matre.2022.100158. URL: <https://linkinghub.elsevier.com/retrieve/pii/S2666935822001057> (visited on 08/06/2023) (cit. on p. 13).
- [23] Sanjeevani V. Bhide and Anil V. Virkar. «Stability of BaCeO<sub>3</sub>-Based Proton Conductors in Water-Containing Atmospheres». en. In: *Journal of The Electrochemical Society* 146.6 (June 1999), pp. 2038–2044. ISSN: 0013-4651,

- 1945-7111. DOI: 10.1149/1.1391888. URL: <https://iopscience.iop.org/article/10.1149/1.1391888> (visited on 08/13/2023) (cit. on p. 14).
- [24] Cameron W Tanner and Anil V Virkar. «Instability of  $\text{BaCeO}_3$  in  $\text{H}_2\text{O}$ -Containing Atmospheres». en. In: *J. Electrochem. Soc.* 143.4 (1996) (cit. on p. 14).
- [25] S. Ricote, N. Bonanos, A. Manerbino, and W.G. Coors. «Conductivity study of dense  $\text{BaCe}_x\text{Zr}(0.9x)\text{Y}_0.1\text{O}(3)$  prepared by solid state reactive sintering at  $1500^\circ\text{C}$ ». en. In: *International Journal of Hydrogen Energy* 37.9 (May 2012), pp. 7954–7961. ISSN: 03603199. DOI: 10.1016/j.ijhydene.2011.08.118. URL: <https://linkinghub.elsevier.com/retrieve/pii/S036031991102043X> (visited on 08/13/2023) (cit. on p. 14).
- [26] Sihyuk Choi, Chris J. Kucharczyk, Yangang Liang, Xiaohang Zhang, Ichiro Takeuchi, Ho-Il Ji, and Sossina M. Haile. «Exceptional power density and stability at intermediate temperatures in protonic ceramic fuel cells». en. In: *Nature Energy* 3.3 (Feb. 2018), pp. 202–210. ISSN: 2058-7546. DOI: 10.1038/s41560-017-0085-9. URL: <https://www.nature.com/articles/s41560-017-0085-9> (visited on 08/06/2023) (cit. on p. 14).
- [27] Chuancheng Duan, Robert Kee, Huayang Zhu, Neal Sullivan, Liangzhu Zhu, Liuzhen Bian, Dylan Jennings, and Ryan O’Hayre. «Highly efficient reversible protonic ceramic electrochemical cells for power generation and fuel production». en. In: *Nature Energy* 4.3 (Mar. 2019), pp. 230–240. ISSN: 2058-7546. DOI: 10.1038/s41560-019-0333-2. URL: <https://www.nature.com/articles/s41560-019-0333-2> (visited on 08/06/2023) (cit. on p. 14).
- [28] Lei Yang, Shizhong Wang, Kevin Blinn, Mingfei Liu, Ze Liu, Zhe Cheng, and Meilin Liu. «Enhanced Sulfur and Coking Tolerance of a Mixed Ion Conductor for SOFCs:  $\text{BaZr}_{0.1}\text{Ce}_{0.7}\text{Y}_{0.2-x}\text{Yb}_x\text{O}_{3-x}$ ». en. In: *Science* 326.5949 (Oct. 2009), pp. 126–129. ISSN: 0036-8075, 1095-9203. DOI: 10.1126/science.1174811. URL: <https://www.science.org/doi/10.1126/science.1174811> (visited on 08/13/2023) (cit. on p. 14).
- [29] Muhammad Bilal Hanif, Sajid Rauf, Martin Motola, Zaheer Ud Din Babar, Chang-Jiu Li, and Cheng-Xin Li. «Recent progress of perovskite-based electrolyte materials for solid oxide fuel cells and performance optimizing strategies for energy storage applications». en. In: *Materials Research Bulletin* 146 (Feb. 2022), p. 111612. ISSN: 00255408. DOI: 10.1016/j.materresbull.2021.111612. URL: <https://linkinghub.elsevier.com/retrieve/pii/S0025540821004098> (visited on 08/30/2023) (cit. on p. 15).

- [30] W.Z. Zhu and S.C. Deevi. «Development of interconnect materials for solid oxide fuel cells». en. In: *Materials Science and Engineering: A* 348.1-2 (May 2003), pp. 227–243. ISSN: 09215093. DOI: 10.1016/S0921-5093(02)00736-0. URL: <https://linkinghub.elsevier.com/retrieve/pii/S0921509302007360> (visited on 08/14/2023) (cit. on p. 15).
- [31] Z Gary Yang, Dean M. Paxton, K. Scott Weil, Jeffrey W. Stevenson, and Prabhakar Singh. *Materials Properties Database for Selection of High-Temperature Alloys and Concepts of Alloy Design for SOFC Applications*. en. Tech. rep. PNNL-14116, 15010553. Nov. 2002, PNNL-14116, 15010553. DOI: 10.2172/15010553. URL: <http://www.osti.gov/servlets/purl/15010553-49RdBr/native/> (visited on 08/26/2023) (cit. on p. 16).
- [32] Ruofan Wang, Zhihao Sun, Jung-Pyung Choi, Soumendra N. Basu, Jeffrey W. Stevenson, and Michael C. Tucker. «Ferritic stainless steel interconnects for protonic ceramic electrochemical cell stacks: Oxidation behavior and protective coatings». en. In: *International Journal of Hydrogen Energy* 44.47 (Oct. 2019), pp. 25297–25309. ISSN: 03603199. DOI: 10.1016/j.ijhydene.2019.08.041. URL: <https://linkinghub.elsevier.com/retrieve/pii/S0360319919329581> (visited on 08/26/2023) (cit. on p. 16).
- [33] M.K. Mahapatra and K. Lu. «Glass-based seals for solid oxide fuel and electrolyzer cells – A review». en. In: *Materials Science and Engineering: R: Reports* 67.5-6 (Feb. 2010), pp. 65–85. ISSN: 0927796X. DOI: 10.1016/j.mser.2009.12.002. URL: <https://linkinghub.elsevier.com/retrieve/pii/S0927796X09001119> (visited on 08/06/2023) (cit. on pp. 16–19).
- [34] M.K. Mahapatra and K. Lu. «Seal glass for solid oxide fuel cells». en. In: *Journal of Power Sources* 195.21 (Nov. 2010), pp. 7129–7139. ISSN: 03787753. DOI: 10.1016/j.jpowsour.2010.06.003. URL: <https://linkinghub.elsevier.com/retrieve/pii/S0378775310009419> (visited on 08/06/2023) (cit. on pp. 19, 20).
- [35] C. Lara, M.J. Pascual, and A. Durán. «Glass-forming ability, sinterability and thermal properties in the systems RO–BaO–SiO<sub>2</sub> (R=Mg, Zn)». en. In: *Journal of Non-Crystalline Solids* 348 (Nov. 2004), pp. 149–155. ISSN: 00223093. DOI: 10.1016/j.jnoncrysol.2004.08.140. URL: <https://linkinghub.elsevier.com/retrieve/pii/S0022309304007100> (visited on 08/28/2023) (cit. on p. 19).
- [36] S.T. Reis and R.K. Brow. «Designing Sealing Glasses for Solid Oxide Fuel Cells». en. In: *Journal of Materials Engineering and Performance* 15.4 (Aug. 2006), pp. 410–413. ISSN: 10599495, 00000000. DOI: 10.1361/105994906X117206. URL: <http://link.springer.com/10.1361/105994906X117206> (visited on 08/28/2023) (cit. on p. 19).

- [37] Laura del-Mazo-Barbara and Maria-Pau Ginebra. «Rheological characterisation of ceramic inks for 3D direct ink writing: A review». en. In: *Journal of the European Ceramic Society* 41.16 (Dec. 2021), pp. 18–33. ISSN: 09552219. DOI: 10.1016/j.jeurceramsoc.2021.08.031. URL: <https://linkinghub.elsevier.com/retrieve/pii/S0955221921005987> (visited on 08/23/2023) (cit. on pp. 20–23, 30).
- [38] Albert Tarancón and Vincenzo Esposito. «3D Printing for Energy Applications». en. In: () (cit. on p. 20).
- [39] Chao-Fan Guo, Min Zhang, and Bhesh Bhandari. «A comparative study between syringe-based and screw-based 3D food printers by computational simulation». en. In: *Computers and Electronics in Agriculture* 162 (July 2019), pp. 397–404. ISSN: 01681699. DOI: 10.1016/j.compag.2019.04.032. URL: <https://linkinghub.elsevier.com/retrieve/pii/S0168169918312031> (visited on 08/24/2023) (cit. on p. 23).
- [40] Soukaina Lamnini, Hamada Elsayed, Yazid Lakhdar, Francesco Baino, Federico Smeacetto, and Enrico Bernardo. «Robocasting of advanced ceramics: ink optimization and protocol to predict the printing parameters - A review». en. In: *Heliyon* 8.9 (Sept. 2022), e10651. ISSN: 24058440. DOI: 10.1016/j.heliyon.2022.e10651. URL: <https://linkinghub.elsevier.com/retrieve/pii/S2405844022019399> (visited on 08/23/2023) (cit. on pp. 23, 24).
- [41] Xiaochun Wang, Zhun Kou, Hao Wu, Yi Song, Xuepeng Zhao, Shanping Xu, and Li Li. «Improvement of thermal cycle stability of YSZ-glass composite seals for intermediate temperature solid oxide fuel cell». en. In: *Ceramics International* (Sept. 2023), S0272884223026226. ISSN: 02728842. DOI: 10.1016/j.ceramint.2023.08.359. URL: <https://linkinghub.elsevier.com/retrieve/pii/S0272884223026226> (visited on 09/18/2023) (cit. on p. 29).
- [42] Qiuju Zheng, Yanfei Zhang, Maziar Montazerian, Ozgur Gulbiten, John C. Mauro, Edgar D. Zanotto, and Yuanzheng Yue. «Understanding Glass through Differential Scanning Calorimetry». en. In: *Chemical Reviews* 119.13 (July 2019), pp. 7848–7939. ISSN: 0009-2665, 1520-6890. DOI: 10.1021/acs.chemrev.8b00510. URL: <https://pubs.acs.org/doi/10.1021/acs.chemrev.8b00510> (visited on 08/14/2023) (cit. on pp. 33, 34).
- [43] Satohiro Tanaka. «Theory of power-compensated DSC». en. In: *Thermochimica Acta* 210 (Nov. 1992), pp. 67–76. ISSN: 00406031. DOI: 10.1016/0040-6031(92)80277-4. URL: <https://linkinghub.elsevier.com/retrieve/pii/0040603192802774> (visited on 09/11/2023) (cit. on p. 33).

- [44] A R Boccaccini and B Hamann. «Review In Situ high-temperature optical microscopy». en. In: () (cit. on p. 35).
- [45] Joseph I. Goldstein, Dale E. Newbury, Joseph R. Michael, Nicholas W.M. Ritchie, John Henry J. Scott, and David C. Joy. *Scanning Electron Microscopy and X-Ray Microanalysis*. en. New York, NY: Springer New York, 2018. ISBN: 978-1-4939-6674-5 978-1-4939-6676-9. DOI: 10.1007/978-1-4939-6676-9. URL: <https://link.springer.com/10.1007/978-1-4939-6676-9> (visited on 08/21/2023) (cit. on p. 37).
- [46] A.G. Sabato, A. Rost, J. Schilm, M. Kusnezoff, M. Salvo, A. Chrysanthou, and F. Smeacetto. «Effect of electric load and dual atmosphere on the properties of an alkali containing diopside-based glass sealant for solid oxide cells». en. In: *Journal of Power Sources* 415 (Mar. 2019), pp. 15–24. ISSN: 03787753. DOI: 10.1016/j.jpowsour.2019.01.051. URL: <https://linkinghub.elsevier.com/retrieve/pii/S0378775319300692> (visited on 08/06/2023) (cit. on p. 39).
- [47] Ilaria Ritucci, Karsten Agersted, Philipp Zielke, Anders Christian Wulff, Peyman Khajavi, Federico Smeacetto, Antonio Gianfranco Sabato, and Ragnar Kiebach. «A Ba-free sealing glass with a high coefficient of thermal expansion and excellent interface stability optimized for SOFC/SOEC stack applications». en. In: *International Journal of Applied Ceramic Technology* 15.4 (July 2018), pp. 1011–1022. ISSN: 1546542X. DOI: 10.1111/ijac.12853. URL: <https://onlinelibrary.wiley.com/doi/10.1111/ijac.12853> (visited on 09/18/2023) (cit. on p. 39).
- [48] Smeacetto Federico, Santarelli Massimo, Dr Anelli Simone, and Dealberti Gabriele. «Development of glass-ceramic sealants and modelling of single repeating unit for reversible Protonic Ceramic Cells (PCCs)». en. In: () (cit. on pp. 46, 47, 53, 59, 60, 62, 63).
- [49] Sasanka N. Ranasinghe and Peter H. Middleton. «Modelling of single cell solid oxide fuel cells using COMSOL multiphysics». en. In: *2017 IEEE International Conference on Environment and Electrical Engineering and 2017 IEEE Industrial and Commercial Power Systems Europe (EEEIC / I&CPS Europe)*. Milan, Italy: IEEE, June 2017, pp. 1–6. ISBN: 978-1-5386-3917-7. DOI: 10.1109/EEEIC.2017.7977790. URL: <http://ieeexplore.ieee.org/document/7977790/> (visited on 10/01/2023) (cit. on p. 60).
- [50] Ji-Hao Zhang, Li-Bin Lei, Di Liu, Fu-Yun Zhao, Meng Ni, and Fanglin Chen. «Mathematical modeling of a proton-conducting solid oxide fuel cell with current leakage». en. In: *Journal of Power Sources* 400 (Oct. 2018), pp. 333–340. ISSN: 03787753. DOI: 10.1016/j.jpowsour.2018.08.038. URL:

- <https://linkinghub.elsevier.com/retrieve/pii/S0378775318308978> (visited on 10/01/2023) (cit. on p. 60).
- [51] A.N. Celik. «Three-dimensional multiphysics model of a planar solid oxide fuel cell using computational fluid dynamics approach». en. In: *International Journal of Hydrogen Energy* 43.42 (Oct. 2018), pp. 19730–19748. ISSN: 03603199. DOI: 10.1016/j.ijhydene.2018.08.212. URL: <https://linkinghub.elsevier.com/retrieve/pii/S0360319918328155> (visited on 10/01/2023) (cit. on p. 60).
- [52] Robert Zinni. «Thermal Stress Analysis of a Solid Oxide Fuel Cell Interconnect using a Staggered Tube Bank Geometry». en. In: () (cit. on p. 61).
- [53] D. Catalán-Martínez, L. Navarrete, M. Tarach, J. Santos-Blasco, E. Vøllestad, T. Norby, M.I. Budd, P. Veenstra, and J.M. Serra. «Thermo-fluid dynamics modelling of steam electrolysis in fully-assembled tubular high-temperature proton-conducting cells». en. In: *International Journal of Hydrogen Energy* 47.65 (July 2022), pp. 27787–27799. ISSN: 03603199. DOI: 10.1016/j.ijhydene.2022.06.112. URL: <https://linkinghub.elsevier.com/retrieve/pii/S0360319922027446> (visited on 10/01/2023) (cit. on p. 67).